UNIVERSITÀ DEGLI STUDI DI MILANO - BICOCCA
DIPARTIMENTO DI FISICA G. OCCHIALINI

CORSO DI DOTTORATO IN FISICA E ASTRONOMIA
CICLO XXVII

MEASUREMENT OF THE BRANCHING FRACTION OF $B_c^+ \to J/\psi \pi^+ \pi^+ \pi^-$ RELATIVE TO $B_c^+ \to J/\psi \pi^+$ AND OF THE PRODUCTION CROSS-SECTION OF $B_c^+ \to J/\psi \pi^+$ RELATIVE TO $B^+ \to J/\psi K^+$ WITH THE CMS EXPERIMENT

Settore scientifico disciplinare FIS/01

Tesi di Dottorato di:
SARA FIORENDI

Tutore: Prof. L. Moroni

Anno Accademico 2013-2014

Abstract

The pseudoscalar B_c meson, the ground state of the $\bar{b}c$ system, is the lightest particle containing two heavy quarks of different flavors, and thus represents a unique laboratory to study heavy-quark dynamics. The investigation of B_c meson properties is of special interest compared to the flavor symmetric heavy quarkonium ($\bar{b}b$, $\bar{c}c$) states, and provides a new testing ground for predictions in the context of effective models inspired by quantum chromodynamics.

Each of the two constituents quarks can decay via the weak interaction. In particular, the $b \to c$ transition, which accounts for about 20% of the decay rate, offers an easily accessible experimental signature, having a high probability of producing a J/ψ meson. Consequently, the first B_c observation was made in the semileptonic channel $B_c^+ \to J/\psi \ell^+ \nu \, (\ell = e, \mu)$ by the CDF Collaboration.

The physics of the B_c meson has entered a new era with the advent of the CERN Large Hadron Collider (LHC). Thanks to the unprecedented energy and instantaneous luminosity provided by the LHC, the available B_c statistics is much higher than in previous experiments. The features of the Compact Muon Solenoid (CMS) experiment allow to pursue a wide range of measurements concerning the physics of the *beauty*-quark. In addition to indirect searches for New Physics through studies of rare decays, such as $B_s \to \mu^+\mu^-$ and $B^0 \to K^{0*}\mu^+\mu^-$, the investigation of the B_c meson properties represents an important topic in the physics program of the experiment. Moreover, accurate measurements of its production cross section and decay modes are crucial to achieve a precise background estimation in the searches for rare decays.

In this thesis I present the analyses of the multi-body $B_c^+ \to J/\psi \pi^+ \pi^+ \pi^-$ and the two-body $B_c^+ \to J/\psi \pi^+$ channels, along with a measurement of the ratio of their branching fractions $R_{B_c} \equiv B(B_c^+ \to J/\psi \pi^+ \pi^+ \pi^-)/B(B_c^+ \to J/\psi \pi^+)$, with the CMS detector at the LHC. The CMS experiment, due to the excellent muon identification system and tracking detectors, is indeed particularly suited to the study of final states containing J/ψ mesons, where $J/\psi \to \mu^+\mu^-$. The ratio R_{B_c} is measured to be $2.55 \pm 0.80(\text{stat.}) \pm 0.33(\text{syst.})^{+0.04}_{-0.01}(\tau_{B_c})$. This measurement is independent of the poorly known B_c production cross section.

The $B_c^+ \to J/\psi \pi^+$ mode is also compared to the $B^+ \to J/\psi K^+$ decay, which has a similar vertex topology. The ratio of their production cross section times branching fractions $R_{c/u} \equiv (\sigma(B_c^+) \times B(B_c^+ \to J/\psi \pi^+))/(\sigma(B^+) \times B(B^+ \to J/\psi K^+))$ is measured to be $[0.48 \pm 0.05(\text{stat.}) \pm 0.03(\text{syst.}) \pm 0.05(\tau_{B_c})]\%$. In the kinematic region investigated, the B_c^+ transverse momentum is greater than 15 GeV and the rapidity region is $|y| < 1.6$, complementary to that accessible in the LHCb experiment. This measurement contributes to a more complete

understanding of B_c production in pp collisions.

The analysis was performed on a 5.1 fb^{-1} sample of pp data, collected by the CMS experiment at $\sqrt{s} = 7$ TeV, using a trigger based on the selection of two muons from a J/ψ decay. The reduction of the copious combinatorial background is achieved by exploiting both kinematic and topological selections on the B_c candidate. The reconstruction efficiency has been accurately parametrized and measured on dedicated Monte Carlo samples, which well simulate the data-taking conditions. Various sources of systematic uncertainties have been evaluated and are described in details in the text.

This thesis is organized as follows.
A short review of the Standard Model is outlined in Chapter 1.

Motivations for B_c meson studies are described in Chapter 2, where B_c properties are examined, along with the status of theoretical predictions and the current experimental scenario.

Chapter 3 is devoted to the illustration of the experimental apparatus used to perform the measurement. The LHC accelerator and the CMS detector are described, focusing the attention on the CMS inner tracker and muon stations, which are used to reconstruct the final state particles of the B_c decays.

The detailed description of the measurements of R_{B_c} and $R_{c/u}$ is discussed in Chapter 4. The first part of the Chapter is dedicated to an overview of the procedure used to extract the $B_c^+ \to J/\psi \pi^+ \pi^+ \pi^-$, $B_c^+ \to J/\psi \pi^+$ and $B^+ \to J/\psi K^+$ signals. The measurements of R_{B_c} and $R_{c/u}$ are then described in the second part of the Chapter, along with the efficiency parametrization and the evaluation of systematic uncertainties. Finally, results are compared with the available theoretical predictions and with measurements from other experiments.

Sommario

Il mesone pseudoscalare B_c, stato fondamentale del sistema $(\bar{b}c)$, è la particella più leggera formata da due quark pesanti di diverso sapore, e rappresenta perciò un laboratorio ideale per lo studio della dinamica dei decadimenti degli Heavy Flavor.

Lo studio delle proprietà del mesone B_c è di particolare interesse se paragonato agli stati $\bar{b}b$ e $\bar{c}c$, che non portano sapore, e offre un nuovo terreno per verificare le predizioni dei modelli effettivi ispirati dalla cromodinamica quantistica.

Ciascuno dei due quark costituenti la B_c può decadere attraverso l'interazione debole. In particolare, la transizione $b \rightarrow c$, che copre circa il 20% del rate di decadimento, ha un'alta probabilità di produrre un mesone J/ψ nello stato finale, che costituisce una segnatura sperimentale facilmente identificabile. Infatti, la prima osservazione del mesone B_c è stata effettuata nel canale di decadimento semileptonico $B_c^+ \rightarrow J/\psi \ell^+ \nu \, (\ell = \text{e}, \mu)$ dalla Collaborazione CDF.

Lo studio sperimentale del mesone B_c è entrato in una nuova fase con l'avvento del Large Hadron Collider (LHC) al CERN. Grazie alle alte energie e luminosità istantanee mai raggiunte prima, la statistica di eventi di B_c disponibile è molto più alta che negli esperimenti precedenti. Le caratteristiche dell'esperimento CMS (Compact Muon Solenoid) consentono di perseguire un ampio programma di misure nell'ambito della fisica del quark $beauty$. Accanto a ricerche indirette di nuova fisica attraverso lo studio di decadimenti rari, come $B_s \rightarrow \mu^+\mu^-$ e $B^0 \rightarrow K^{0*}\mu^+\mu^-$, lo studio del mesone B_c rappresenta un settore importante nel programma di fisica dell'esperimento. Inoltre, poichè la B_c rappresenta un potenziale background proprio nei decadimenti rari, una misura della sua sezione d'urto e la caratterizzazione dei suoi stati finali sono cruciali per poter ottenere un'accurata stima dei fondi.

In questa tesi presento l'analisi dei canali di decadimento $B_c^+ \rightarrow J/\psi \pi^+ \pi^+ \pi^-$ e $B_c^+ \rightarrow J/\psi \pi^+$, e una misura del rapporto delle loro Branching Fraction, $R_{B_c} \equiv B(B_c^+ \rightarrow J/\psi \pi^+ \pi^+ \pi^-)/B(B_c^+ \rightarrow J/\psi \pi^+)$. La misura è stata ottenuta presso l'esperimento CMS a LHC. L'esperimento CMS, infatti, è particolarmente adatto allo studio degli stati finali contenenti mesoni J/ψ, dove $J/\psi \rightarrow \mu^+\mu^-$, grazie alle eccellenti prestazioni dei sistemi di rivelazione di muoni e di tracciamento. La misura del rapporto R_{B_c} è $2.55 \pm 0.80(\text{stat.}) \pm 0.33(\text{syst.})^{+0.04}_{-0.01}(\tau_{B_c})$. Questo rapporto è indipendente dalla sezione d'urto della B_c, la cui misura non è ancora disponibile.

Il canale $B_c^+ \rightarrow J/\psi \pi^+$ è anche confrontato con il decadimento $B^+ \rightarrow J/\psi K^+$, che ha le stesse caratteristiche topologiche. Il rapporto delle sezioni

d'urto moltiplicato per le rispettive Branching Fractions è misurato essere $[0.48\pm$ $0.05\,(\text{stat.})\pm 0.03\,(\text{syst.})\pm 0.05\,(\tau_{B_c})]\%$. Nello spazio cinematico esplorato, il momento traverso del mesone B_c^+ è maggiore di 15 GeV e la regione di rapidità è $|y| < 1.6$, complementare a quella accessibile all'esperimento LHCb. Questa misura contribuisce a una comprensione più completa della produzione di B_c^+ in collisioni protone-protone.

L'analisi è stata condotta sui dati raccolti da CMS a $\sqrt{s} = 7$ TeV, che corrispondono a una luminosità integrata di 5.1 fb^{-1}. Il trigger utilizzato per la selezione degli eventi si basa sull'identificazione dei due muoni provenienti dal decadimento del mesone J/ψ. L'abbondante fondo combinatorio è stato ridotto sfruttando selezioni topologiche e cinematiche. L'efficienza di ricostruzione è stata accuratamente parametrizzata e misurata su appositi campioni Monte Carlo, che ben riproducono le condizioni della presa dati. Sono state valutate diverse fonti di incertezza sistematica, descritte accuratamente nel testo.

Contents

Chapter 1

Introduction

The Standard Model of particle physics represents the current best understanding of elementary particles and their interactions. Its predictions have been tested successfully to a high level level of accuracy in a variety of experiments and over a wide range of energies. However, the SM does not explain the complete picture and many fundamental questions are still open. This Chapter provides a general overview of the SM concepts and of theoretical tools useful for this thesis.

1.1 The Standard Model

The Standard Model of particle physics (SM) [1, 2, 3] is a theory which describes the elementary particles and their interactions. More precisely, the SM addresses strong, electromagnetic and weak interactions. The gravitational force is not included in the theory, and is expected to have a negligible impact on fundamental particle processes at accessible energies.

The SM is a renormalizable field theory based on a local symmetry that generalise the structure of Quantum Electrodynamics (QED) to a larger set of conserved currents and charges (eight strong charges and four electro-weak charges). It is based on the gauge group $SU(3)_C \otimes SU(2)_L \otimes U(1)_Y$, where the SU(3) gauge group is the symmetry group of strong interactions, and $SU(2)_L \otimes U(1)_Y$ is the unified gauge group of weak and electromagnetic interactions.

QED describes the interaction between two electrically charged particles with the exchange of photons, emitted by one electron and reabsorbed by the second. In a similar way, the SM matter fields are half-integer spin particles (fermions): the quarks, which have color and electroweak charge, and leptons, which only have electroweak charge. All the fermions have a corresponding

anti-particle with the same mass and opposite electric charge.

Three fermion generations are distinguished, as shown in Tab. 1.1: Each

Generation	Quarks		Leptons	
I	u	d	e	ν_e
II	c	s	μ	ν_μ
III	t	b	τ	ν_τ

Table 1.1: The three generations of quarks and leptons.

family contains a weakly charged doublet of quarks, in three color replicas, and a colorless weakly charged doublet with a neutrino (ν) and a charged lepton.

Forces are mediated by spin 1 bosons: the photon (γ), the weak interaction gauge bosons W^+, W^- and Z^0 and the eight gluons g that mediate the strong interactions. The photon and the gluons are massless, as a consequence of the exact conservation of the corresponding symmetry generators, the electric charge and the eight color charges. The weak bosons W^+, W^- and Z^0 have large masses ($m_W \sim 80.4$ GeV, $m_Z = 91.2$ GeV), because the corresponding symmetries are broken.

In the SM the spontaneous breaking of the electroweak gauge symmetry is induced by the Higgs mechanism [4, 5, 6], which predicts the presence in the physical spectrum of one spin 0 particle, the Higgs boson. The Higgs fields interact with the fermionic sector through "Yukawa terms". Fermions acquire a mass proportional to the vacuum expectation value of the Higgs field and the strength of the coupling. Particles that do not interact with the Higgs field (photon and gluons) remain massless.

Fermion couplings to the Higgs field not only determine their masses; they induce a misalignment of quark mass eigenstates with respect to the eigenstates of the weak charges, thereby allowing all fermions of heavy families to decay to lighter ones. These couplings provide the only mechanism within the SM that can account for the observed violation of CP, that is, invariance of the laws of nature under mirror reflection (parity P) and the interchange of particles with their anti-particles (charge conjugation C).

The SM Lagrangian is commonly divided in two parts:

$$L_{SM} = L_{QED} + L_{QCD} \tag{1.1}$$

where L_{QED} holds the QED interactions and its gauge bosons, and L_{QCD} holds the gluon fields and their interactions.

1.1.1 The EW sector

The EW sector is based on the gauge group $SU(2)_L \otimes U(1)_Y$. The $SU(2)_L$ group is associated to three generators T_a, corresponding to three gauge bosons W_a^μ (with a = 1, 2, 3). The generator of the $U(1)_Y$ symmetry is Y, and the associated boson is B^μ.

The left-handed fermion fields of the i_{th} fermion family transform as doublets under SU(2), while right-handed fields are SU(2) singlets.
A complex scalar Higgs doublet,

$$\phi \equiv \left(\begin{array}{c} \phi^+ \\ \phi^0 \end{array} \right),$$

is added to the model in order to explain mass generation through the spontaneous symmetry breaking mechanism. The Higgs potential is

$$V(\phi) = \mu^2 \phi^\dagger \phi + \frac{\lambda^2}{2}(\phi^\dagger \phi)^2 \qquad (1.2)$$

For negative values of μ^2, the vacuum expectation value of ϕ is different from zero ($v = \mu/\sqrt{\lambda} \approx 246$ GeV), breaking part of the electroweak gauge symmetry.

After the symmetry breaking, linear combinations of the boson fields W_a^μ and B^μ form the physical electromagnetic and weak fields:

$$A_\mu = cos\theta_w B_\mu + sin\theta_w W_\mu^3, \qquad (1.3)$$

$$Z_\mu = -sin\theta_w B_\mu + cos\theta_w W_\mu^3, \qquad (1.4)$$

$$W_\mu^\pm = \frac{W_\mu^1 \mp W_\mu^2}{\sqrt{2}}, \qquad (1.5)$$

where θ_w is the Weinberg angle $\theta_w = \tan^{-1}(g'/g)$ and g' and g are the coupling constants of $SU(2)_L$ and $U(1)_Y$ respectively.
The weak boson masses are given by:

$$M_H = v\sqrt{2\lambda} \qquad M_W = \frac{v|g|}{2} \qquad M_Z = \frac{1}{2}v\sqrt{g^2 + g'^2} = \frac{M_W}{\cos\theta_w} \qquad M_\gamma = 0$$

$$(1.6)$$

The physical mass of the Higgs boson is therefore a parameter of the theory, and has to be determined experimentally. In 2012 both the ATLAS and CMS experiments at the LHC reported the observation of a new boson with a mass

near 125 GeV [7, 8]. In the following two years, the production and decay rates and the spin-parity quantum numbers of the new boson have been extensively studied. Results show that the properties of the particle observed are compatible with those expected for a SM Higgs boson (Fig.1.1).
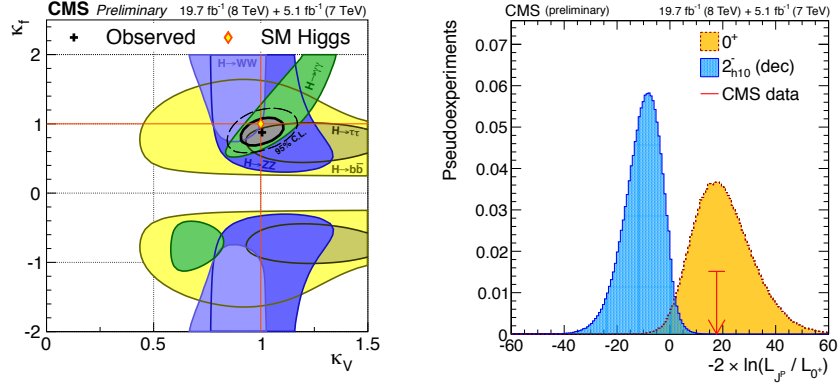
Figure 1.1: The 68% CL contours for individual channels (colored swaths) and for the overall combination (thick curve) for the (K_V, K_F) parameters, which describe the Higgs boson couplings to vector and fermion, respectively. The cross indicates the global best-fit values. The dashed contour bounds the 95% CL confidence region for the combination. The yellow diamond represents the SM expectation [9]. The right plot show the distributions of a test statistic for the hypotheses $J^P = 1^+$ or 0^+ [10]. The red arrow indicates the observed value.

The fermion EW couplings are divided in charged and neutral current interactions, depending on the mediator boson:

$$L_{CC} = \frac{g'}{2\sqrt{2}}(J_\mu^+ W^{+\mu} + J_\mu^- W^{-\mu}), \tag{1.7}$$

$$L_{NC} = eJ_\mu^{em}A^\mu + \frac{g'}{2\cos\theta_w}J_\mu^0 Z^\mu, \tag{1.8}$$

where the currents J^i are:

$$J_\mu^+ = (\bar{u}d')_{V-A} + (\bar{\nu}_e e)_{V-A}, \tag{1.9}$$

$$J_\mu^{em} = \sum_f Q_f \bar{f}\gamma_\mu f, \tag{1.10}$$

$$J_\mu^0 = \sum_f \gamma_\mu(v_f - a_f\gamma_5)f, \tag{1.11}$$

the sum run over each fermion f and $(\bar{u}d')_{V-A} = \bar{u}\gamma_\mu(1-\gamma_5)d'$. γ_i are the Dirac matrices, v_f and a_f are the vector and axial couplings, respectively.

1.1.2 The CKM matrix

In the SM, the masses and mixings of quarks originate from the Yukawa interactions with the Higgs condensate.

The quark mixing, by convention, is restricted to the down quarks:

$$
\begin{pmatrix} d' \\ s' \\ b' \end{pmatrix}_L = V \begin{pmatrix} d \\ s \\ b \end{pmatrix}_L , \tag{1.12}
$$

where the primed quarks are the mass eigenstates and the others are the flavor eigenstates. V is the Cabibbo-Kobayashi-Maskawa (CKM) matrix [11, 12], which contains one free imaginary phase, being the source of the CP violation, and three free real angles.

The CKM matrix is usually written as

$$
\begin{pmatrix} V_{ud} & V_{us} & V_{ub} \\ V_{cd} & V_{cs} & V_{cb} \\ V_{td} & V_{ts} & V_{tb} \end{pmatrix} \tag{1.13}
$$

so that the entries are labeled by the quark flavors. The probability of the transition from a quark i to a quark j is therefore proportional to $|V_{ij}|^2$. The CKM elements are fundamental parameters of the SM that need to be accurately determined from experiments.

A convenient parametrization of the CKM matrix is the Wolfenstein approximation [13]:

$$
V_{CKM} = \begin{pmatrix} 1-\frac{1}{2}\lambda^2 & \lambda & A\lambda^3(\rho-i\eta) \\ -\lambda & 1-\frac{1}{2}\lambda^2 & A\lambda^2 \\ A\lambda^3(1-\rho-i\eta) & -A\lambda^2 & 1 \end{pmatrix} \tag{1.14}
$$

The unitarity of the CKM matrix imposes six equations that can be interpreted as unitarity triangles in the complex plane. Measuring the parameters of the unitarity triangle serves two purposes: first, to determine some fundamental parameters of the Standard Model, and secondly, to test whether the CKM mechanism of flavor and CP violation is indeed correct, or whether there are hints of deviations from the Standard Model.

There is a plethora of ways in which the sides and angles of the unitarity triangle have been constrained [14] and the most recent experimental results

are represented on the $\bar{\rho}\,\bar{\eta}$ plane in Fig.1.2. Until now no significant deviations from the CKM mechanism have been established.
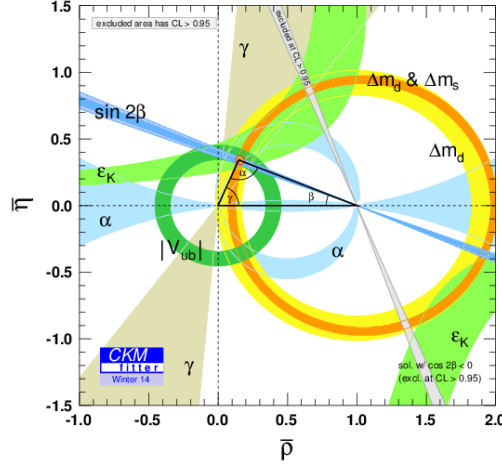

Figure 1.2: Unitarity triangle constraints in the $(\bar{\rho}, \bar{\eta})$ plane [15].

1.1.3 The QCD sector

The dynamics of the quarks and gluons are controlled by the QCD Lagrangian. QCD is described by the SU(3)$_C$ symmetry group, which has eight massless spin-one gauge bosons, the gluons, carrying color charge and self-interacting.

The QCD Lagrangian is:

$$L_{QCD} = -\frac{1}{4}F^a_{\mu\nu}F^{a\ \mu\nu} + \sum_{\{q\}}\bar{q}(i\gamma^\mu D_\mu - m_q)q, \tag{1.15}$$

where $\{q\} = u, d, s, c, b, t$, D_μ is the covariant derivative $D_\mu = \delta_\mu - iT^a A^a_\mu$ and $F^a_{\mu\nu} = \delta_\mu A^a_\nu - \delta_n u A^a_\mu + gf^{abc}A^b_\mu A^c_\nu$. f^{abc} are the structure constants of SU(3) and T^a form a basis of the fundamental representation of the SU(3) algebra.

Being a non-Abelian gauge theory, the physical spectrum consists of color singlet states only. The simplest of these states are mesons, formed by a quark-antiquark pair ($q\bar{q}$), and baryons, formed by three quarks ($q_1 q_2 q_3$). Recently discovered resonances [16, 17] not belonging to the standard spectra of the c and b quarks can be interpreted as bound states of four quarks (or quark molecules).

Another important property of QCD is the asymptotic freedom, which means that quarks and gluons have very weak interactions at short distances and high energy scale. This follows from the behavior of the QCD effective coupling constant $\alpha_s(q)$ as function of the momentum transfer q (see Fig.1.3). At high q (short distances), $\alpha_s(q)$ vanishes: quarks and gluons interact very weakly and a perturbative expansion in α_s can be performed. On the other hand, at values of q comparable to the QCD scale Λ_{QCD} (high distances), the strong interaction amplitude becomes so large that quarks cannot behave as free particles ("confinement") and perturbation theory is no longer suitable.
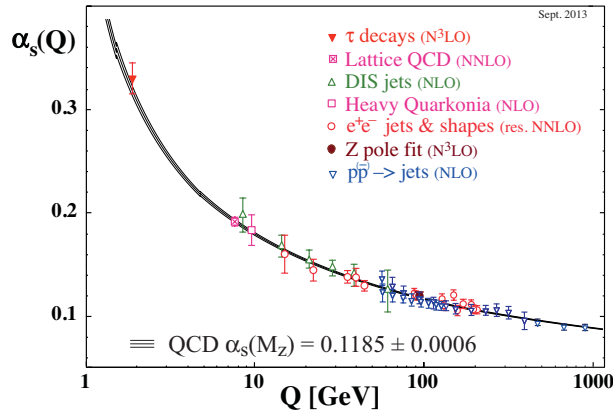
Figure 1.3: Summary of measurements of α_s as a function of the energy scale Q from [18]. The legend indicates the kind of measurement and the degree of QCD perturbation theory used in the extraction of α_s.

Quarks are conventionally divided into light ($m_q \ll \Lambda_{QCD} \approx 200$ MeV) and heavy ($m_q \gg \Lambda_{QCD}$), as summarized in Table 1.2.

	u	$m_u = 2.3$ MeV
Light quarks	d	$m_d = 4.8$ MeV
	s	$m_s = 95$ MeV
	c	$m_c = 1.275$ GeV
Heavy quarks	b	$m_b = 4.2$ - 4.6 GeV
	t	$m_t = 173.2$ GeV

Table 1.2: Masses of the six quarks, as evaluated in [18], where details on their extraction are reported.

Strong interactions of hadrons containing heavy quarks are easier to understand than those of hadrons containing only light quarks. For heavy quarks the effective coupling constant $\alpha_s(m_Q)$ is small, implying that on length scales comparable to $1/m_Q$ the strong interactions are perturbative and much like the electromagnetic interactions, therefore easier to handle.

1.2 Theoretical tools for B physics

Weak decays of hadrons containing heavy quarks are employed for tests of the Standard Model and measurements of its parameters. In particular, they offer the most direct way to determine the weak mixing angles, to test the unitarity of the CKM matrix, and to explore the physics of CP violation. Possibly, hints of New Physics beyond the Standard Model will be provided.

The structure of weak interactions in the Standard Model has been already formulated in Eq.1.8, where J_μ^+ can be also written in an explicit form as:

$$J_\mu^+ = (\bar{n}u_e, \bar{v}_m u, \bar{v}_\tau)\gamma_\mu \begin{pmatrix} e_L \\ \mu_L \\ \tau_L \end{pmatrix} + (\bar{u}_L, \bar{c}_L, \bar{t}_L)\gamma_\mu V_{CKM} \begin{pmatrix} d_L \\ s_L \\ b_L \end{pmatrix} \qquad (1.16)$$

At low energies, the charged-current interaction gives rise to local four-fermion couplings of the form

$$L_{eff} = -2\sqrt{2}G_F J^{+\mu}J_\mu^-, \qquad (1.17)$$

where G_F is the Fermi constant.

According to the structure of the charged-current interaction, weak decays of hadrons can be divided into three classes: leptonic decays, in which the quarks of the decaying hadron annihilate each other and only leptons appear in the final state; semi-leptonic decays, in which both leptons and hadrons appear in the final state; and non-leptonic decays, in which the final state consists of hadrons only.

However, the simplicity of the weak interactions is overshadowed by the complexity of the strong interactions responsible for the binding of quarks inside hadrons through gluon exchange. Thus, weak decays also serve as a probe of the least understood strong-interaction phenomenology: the confinement of quarks and gluons inside hadrons. Fig.1.4 shows a picture of a non-leptonic decay, where the effects of the strong interaction are also depicted.

Therefore, in order to fully understand weak meson decays the interplay between weak and strong interactions has to be addressed.
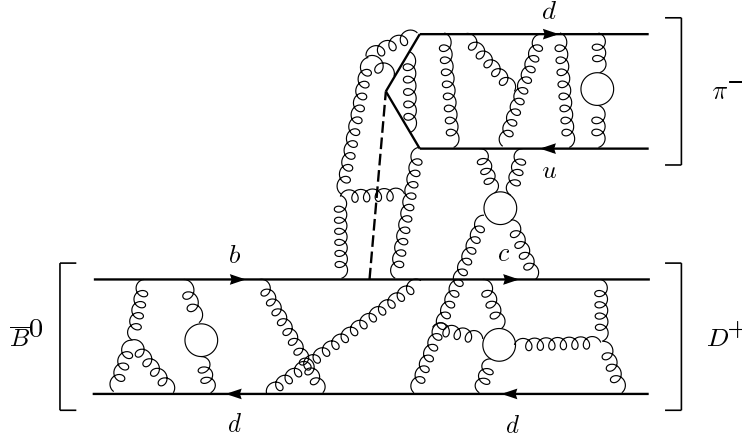
Figure 1.4: Representation of a non-leptonic *B* meson decay, showing also the gluon exchanges between the quarks.

The formal framework to achieve this is provided by the operator product expansion (OPE) [19]. The main feature of the OPE is that it allows to separate long distance physics, which incorporates the physics of hadronic states, from short distance phenomena, responsible for the flavor structure, and to face them independently.

Consider the amplitude M for the weak B meson decay process into some final state f. Using the OPE formalism, the amplitude can be represented as

$$M = -\frac{4G_F}{\sqrt{2}} V_{CKM} \sum_i C_j(\mu)\langle f | O_j(\mu)|B\rangle \left[1 + O\left(\frac{m_b^2}{M_W^2}\right)\right] \qquad (1.18)$$

where μ is the factorization scale. Physics from distances shorter than $1/\mu$ (masses $\gg \mu$) is contained in the Wilson coefficients C_j, and physics from distances longer than μ is accounted for by the hadronic matrix elements $\langle f | O_j | B\rangle$ of the local operators O_j.

The renormalization scale μ separating the two regimes is typically chosen to be of the order of a few GeV for B meson decays. The physical amplitude M cannot depend on μ. The μ dependence of the Wilson coefficients has to cancel the μ dependence present in O_j. This cancellation of μ dependence generally involves several terms in the expansion.

The short distance part in Eq.1.18 (the Wilson coefficients C_j) can be analyzed systematically using well established field theoretical methods. Due to the asymptotic freedom property of QCD, the strong interaction effects at short-

distances are calculable in perturbation theory in the strong coupling $\alpha_s(\mu)$. In fact $\alpha_s(\mu)$ is small enough in the full range of relevant short distance scales to serve as expansion parameter.

However, large logarithms $\ln(M_W/\mu)$ multiply $\alpha_s(\mu)$ in the calculation of the C_j's, spoiling the validity of the usual perturbation series. It is therefore necessary to perform a renormalization group analysis which allows an efficient summation of logarithmic terms to all orders in perturbation theory.

In this way the usual perturbation theory is replaced by the renormalization group improved perturbation theory in which the leading order (LO) corresponds to summing the leading logarithmic terms $\sim (\alpha_s \ln(M_W/\mu))^n$. Then at next-to-leading order (NLO), all terms of the form $\sim \alpha_s(\alpha_s \ln(M_W/\mu))^n$ are summed in addition, and so on.

The long-distance part in Eq.1.18 (the set of operators O_j) deals with low energy strong interactions and therefore poses a very difficult problem. In fact, at long distances, of order $1/\Lambda_{QCD}$, quarks and gluons hadronize and QCD becomes nonperturbative. Many approaches have been used to address the calculation of the long-distance part.

So far Lattice Gauge Theory [4] constitutes the only known entirely nonperturbative regularisation scheme. It relies on stochastic methods, which simulate gauge theories on a lattice, and allows to predict properties of interacting QCD matter. Such simulations have provided convincing evidence and the accuracy of the results has been improving with the more powerful computers and advanced numerical techniques. However, present computing power is still limited and only achieves solving, with a satisfactory precision, relatively simple problems.

Other approaches, like 1/N expansion, QCD and hadronic sum rules or chiral perturbation theory, have been used to obtain qualitative insight of relevant hadronic matrix elements. An alternative approach takes advantage of the existence of a hierarchy of scales by substituting QCD with simpler but equivalent Effective Field Theories (EFTs), whose idea is briefly exposed in the next Section.

Despite the numerous efforts, the problem of long-distance interactions is not yet solved satisfactorily.

1.2.1   Effective Field Theories

An EFT is a quantum field theory that contains the relevant degrees of freedom to describe phenomena in certain limited range of energies and momenta, and contains an intrinsic energy scale Λ that sets the limit of its applicability.

Typically, one integrates out the higher energy scales so that the Lagrangian of the EFT can be organized as a series of operators over powers of these scales. Each operator has a matching coefficient in front, which encodes the remaining information on the higher energy scales.

In general, an EFT is non-renormalizable, but it can be made finite to any finite order in $1/\Lambda$ by renormalizing the coefficients in front of the operators in the Lagrangian until that order.

The prototype of EFT for heavy quarks is the Heavy Quark Effective Theory (HQET) [20], which is the EFT of QCD suitable to describe systems with one heavy quark. These systems are characterized by two energy scales, m_Q and Λ_{QCD}, and the theory is developed as a systematic expansion in powers of Λ_{QCD}/m.

Bound states of two heavy quarks (*heavy quarkonia*) are a rather unique laboratory. They are characterized by the existence of a hierarchy of energy scales, which can be exploited to construct nonrelativistic effective field theories (NR EFT). As nonrelativistic systems, quarkonia involve three energy scales: the scale of the mass m (hard scale), the scale of the momentum transfer $p \sim m_Q v$ (soft scale) and the scale of the kinetic energy of the two heavy quarks in the centre-of-mass frame $E \sim p^2/m_Q \sim m_Q v^2$ (ultrasoft scale). Heavy quarkonia includes $\bar{c}c$ (charmonia), $\bar{b}b$ (bottomonia) and the open flavor $\bar{b}c$ states.

The Nonrelativistic QCD effective theory (NRQCD) [21, 22] exploits the hierarchy $m_Q \gg m_Q v$. By integrating out modes of energy and momentum m_Q from QCD Green functions, NRQCD enables the factorization of nonperturbative contributions into the expectation values or matrix elements of few operator. These contributions can then be evaluated on the lattice, extracted from the data or calculated in QCD vacuum models.

Chapter 2

The B_c meson

This Chapter presents the theoretical and experimental status of the physics of the B_c meson. After a general overview, B_c production and decay properties are discussed. A short Section about the simulation software follows. The current experimental scenario is examined in the last part of the Chapter.

The B_c meson, the ground state of the $\bar{b}c$ system, is the lightest meson consisting of two heavy quarks of different flavors.

Being a double heavy-quark-antiquark bound state, the $\bar{b}c$ state is similar to the charmonium ($\bar{c}c$) and bottomonium ($\bar{b}b$) systems. In fact, the B_c meson bound-state dynamics can be treated in the non-relativistic expansion by QCD-inspired effective models worked out for the charmonium and bottomonium states. The $\bar{b}c$ system is indeed the ideal laboratory to test the self-consistency of these models, whose parameters have been fixed from the fit to charmonia and bottomonia data.

However, since it carries flavor, the B_c meson has some specific production and decay peculiarities. First, the production mechanism for the $\bar{b}c$ system is different from that for the $\bar{c}c$ and $\bar{b}b$ systems, because it requires the production of two heavy quark-antiquark pairs. The $\bar{b}c$ production cross section is lower than that for hidden-flavour quarkonia, because the leading-order diagrams are of higher order in the coupling constants and the phase-space is suppressed owing to the presence of the additional heavy quarks.

Also, being an open flavor state, the B_c meson decays via the weak interaction. Thus, differently from the other heavy quarkonia, the B_c meson is a long-living particle; on the other hand, its lifetime is shorter than that of the other B mesons, since both the constituent quarks compete in the decay. Therefore, the study of B_c decays is of particular interest to improve the understanding of QCD

23

dynamics and the measurement of the parameters of the weak Lagrangian. An accurate measurement of the B$_c$ lifetime can also provide information on the masses of charm and beauty quarks.

2.1 The ($\bar{b}c$) mass spectrum

The $\bar{b}c$ states have a rich spectroscopy of orbital and angular-momentum excitations. Sixteen narrow states are expected below the threshold of the decay into a (B D) pair. Having no strong or electromagnetic annihilation decay channel, the excited $\bar{b}c$ levels cascade down into the ground pseudoscalar state by radiating photons and pion pairs. This results in a total width of $\bar{b}c$ excited states that is two orders of magnitude less than the total width of the charmonium and bottomonium excited levels, for which the annihilation channels are essentials [23].

The spectrum and properties of the $\bar{b}c$ family are predicted by non-relativistic potential models [24, 25], perturbative QCD [26], and lattice calculations [27, 28, 29]. Fig. 2.1 shows the predicted mass spectrum of the $\bar{b}c$ system, accounting for the spin-dependent splittings. Before the advent of the LHC, only the ground state of the $\bar{b}c$ system had been observed.
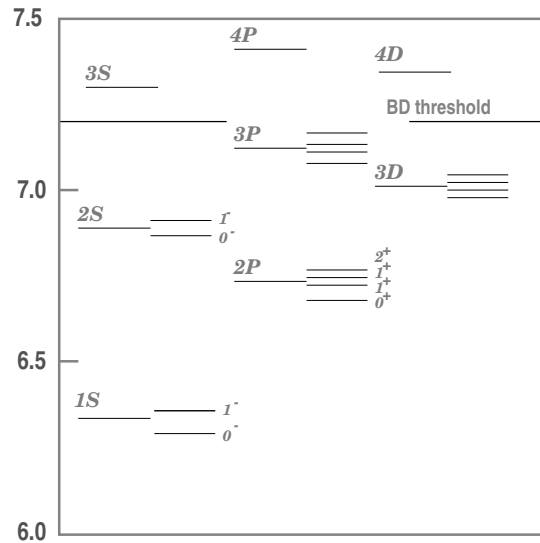

Figure 2.1: Predicted $\bar{b}c$ mass spectrum [30].

2.2 B_c **production**

The B_c production mechanisms are completely different from those for hidden-flavor quarkonia. In fact, the electromagnetic and hadronic production of B_c mesons requires the joint production of the two additional heavy quarks ($\bar{c}$ and b). This explains the low value of the B_c production cross section in comparison with the production cross section of particles from the ψ and Υ families. On the other hand, the absence of B_c decay channels into light hadrons because of the strong interactions implies that all higher-mass bound $\bar{b}c$ states below the (B D) threshold decay through hadronic and electromagnetic transitions into the lowest state with a probability close to unity.

Thus, the B_c production can be thought as a process composed of three steps: a $\bar{b}b$ and a $\bar{c}c$ pair are first created by parton collision. Second, a $\bar{b}$ and a $\bar{c}$ quark bind to form the B_c meson in its ground state or in one of its excited states. Finally, the excited states cascade down to the ground state. Therefore the total production cross section for B_c is the sum of the direct production cross sections for B_c and its excited states.

The description of the direct production of the B_c meson is based on the factorization of hard parton production of heavy quarks ($\bar{b}b,\bar{c}c$) and soft coupling of ($\bar{b}c$) bound state. In the first stage, the hard subprocess can be reliably calculated in the framework of QCD perturbation theory, while in the second stage the quark binding in the heavy quarkonium can be described in the non-relativistic potential model approach.

The differential cross section for producing the $\bar{b}c$ state B_c in a hadron collision can be written as [31]:

$$d\sigma[h_A h_B \to B_c + X] = \sum_{ij} \int dx_1 dx_2 f_i^{h_A}(x_1,\mu) f_j^{h_B}(x_2,\mu)[d\hat{\sigma}(ij \to B_c + X)],$$

(2.1)

where f_i are the parton distribution functions (PDF) of the incoming hadrons h_A and h_B, the sum is over the partons i and j in the initial state hadrons and μ is the renormalization/factorization scale. The cross section $d\hat{\sigma}(ij \to B_c + X)$ for the direct production of $\bar{b}c$ by the collision of partons i and j is the sum of products of short-distance cross sections and long-distance matrix elements:

$$d\hat{\sigma}[ij \to B_c + X] = \sum_n d\hat{\sigma}[ij \to (\bar{b}c)_n + X]\langle O^H(n)\rangle,$$

(2.2)

where the sum is over 4-fermion operators that create and annihilate the $\bar{b}c$. The nonperturbative matrix element $\langle O^H(n)\rangle$ encodes the probability for a $(\bar{b}c)_n$

to evolve into the B$_c$ state and scales as a definite power of the relative velocity v of the charm quark. For S-wave states, the leading color-octet matrix element is suppressed by v^4 relative to the leading color-singlet matrix element. For P-wave states, the leading color-singlet matrix element and the leading color-octet matrix element are both suppressed by v^2 relative to the leading color-singlet matrix element for S-waves.

The short-distance cross section $d\hat{\sigma}[ij \to (\bar{b}c)_n + X)]$ for creating the $\bar{b}c$ in the color and angular-momentum state n can be calculated as a perturbative expansion in α_s at scales of order m_c or larger.
The lowest order mechanisms for creating the $(\bar{b}c)$ are the order-α_s^4 processes $q\bar{q}$, gg $\to(\bar{b}c) + b\bar{c}$. At the LHC, the dominant contribution comes from the gluon-gluon process, which is described by 36 Feynman diagrams. The typical Feynman diagrams are plotted in Fig. 2.2. This process can create the $\bar{b}c$ in either a color-singlet or color-octet state. The cross section for color-octet $\bar{b}c$ is expected to be about a factor of 8 larger than for color-singlet $\bar{b}c$ (from counting the color states), which can partially compensate for suppression factors embedded in the matrix element. In contrast to the case for the production of hidden-flavor quarkonia, there is no dynamical enhancement of the short-distance coefficients of the color-octet $\bar{b}c$ at low or at high p_T. Color-octet production processes should therefore be less important for $\bar{b}c$ mesons than for quarkonium, and all existing calculation for the cross sections of $\bar{b}c$ mesons have been carried out within the color-singlet model.

Two approaches have been used to compute $d\hat{\sigma}[ij \to (\bar{b}c)_n + X)]$: the complete order-$\alpha_s^4$ approach and the fragmentation approach [32, 33, 34, 35]. In the former, the parton cross-section is computed at leading order in α_s. Instead, the fragmentation approach is based on the fact that, for asymptotically large $p_T \gg m_{B_c}$, the parton cross-section can be further factorized into a cross-section for producing $\bar{b}b$ and a fragmentation function $D_{\bar{b} \to B_c}(z, \mu)$ that gives the probability for the $\bar{b}$ to fragment into a B$_c$ carrying a fraction z of the $\bar{b}$ momentum:

$$d\hat{\sigma}[ij \to B_c + X] \approx \int dz d\hat{\sigma}[ij \to \bar{b} + b]D_{b \to B_c}(z, \mu). \qquad (2.3)$$

This approach has the advantage of simple expressions for the $\bar{b}$ production cross-section and the fragmentation function $D_{\bar{b} \to B_c}$ of Eq.2.3. However, in Ref.[35, 36] it is proved that the fragmentation cross-section becomes an accurate approximation to the complete order-α_s cross-section only at very large p_T values. Therefore this approach is no longer considered in the following.
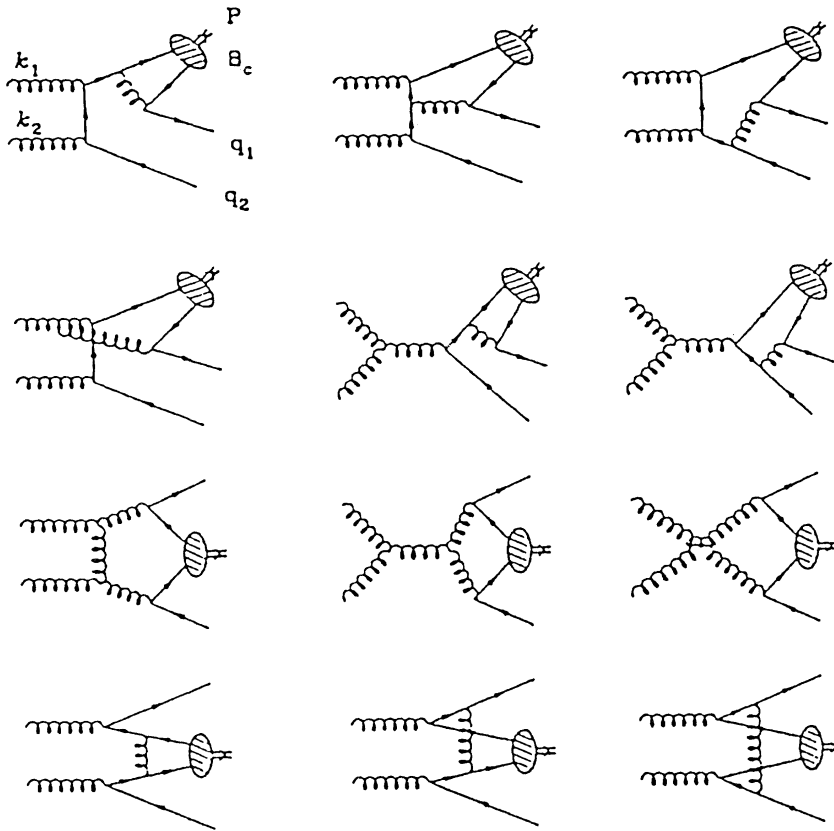
Figure 2.2: Feynman diagrams for the B_c production in gluon-gluon fusion.

2.2.1 Uncertainties on B$_c$ hadronic production

The inputs required to calculate the complete order-α_s^4 cross-sections are the masses m_b, m_c, and m_{B_c}, the decay constant F_{B_c}, the PDFs, the QCD coupling constant α_s, and the factorization scale μ.

The masses m_b and m_c are known with uncertainties of about 2.4% and 8%, respectively. In the NRQCD factorization approach, m_{B_c} and $m_{B_c^*}$ are set $= m_c + m_b$ in the short-distance coefficients (the binding energy is taken into account in contributions from operators of higher order in v).

The effect of the uncertainties on the quark masses on the estimate of the B$_c$ production cross section is evaluated by calculating the cross section with the allowed values of m_c and m_b, while fixing all the other parameters. The predictions for the direct B$_c$ production cross-section at the Tevatron and the LHC are summarized in Table 2.1 (2.2) for several values of m_c (m_b) and for typical values for the other parameters [31]. Due to the strong dependence on the collision energy, the hadronic production cross-section for B$_c$ mesons at the LHC is larger than at the Tevatron by a factor of about 16. The cross section decreases by 10-20% for m_b steps of 0.2 GeV and m_c steps of 0.1 GeV.

	Tevatron ($\sqrt{s} = 2$ TeV)						LHC ($\sqrt{s} = 14$ TeV)					
m_c (GeV)	1.3	1.4	1.5	1.6	1.7	1.8	1.3	1.4	1.5	1.6	1.7	1.8
$\sigma[B_c]$ (nb)	4.84	3.87	3.12	2.56	2.12	1.76	75.6	61.0	49.8	41.4	34.7	28.9

Table 2.1: The total cross-section for hadronic B$_c$ production at the Tevatron and LHC for various values of m_c [31] and fixed b quark mass ($m_b = 4.9$ GeV). The gluon distribution function is CTEQ5L, the running of α_s is leading order, $\mu^2 = \hat{s}/4$, and $F_{B_c} = 480$ MeV.

	Tevatron ($\sqrt{s} = 2$ TeV)					LHC ($\sqrt{s} = 14$ TeV)				
m_b (GeV)	4.5	4.7	4.9	5.1	5.3	4.5	4.7	4.9	5.1	5.3
$\sigma[B_c]$ (nb)	4.10	3.55	3.12	2.70	2.38	63.4	56.2	49.8	44.1	39.6

Table 2.2: The total cross-section for hadronic B$_c$ production at the Tevatron and LHC for various values of m_b [31] and fixed c quark mass ($m_c = 1.5$ GeV). The gluon distribution function is CTEQ5L, the running of α_s is leading order, $\mu^2 = \hat{s}/4$, and $F_{B_c} = 480$ MeV.

An experimental measurement of the decay constant F_{B_c} is not available, therefore values obtained from potential models [24, 37, 38] or from lattice gauge theory [39] are used. The uncertainty on the factor $F_{B_c}^2$ is about 6%.

The largest uncertainties in the theoretical predictions arise from the factor $\alpha_s^4(\mu)$. There is a large ambiguity in the choice of the scale μ, since the short-distance process involves several scales, including m_c, m_b, and p_T. The sensitivity to the choice of μ could be decreased by carrying out a complete calculation of the production cross-section at next-to-leading order in α_s, but this is, at present, prohibitively difficult. Fig. 2.3 shows the differential cross-sections for B$_c$ production as a function of the B$_c$ transverse momentum and rapidity at the Tevatron and the LHC, using four different prescriptions for the scale μ [31]. At central rapidity, the variations among the four choices of scale is about a factor of three at the Tevatron and a factor of two at the LHC.

The total uncertainty from combining all of the uncertainties in the direct cross-section for B$_c$ production is less than an order of magnitude.
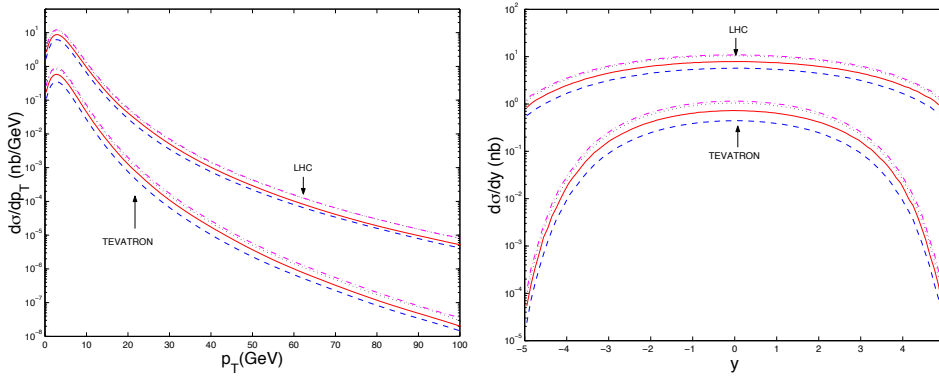

Figure 2.3: The differential cross-sections for B$_c$ direct production as a function of its transverse momentum and rapidity at the Tevatron ($\sqrt{s} = 2$ TeV) and at the LHC ($\sqrt{s} = 14$ TeV) for four choices of the scale: $\mu^2 = \hat{s}/4$ (solid line), $\mu^2 = p_T^2 + m_{B_c}^2$ (dotted line), $\mu^2 = \hat{s}$ (dashed line), and $\mu^2 = p_{Tb}^2 + m_b^2$ (dash-dot line). The gluon distribution is CTEQ5L, the running of α_s is leading order, $F_{B_c} = 480$ MeV, $m_c = 1.5$ GeV, and $m_b = 4.9$ GeV [31].

2.2.2 Inclusive cross-section

So far I have discussed predictions for the direct production of the B$_c$. What can be measured experimentally is the inclusive cross-section, including the feeddown from all of the higher states of the $\bar{b}c$ system. The excited states below the (B D) threshold (an additional S-wave multiplet, one or two P-wave multiplets, and a D-wave multiplet) all cascade down to the ground state B$_c$.

Since the B$_c$* decays into the B$_c$ with a probability of almost 100%, and its direct production cross section is $\sim$ 2.4 larger than that of the ground state [31], the feeddown from directly-produced B$_c$* s increases the cross-section for the B$_c$ by about a factor of 3.4. Applying the complete order-α_s^4 calculation for B$_c$ and B$_c$* cross-sections to the 2S multiplet, the contribution of their feeddown can be evaluated. The inclusive cross-section for B$_c$ production, including the effect of feeddown from the direct production of all of the S-wave B$_c$ states, is larger than the cross-section for direct B$_c$ production by a factor of about 5.4 [47].

Quantitative predictions for the contribution to the inclusive B$_c$ production cross-section from the feeddown from P-wave states are not available so far.

In summary, the order-α_s colour-singlet production cross-section for S-wave $\bar{b}c$ mesons can be used to predict the B$_c$ production cross-section, including feeddown from excited S-wave states. The uncertainty in the normalization of that prediction is less than an order of magnitude. A measurement of the inclusive cross-section for B$_c$ production much larger than the prediction could indicate that there is a large contribution from the feeddown from P-wave or higher-orbital-angular-momentum states. It could also indicate that the colour-octet contributions to the direct production of the B$_c$ and the B$_c$* are important.

2.3   B$_c$ **decays and lifetime**

As mentioned before, the B$_c$ meson is a particular state, because both quarks compete in the decay. In fact, three classes of transitions can be identified:

1. the decay of the $\bar{b}$-quark with the spectator c quark

2. the decay of the c-quark with the spectator $\bar{b}$ quark

3. the annihilation of $\bar{b}$ with c, which results in $B_c^+ \to l^+ \nu_l (c\bar{s}, u\bar{s})$, where $l = e, \mu, \tau$.

In the $\bar{b} \to \bar{c}c\bar{s}$ decays one separates also the Pauli Interference (PI) with the c quark from the initial state. The corresponding quarks diagrams are shown in Fig.2.4. The total decay width is therefore the sum over the partial widths:

$$\Gamma(B_c \to X) = \Gamma(b \to X) + \Gamma(c \to X) + \Gamma(ann.) + \Gamma(PI). \qquad (2.4)$$

The dominant contribution to the B$_c$ lifetime is expected to be given by the c-quark decays ($\approx$70%), while the b-quark decays and the weak annihilation are expected to add about 20% and 10%, respectively, and the Pauli interference
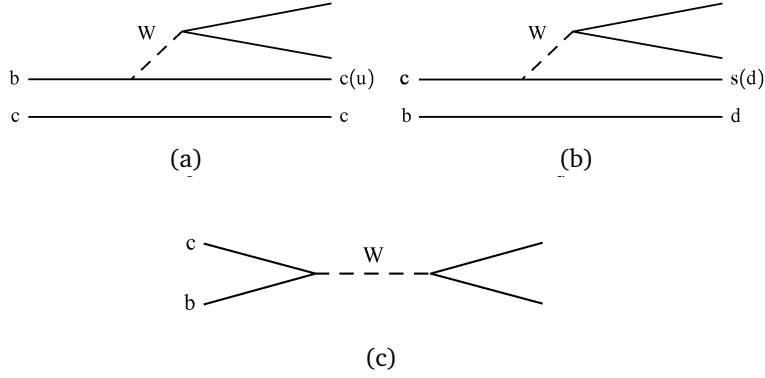
Figure 2.4: Quark diagrams for the B$_c$ meson decays: (a) the c-spectator decay; (b) the b-spectator decay; (c) the annihilation.

term gives a valuable contribution in the $\bar{b} \to \bar{c}c\bar{s}$ decays at the level of -1.5% (already included in the b-quark decay fraction) [40].

In order to evaluate the contribution to the B$_c$ decay width from the first two classes, the operator product expansion (OPE) approach for the quark currents of weak decays [41, 42] can be applied. In this method, one first estimates the α_s-corrections to the free quark decays and uses quark-hadron duality [43] for the final states. Then the matrix element for the transition operator in the bound meson state is considered, taking into account the effects caused by the motion and virtuality of decaying quark inside the meson because of the inter-action with the spectator. In this way the $\bar{b} \to \bar{c}c\bar{s}$ decay mode turns out to be suppressed almost completely due to the Pauli interference with the c-quark from the initial state. The c-quark decays with a spectator $\bar{b}$ are also suppressed compared to the decay of a free c-quark, because of the large binding energy of the initial state. Possible effects of interference between the leading-order weak amplitudes and the penguin corrections in B$_c$ decays were considered in the framework of OPE in Ref. [44], and these corrections were estimated to be about 4%.

The annihilation width is the sum of the widths from the annihilation of the $\bar{b}c$ state into quarks and leptons. When studying the annihilation into quarks, one must take into account the hard-gluon corrections to the effective four-quark interaction of weak currents, which give an enhancement factor $a_1 = 1.22 \pm 0.04$. The nonperturbative effects of QCD can be absorbed into the leptonic decay constant $f_{B_c} \approx 400$ MeV. This estimate of the contribution from annihilation into quarks does not depend on a hadronization model, since a

large energy release, of the order of the meson mass, takes place.

Because of helicity suppression, the decay width is proportional to the square of the masses of leptons or quarks in the final state, so that the contributions from light leptons and quarks can be neglected. Thus, the only important annihilation channels are $\bar{b}c \to \tau^+ \nu_\tau$ and $\bar{b}c \to c\bar{s}$.

To calculate inclusive widths in the potential model approach, it is necessary to sum up the widths of exclusive decay modes. For semileptonic decays of the b quark ($\bar{b} \to \bar{c}l^+ \nu_l$), the hadronic final state is almost completely saturated by the lightest bound states in the $\bar{c}c$ system, i.e. the 1S states η_c and J/ψ. For semileptonic decays of the c quark ($c \to sl^+ \nu_l$), the only $\bar{b}s$ states that can enter the accessible energy gap are B_s and B_s^*.

The results of the calculation of the B$_c$ total width in the inclusive OPE and exclusive potential model approaches give values that are consistent with each other, if one takes into account the most significant uncertainty, which is related to the choice of the quark masses (especially of the charm quark). The predicted B$_c$ lifetime is

$$\tau_{B_c}^{OPE,PM} = 0.55 \pm 0.15 \; ps. \tag{2.5}$$

The OPE estimates of inclusive decay rates agree with semi-inclusive calculations in the sum rules of QCD and NRQCD [45, 46], where the saturation of hadronic final states by the ground levels in the $\bar{c}c$ and $\bar{b}s$ systems is assumed, as well as the factorization that allows to relate the semileptonic and hadronic decay modes. Predictions from the three approaches are summarized in Table 2.3.

In contrast to OPE, where the heavy quark masses are the major source of uncertainty, masses are fixed in the SR approach. The accuracy of SR calculations for the total width of the B$_c$ is indeed determined by the choice of the scale μ for the hadronic weak Lagrangian in the decays of c quarks. The dependence on the choice of the μ scale is shown in Fig. 2.5, where μ is varied between $m_c/2$ and m_c. The dark shaded region corresponds to the scales preferred by the data on the charmed meson lifetimes.

2.3.1   Semileptonic and leptonic modes

The semileptonic decay rates are estimated in Ref.[46] using the sum rule approach and taking into account large Coulomb-like corrections for the heavy quarkonium in the initial state. The widths and branching fractions calculated using QCD sum rules are summarized in Table 2.4.

In practice, the most useful semileptonic decay modes are those with a J/ψ in the final state, which is easily detected in experiments via its leptonic decays.

B$_c$ decay mode	OPE, %	PM, %	SR, %
$\bar{b} \to \bar{c}l^+\nu_l$	3.9 ± 1.0	3.7 ± 0.9	2.9 ± 0.3
$\bar{b} \to \bar{c}u\bar{d}$	16.2 ± 4.1	16.7 ± 4.2	13.1 ± 1.3
$\sum \bar{b} \to \bar{c}$	25.0 ± 6.2	25.0 ± 6.2	19.6 ± 1.9
$c \to sl^+\nu_l$	8.5 ± 2.1	10.1 ± 2.5	9.0 ± 0.9
$c \to su\bar{d}$	47.3 ± 11.8	45.4 ± 11.4	54.0 ± 5.4
$\sum c \to s$	64.3 ± 16.1	65.6 ± 16.4	72.0 ± 7.2
$B_c^+ \to \tau^+\nu_\tau$	2.9 ± 0.7	2.0 ± 0.5	1.8 ± 0.2
$B_c^+ \to c\bar{s}$	7.2 ± 1.8	7.2 ± 1.8	6.6 ± 0.7

Table 2.3: The branching ratios of the B$_c$ decay modes calculated in the framework of inclusive OPE approach, by summing up the exclusive modes in the potential model and according to the semi-inclusive estimates in the sum rules of QCD and NRQCD [47].
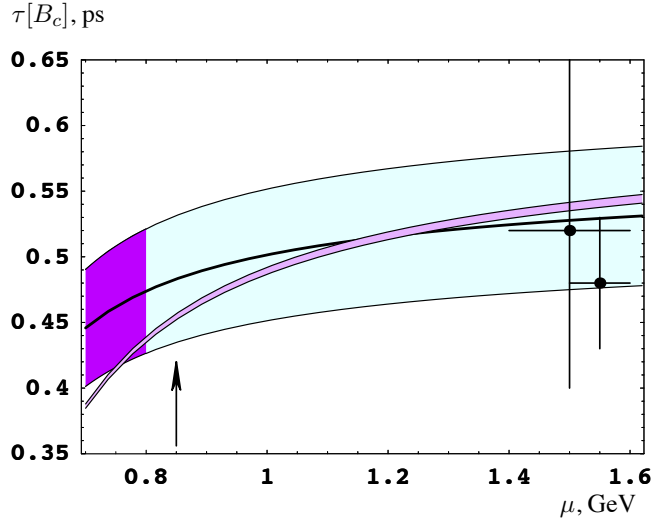

Figure 2.5: The B$_c$ lifetime calculated in QCD SR versus the scale μ. Wide shaded region: uncertainty of the semi-inclusive estimates [46]; violet shaded region: preferable choice as given by charmed mesons lifetimes. Dots: values in the OPE approach from Ref. [41] (left point) and Ref. [42] (right point). Narrow shaded region: result of [40] obtained by summing up the exclusive channels with a variation of the hadronic scale in the decays of the $\bar{b}$ in the range $1 < \mu_b < 5$ GeV. Arrow: preferable prescription of μ = 0.85 GeV as discussed in [46].

The calculations for the B$_c$ exclusive semileptonic decay rates into 1S charmonium states obtained from QCD sum rules agree with the estimates from potential models, which, additionally, consider the contributions of decays to the excited 2S and 1P states. The direct decay rate into P-wave charmonium states turns out to be about 20% of the direct decay rate into the 1S states. The radiative decay of the χ_c states increases the total semileptonic decay rate of B$_c$ to J/ψ by about 5%.

Mode	Γ (10^{-14} GeV)	BR, %
$B_s e^+ \nu_e$	5.8	4.0
$B_s^* e^+ \nu_e$	7.2	5.0
$\eta_c e^+ \nu_e$	1.1	0.75
$\eta_c \tau^+ \nu_\tau$	0.33	0.22
$J/\psi e^+ \nu_e$	2.8	2.1
$J/\psi \tau^+ \nu_\tau$	0.7	0.51

Table 2.4: Widths and branching fractions for the semileptonic decay modes of the Bc meson calculated using QCD sum rules. The accuracy is about 10%. For branching ratios, τ_{B_c} is set to 0.46 ps.

Leptonic decays marginally contribute to the to the B$_c$ full width. Nevertheless, their analysis is of particular interest, both from the phenomenological and the theoretical point of view.

From the phenomenological side, B$_c$ annihilation modes are governed by V_{cb}; therefore they are Cabibbo-enhanced with respect to the analogous B_u decays, and represent new channels to access this matrix element.

From the theoretical viewpoint, the purely leptonic ($B_c \to l\nu$) and the radiative leptonic ($B_c \to l\nu\gamma$) transitions are interesting since, in the nonrelativistic limit of the quark dynamics, their rates can be expressed in terms of the decay constant f_{B_c}, providing alternative possibilities to measure it [48, 49].

The dominant leptonic B$_c$ decay is the B$_c \to \tau\nu_\tau$ mode. However, it has a low experimental efficiency of detection because of hadronic background in the τ decays and missing energy.

In the radiative modes, muon and electron channels are enhanced [48]. In fact, the additional photon removes the helicity suppression for the leptonic decay of a pseudoscalar particle, leading to an an increase of the muonic decay rate by a factor of two.

2.3.2 Nonleptonic modes

The nonleptonic weak decays are described in the SM by a single W boson exchange diagram at tree level. The hadronic decay widths can be obtained assuming the factorization of the weak transition between the quarkonia and the hadronization of products of the virtual W^{*+} boson decay.

The effective four-fermion Hamiltonian describing the nonleptonic decays $q_1 \to q_2, q_3$ has the form

$$
\begin{aligned}
\mathcal{H}_{eff}^{q_1 \to q_2(q_3)} = \frac{G_F}{\sqrt{2}} \{ & V_{q_2 q_1} [c_1(\mu) \mathcal{O}_1^{q_2 q_1} + c_2(\mu) \mathcal{O}_2^{q_2 q_1}] \\
+ & V_{q_3 q_1} [c_1(\mu) \mathcal{O}_1^{q_3 q_1} + c_2(\mu) \mathcal{O}_2^{q_3 q_1}] + h.c. \}
\end{aligned}
\tag{2.6}
$$

where G_F is the Fermi coupling constant and $V_{q_i q_1}$ are the CKM matrix elements. The effective weak Hamiltonian consists of products of local four-quark operators $\mathcal{O}_{1,2}$ renormalized at the scale μ, and scale-dependent Wilson coefficients $c_{1,2}(\mu)$, which incorporate the short-distance effects arising from the renormalization of $\mathcal{H}_{eff}$ from $\mu = m_W$ to $\mu = O(m_b)$. Without strong-interaction effects, one would have $c_1 = 1$ and $c_2 = 0$. However, gluon exchange modifies this result renormalizing the original weak vertices and thus inducing new types of interactions (such as the operators $\mathcal{O}_2$).

The formula above can be rearranged [50] to

$$
c_1 \mathcal{O}_1 + c_2 \mathcal{O}_2 = a_1 \mathcal{O}_1 + c_2 \tilde{\mathcal{O}}_2 = a_2 \mathcal{O}_2 + c_1 \tilde{\mathcal{O}}_1,
\tag{2.7}
$$

with

$$
a_1(\mu) = c_1(\mu) + \frac{1}{N_c} c_2(\mu), \quad a_2(\mu) = c_2(\mu) + \frac{1}{N_c} c_1(\mu),
\tag{2.8}
$$

where N_c is the number of colors and $\tilde{\mathcal{O}}_{1,2}$ are nonfactorizable color-octet current operators.

With this description, three classes of decays can be identified. The first class comprises color-favored tree diagrams and contains those decays in which only a charged meson is directly produced from a color-singlet current (Fig.2.6a); its amplitude is proportional to a_1. The second class is caused by a color-suppressed tree diagram and contains those decays in which only a neutral meson can be generated directly from a color-singlet current (Fig.2.6b); its amplitude is proportional to a_2. The third class of transitions consists of those decays in which both a_1 and a_2 amplitudes interfere (Fig.2.6c).

For processes of class I with b-quark decays, estimates from SR and potential model approaches are in good agreement. In contrast, the sum rule predictions
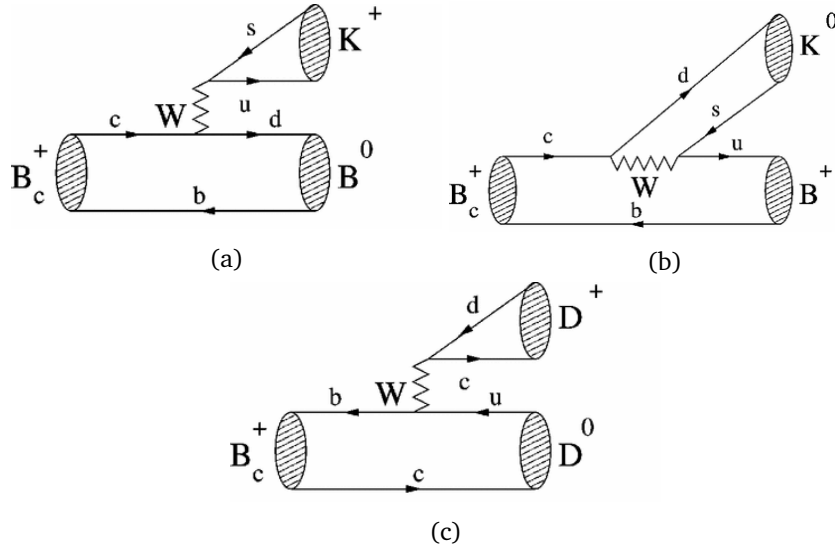
Figure 2.6: Quark diagrams for nonleptonic decays of the first (a), second (b) and third class (c), as defined in the text.

are significantly enhanced in comparison with the values calculated in potential models for transitions with color permutation, i.e., for class II processes. Finally, for class III transitions, where the interference is significantly involved, sum rule estimates for the squares of a_1 and a_2 are in agreement with the potential models. However, the authors of Ref. [30] found that the sign determination could be different between the two approaches. In particular, due to the negative value of a_2 with respect to a_1, they estimates that half of decays should be enhanced in comparison with the case of Pauli interference switched off, while the other half is suppressed, and they propose a list of the most sensitive decay modes where to test the Pauli interference.

For the widths of nonleptonic c-quark decays the sum rule estimates are typically greater than those of potential models and are consistent with the inclusive ones.

The measurement of branching fractions for the semileptonic and nonleptonic modes and their ratios can help examining the various theoretical approaches.

2.3.2.1   B$_c$ **decays into** J/ψ **+ pions**

In this Section we consider decays of the B$_c$ meson into pions and vector char-
monium J/ψ, that is $B_c \to J/\psi + n\pi$, where $n = 1, 2, 3, 4$. These are the B$_c$
decays studied in this thesis.

   These processes can be represented with the diagram in Fig. 2.7, where the
b-quark decays weakly with the emission of a W boson, which subsequently
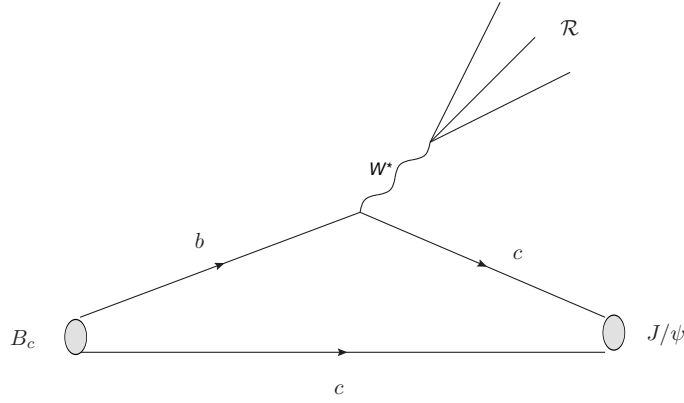decays into n pions (indicated as R in the figure).

Figure 2.7: Typical diagram for B$_c \to J/\psi + n\pi$ decays.

   According to QCD factorization, the amplitude of these processes splits into
two independent parts. The first factor describes the decay $B_c \to J/\psi W^*$ and
its amplitude is calculated using B$_c$ meson form factor parametrizations. The
second part concerns the fragmentation of the virtual W boson.

   A detailed calculation of the branching fractions of $B_c \to J/\psi + n\pi$ decays
is presented in Ref. [51]. In particular, the authors exploit the analogy with τ
lepton decays ($\tau \to \nu_\tau + n\pi$) to use existing experimental data to describe the
W fragmentation.

   Furthermore, they compute the branching fractions using different approaches
to derive the form factors. The first approach is based on the fact that the quark
velocity in the B$_c$ system is small, and nonrelativistic wave functions can be
used to describe the heavy quarkonium (quark model approach, QM). The sec-
ond approach is based on the high speed of the final state J/ψ in the B$_c$ rest
frame, which allows to expand the process amplitude in the powers of the small
parameters $M_{J/\psi}/M_{B_c}$ (light cone approach, LC). An alternative approach ob-
tain the form factors from QCD sum rules (SR approach). Predictions with the

different approaches are reported in Table 2.5.

Note that neutral pions in the final state are considered in the count of the number of pions, so that, e.g, 3π stands for the sum of $\pi^+\pi^0\pi^0$ and $\pi^+\pi^-\pi^+$ decay modes.

	π	2π	3π	4π
LC	0.13	0.35	0.52	0.26
QM	0.17	0.44	0.64	0.33
SR	0.17	0.48	0.77	0.40

Table 2.5: Branching fractions (in %) for $B_c \to J/\psi + n\pi$ decays for different sets of B_c meson form factors [51].

Predictions for the branching fractions of B_c decays with J/ψ plus pions in the final states are also available in Ref. [52], where the authors study the three-pion decay $B_c^+ \to J/\psi\pi^+\pi^+\pi^-$ assuming the dominant contribution of the intermediate axial-vector meson $a_1(1260)$ and vector meson $\rho(770)$ in the $\pi^+\pi^-\pi^+$ and $\pi^+\pi^-$ invariant mass distributions, respectively (see Fig. 2.8 for quark diagrams of the W decays). Their predictions for the branching fractions and their ratios are summarized in Table 2.6.

	π	3π	Ratio
LC	0.096	0.180	1.88
QM	0.111	0.207	1.87
SR	0.122	0.266	2.17

Table 2.6: Branching fractions (in %) for $B_c \to J/\psi + n\pi$ decays for different sets of B_c meson form factors and the predicted value of the ratio $B(B_c^+ \to J/\psi\pi^+\pi^+\pi^-)/B(B_c^+ \to J/\psi\pi^+)$ [52].
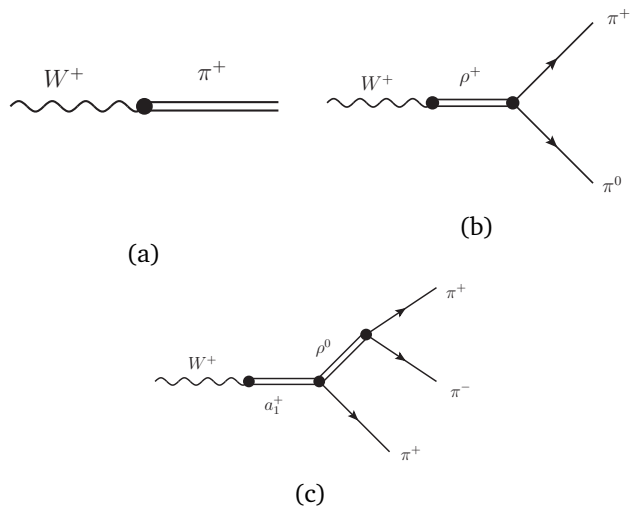
Figure 2.8: Typical diagrams for $W^* \to n\pi$ decays through the resonant states $\rho^0(770)$ (b) and $a_1(1260)$ (c).

2.4   The BCVEGPY generator

A dedicated event generator for the B_c meson, BCVEGPY [53][54], is used to enhance the simulation efficiency of B_c events, and overcome the low production rate due to the small B_c production cross section.

The B_c production rate, requiring both a $\bar{b}b$ and a $\bar{c}c$ couple, is in fact $\sim 10^{-3}$ compared to the single $\bar{b}b$ production. Thus, in PYTHIA simulation program[55], only one B_c meson is produced out of 10^6 pp interactions.

The BCVEGPY package emulates the hadronic production of B_c^+ mesons through the process $gg \rightarrow B_c + b + \bar{c}$, and is based on a complete calculation approach (full pQCD complete calculation at the lowest order α_s^4). Contributions from the quark pair annihilation production mechanism are neglected because they are highly suppressed in pp collision environment.

The BCVEGPY package is integrated in the CMS software and interfaced with PYTHIA (version 6.424, Z2 tune [56]), which hadronizes the whole event. Tunes differ in the treatment of parton radiation and hadronization, and in the choice of underlying event parameters including those regulating parton showers, color reconnections, and cutoff values for the multiple parton interaction mechanism. Values of these parameters were chosen to provide a reasonable description of existing LHC pp differential data measured in minimum-bias and hard QCD processes.

Unstable particle decays are simulated with EVTGEN [57] and the detector response with GEANT4 [58].

2.5   Experimental scenario

Before the advent of the LHC, experimental measurements were limited to semileptonic channels and the fully reconstructed decays $B_c^+ \rightarrow J/\psi \pi^+$. The former has the advantage of a larger branching fraction and statistics (the theoretical prediction is $\mathrm{B}(B_c^+ \rightarrow J/\psi \pi^+) \sim 0.13\%$, $\mathrm{B}(B_c^+ \rightarrow J/\psi \mu^+ \nu_\mu) \sim 1.9\%$, see below for the recent measurement from the LHCb experiment [73]), but it is not kinematically close, while the latter provides a precise determination of the mass, but a lower rate.

The first observation of the B_c meson was made by the CDF Collaboration in 1998 in the semileptonic decay $B_c^+ \rightarrow J/\psi l^+ \nu_l$ $(l = e, \mu)$ [59, 60]. The production cross times branching fraction for this decay relative to that for $B^+ \rightarrow J/\psi K^+$ was measured to be $0.132^{+0.041}_{-0.037}\,(\mathrm{stat}) \pm 0.031\,(\mathrm{syst})^{+0.032}_{-0.020}\,(\mathrm{lifetime})$ for B_c^+ and B mesons with transverse momenta $p_T > 6$ GeV and rapidities $|y| < 1$. This result is shown in Fig.2.9.
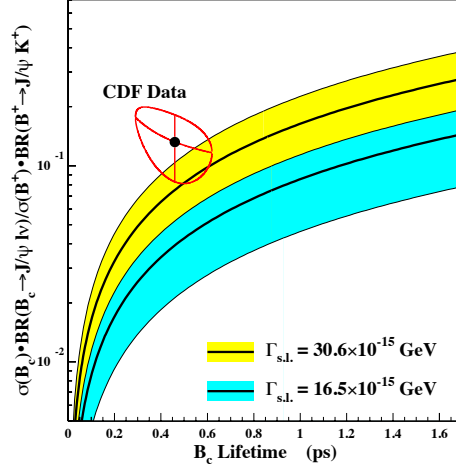
Figure 2.9: Measurement from the CDF experiment of the cross section times branching fraction ratio (point) with 1-standard-deviation contour plotted at the measured value of the BC lifetime. The shaded region represents two different theoretical predictions and their uncertainties. For further details, see Ref.[59].

Both the CDF and the D0 experiments measured the mass of the B_c exploiting the fully reconstructed $B_c^+ \to J/\psi\pi^+$ channel, obtaining $6275.6\pm2.9(\text{stat})\pm2.5(\text{syst})$ [61] and $6300 \pm 14(\text{stat}) \pm 5(\text{syst})$ MeV [62], respectively.

The B_c lifetime was measured through the semileptonic decays $B_c \to J/\psi e^+ \nu_e$ [63] and $B_c \to J/\psi\mu^+ \nu_\mu$ [64] by the two collaborations, respectively. Only recently, the CDF Collaboration published a measurement of the B_c lifetime in the kinematically closed channel $B_c^+ \to J/\psi\pi^+$ [65]. The measured B_c lifetime is $\tau(B_c) = 0.452 \pm 0.048(\text{stat}) \pm 0.027(\text{syst})$ ps.

The advent of the LHC has opened a new era for the experimental investigation of the B_c meson. The LHCb experiment is driving the field, enriching the scenario of the observed decay modes.

Using Run I data, the LHCb Collaboration reported the observation of many new B_c decay channels with a J/ψ in the final state: $B_c^+ \to J/\psi\pi^+\pi^+\pi^-$ [66], $B_c^+ \to J/\psi K^+$ [67], $B_c^+ \to J/\psi 3\pi^+2\pi^-$ [68], $B_c^+ \to J/\psi K^+K^-\pi^+$ [69], $B_c^+ \to J/\psi D_s^+$ and $B_c^+ \to J/\psi D_s^{+*}$ [70]. They also published the observation of the decay $B_c^+ \to \Psi(2S)\pi^+$ [71], and the

first observation of a baryonic B_c^+ decay, namely $B_c^+ \rightarrow p\bar{p}\pi^+$ [72]. For each decay channel, the relative branching fraction is measured, generally resulting in good agreement with the available predictions.

Also, a measurement of the ratio of the branching fractions into hadronic and semileptonic decays $R = B(B_c^+ \rightarrow J/\psi\pi^+)/B(B_c^+ \rightarrow J/\psi\mu^+\nu_\mu)$ has been released [73]. The result, as shown in Fig. 2.10, is in the lower band of theoretical predictions.
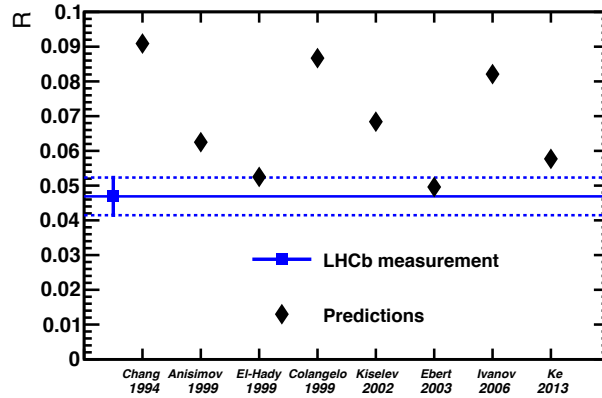

Figure 2.10: LHCb measurement of the ratio of hadronic and semileptonic decay branching fractions of the B$_c$ meson (R) (horizontal solid line) and its $\pm 1\sigma$ uncertainty band (dashed lines) compared to predictions (diamonds). For more details about the theoretical predictions, see Ref.[73].

Finally, the decay $B_c^+ \rightarrow B_s^0\pi^+$ was also observed [74]: this is the first observation of a B$_c$ decay with the b-quark as a spectator.

The subject of this thesis is the measurement of the relative branching fraction of the decays $B_c^+ \rightarrow J/\psi\pi^+\pi^+\pi^-$ and $B_c^+ \rightarrow J/\psi\pi^+$ in the CMS experiment.

The most precise measurement of the B$_c$ mass from LHCb was obtained in the $B_c^+ \rightarrow J/\psi D_s^+$ decay mode, and is

$$6276.28 \pm 1.44 \,(\text{stat}) \pm 0.36 \,(\text{syst}) \; MeV. \tag{2.9}$$

A measurement of the B$_c$ lifetime in the semileptonic decay $B_c^+ \rightarrow J/\psi\mu^+\nu_\mu X$ has been recently provided. The LHCb measurement is [75]:

$$\tau_{B_c} = 509 \pm 8 \,(\text{stat}) \pm 12 \,(\text{syst}) \text{ fs.} \tag{2.10}$$

This result is the most accurate measurement of τ_{B_c} so far and is higher than the previous measurements from the Tevatron experiments.

Finally, production properties of the B_c^+ meson are measured in 7 TeV [76] data in the kinematic region where $p_T(B_c) > 4$ GeV and pseudorapidity is $2.5 < \eta < 4.5$. The ratio $R_{c/u}$ of the production cross-section times branching fraction between the $B_c^+ \rightarrow J/\psi \pi^+$ and the $B^+ \rightarrow J/\psi K^+$ decays is measured to be

$$R_{c/u} = (0.68 \pm 0.10 \ (\text{stat}) \pm 0.03 \ (\text{syst}) \pm 0.05 \ (\text{lifetime}))\%. \qquad (2.11)$$

This thesis provides a measurement of $R_{c/u}$ in the kinematic region $p_T > 15$ GeV and $|y| < 1.6$ performed with the CMS experiment at the LHC.

The ATLAS experiment has recently provided the first observation of an excited B_c state, $B_c(2S)$, using the full statistics of Run I data [77]. The mass of the observed state is found to be $6842 \pm 4 \ (\text{stat}) \pm 5 \ (\text{syst})$ MeV and the significance of the observation is 5.2σ. Fig.2.11 shows the distribution of the mass difference $Q = m(B_c^\pm \pi\pi) - m(B_c^\pm) - 2m(\pi^\pm)$ obtained from the ATLAS experiment in 2011 and 2012 data. The $B_c(2S)$ signal peak is evident above the continuum background.
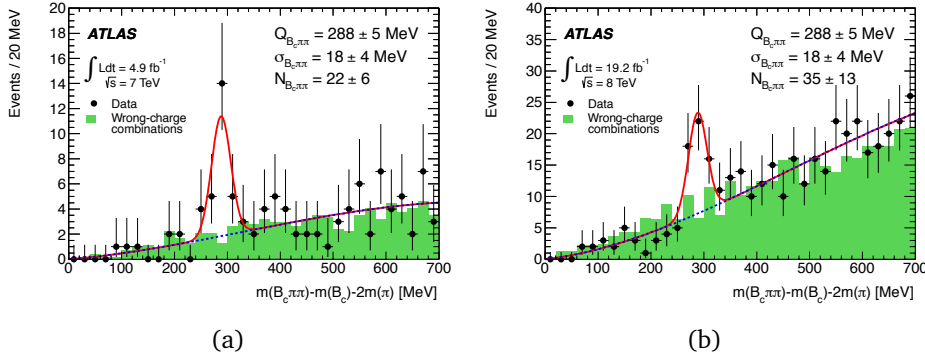

Figure 2.11: Distribution of $Q = m(B_c^\pm \pi\pi) - m(B_c^\pm) - 2m(\pi^\pm)$ from the ATLAS experiment for the opposite-charge pion combination (points with error bars) and for the same (wrong)-charge pion combinations (shaded histogram) in 7 TeV (a) and 8 TeV (b) data [77].

Chapter 3

The CMS experiment at the LHC

The measurements described in this thesis are based on a data sample collected by the CMS detector during the 2011 LHC Run. This Chapter provides a general description of the experimental apparatus, both collider and detector, focusing on the more relevant elements for this analysis: the tracker and muon sub-detectors, the tracking and muon algorithms and the online selection.

3.1   The Large Hadron Collider

The Large Hadron Collider (LHC) [78] is a circular superconducting accelerator and collider, operating at the CERN site in Geneva, Switzerland.

The LHC accelerator is installed in the existing 27 km underground tunnel previously used for the Large Electron Positron collider (LEP) [79]. It is designed to provide proton-proton collisions at a center of mass energy of 14 TeV and instantaneous luminosity of 10^{34} cm^{-2}s^{-1}, thus representing the next major step in the high-energy frontier beyond the Fermilab Tevatron, which has provided proton-antiproton collisions at a center-of-mass energy of 1.96 TeV.

The two proton beams, circulating in opposite directions, collide at four locations, where dedicated experiments are positioned. The two experiments ATLAS [80] and CMS [81] are general-purpose detectors designed to operate at high instantaneous luminosity. The LHCb experiment [82] is designed to operate at lower luminosities and optimized to measure the properties of B-hadrons. The ALICE experiment [83] has been especially built to explore the properties of heavy-ion collisions. Finally, the TOTEM experiment [84] operates at the same interaction point as the CMS experiment and is designed to study the physics of elastic scattering at small angles.

The LHC accelerator chain and locations of the four experiments are shown

in Fig. 3.1. Protons are first accelerated to 50 MeV using the linear accelerator Linac2. They are then injected into the Proton Synchrotron Booster which accelerates them to 1.4 GeV. and sends them to the Proton Synchrotron (PS), which accelerates the beams to 25 GeV. Protons are then fed to the Super Proton Synchrotron (SPS), which increases the energy to 450 GeV and finally transfers the two beams to the LHC.
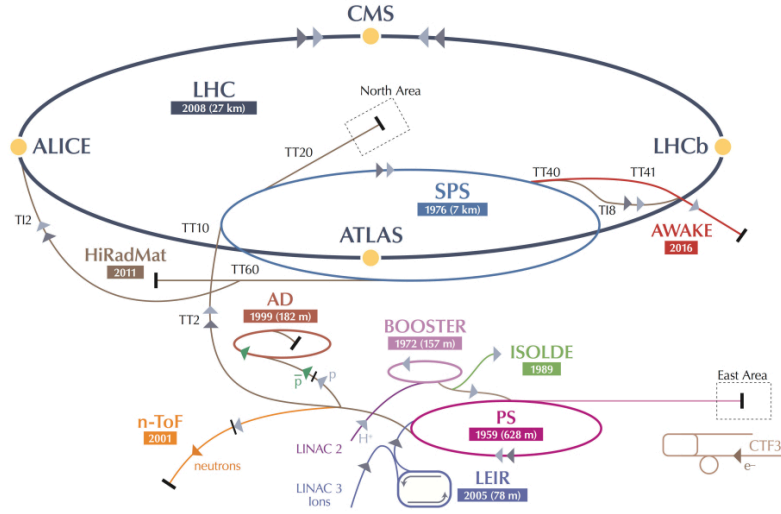

Figure 3.1: The CERN accelerator complex.

The rate of events for any process at the LHC is given by:

$$N = \sigma \mathscr{L}, \tag{3.1}$$

where σ is the cross section of the process and $\mathscr{L}$ is the instantaneous luminosity. The latter depends only on the beam parameters and is defined as

$$\mathscr{L} = \frac{N_b^2 n_p f_{rev} \gamma_r}{4\pi \epsilon_n \beta^*} F. \tag{3.2}$$

The definitions of the beam parameters and their design values for collisions at the highest luminosity are reported in Table 3.1.

The accelerator produced the first proton-proton collisions in November 2009. After few pilot runs, operations started in March 2010 at a reduced center-of-mass energy of 7 TeV, delivering to the ATLAS and CMS experiments

Parameter	Meaning	Value
N_b	Number of protons per bunch	1.15×10^{11}
n_p	Number of proton bunches per beam	2808
f_{rev}	Frequency of revolution	11.245 kHz
γ_r	Relativistic gamma factor	7461
ϵ_n	Normalized transverse beam emittance	3.75 μm
β^*	Beta function at the interaction point	55 cm
F	Geometric luminosity reduction factor	0.836

Table 3.1: LHC beam parameters and their design values for the two general purpose detectors [85].

about 44 pb^{-1} by end of 2010 and 6 fb^{-1} by end of 2011 (Fig.3.2a). During the 2011 data-taking period the instantaneous luminosity of the LHC was raised from low luminosities up to $\mathscr{L} = 3.6 \times 10^{33}$ cm^{-2} s^{-1} (Fig.3.2b), thanks to the increased number of bunches and β^* optimization. Figure 3.3 shows the total integrated luminosity delivered by LHC and recorded by CMS during stable-beams in 2011 data-taking. The overall CMS recording efficiency was higher than 90%.

During the 2012 data-taking, the LHC operated at a centre-of-mass energy of 8 TeV and delivered about 23 fb^{-1} of integrated luminosity to the CMS and ATLAS experiments. In this period the LHC instantaneous luminosity reached 7.7×10^{33} cm^{-2} s^{-1}. Since LHC operated at an increased bunch spacing of 50 ns, with a consequent decrease of the maximum number of bunches per beam to 1374, this luminosity, greater than half the design luminosity, was achieved by operating at larger bunch intensity ($N_b = 1.7 \times 10^{11}$) and lower normalized emittance ($\epsilon_n = 2.5$ μm) than the original design.

The high LHC luminosity allows to reach sensitivity to rare processes, but, on the other hand, the event rate is so high that several interactions overlap in the same bunch crossing. The *pileup* of multiple interactions of the same bunch crossing and the overlap in the detector of signals from different bunch crossings, due to the limited speed of detector response and read-out (out-of-time pileup), pose significant challenges to the trigger, event reconstruction and analysis.
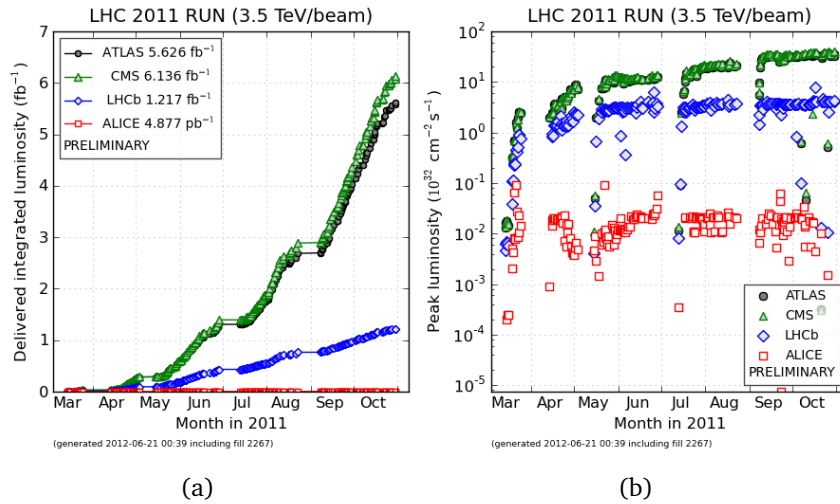
Figure 3.2: Cumulative *pp* luminosity delivered by the LHC to the different experiments during 2011 Run (a) and peak instantaneous luminosity (b).
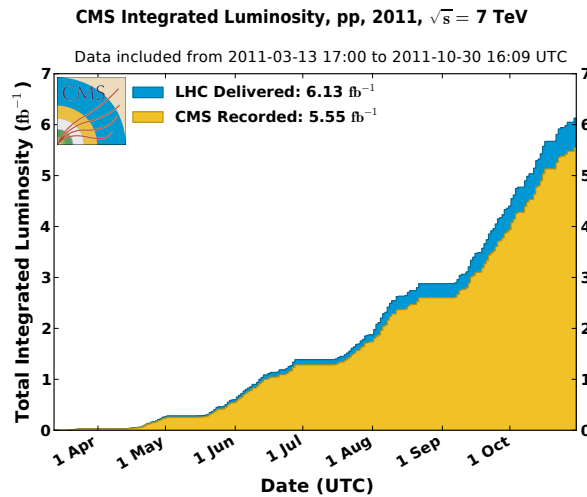

Figure 3.3: Total integrated luminosity delivered to (blue) and recorded by CMS (yellow) during stable-beams in 2011.

3.2   The CMS experiment

The Compact Muon Solenoid (CMS) experiment [81] is a general-purpose detector situated at the LHC Point 5 near the village of Cessy, France. The detector has a cylindrical geometry, with a length of 21.6 m, a diameter of 14.6 m and a total weight of 12500 tons. The CMS detector consists in several concentric subdetectors: the silicon tracker, the electromagnetic calorimeter, the hadron calorimeter, and the muon system. The detector is sketched in Fig. 3.4.
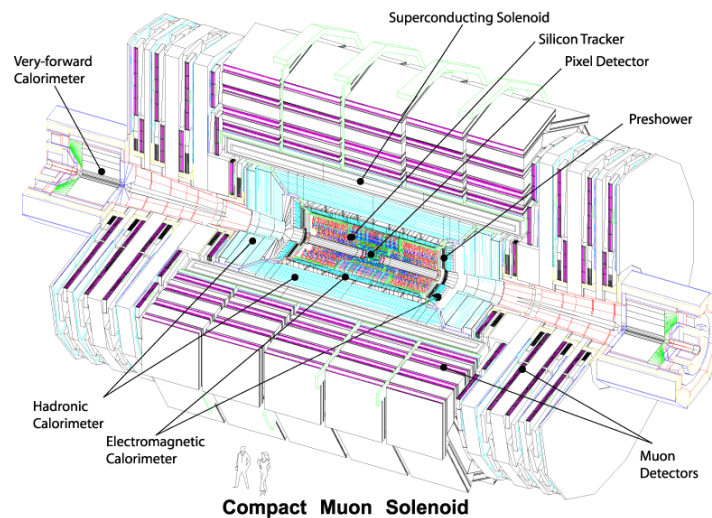

Figure 3.4: Schematic view of the CMS detector.

The core of the CMS apparatus is a 13 m long superconducting solenoid with 5.9 m inner diameter, providing a uniform magnetic field of 3.8 T (see Fig.3.5). It generates a large bending power which allows to precisely measure the transverse momentum of charged particles. The CMS magnet solenoid operates at a temperature of 4 K, ensured by a sophisticated helium cooling system. The return field is large enough to saturate 1.5 m of iron, where muon stations are integrated, while the inner tracker and the calorimetry are accommodated inside the bore of the magnet coil.

The detector is subdivided into a cylindrical barrel part and endcap disks on each side of the interaction point. Forward calorimeters complement the coverage provided by the barrel and endcap detectors.
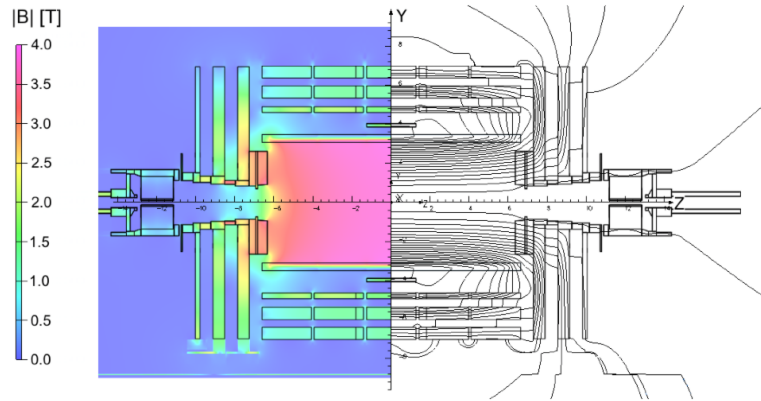
Figure 3.5: Map of the $|B|$ field (left) and field lines (right) predicted for a longitudinal section of the CMS detector by a magnetic field model at a central magnetic flux density of 3.8 T [86]. Each field line represents a magnetic flux increment of 6 Wb.

CMS uses a cylindrical coordinate system (r, ϕ, η) with the z-axis along the beam line, r being the distance from the z-axis, ϕ the azimuthal coordinate with respect to the x-axis, which points towards the center of LHC, and η the pseudorapidity defined as $\eta = -\ln \tan \theta/2$, with θ being the polar angle.

In the following a brief description of the main features of the CMS detector is reported, a more detailed description can be found elsewhere [81].

3.3   The tracker

The inner tracking system of CMS is designed to provide a precise and efficient measurement of the trajectories of charged particles emerging from the LHC collisions, as well as a precise reconstruction of the decay positions of particles with long lifetimes such as bottom quarks and taus.

The CMS Tracker [87] consists of two main detectors: a silicon pixel detector, located close to the beam pipe and covering the region from 4 to 15 cm in radius, and 49 cm on either side of the collision point along the LHC beam axis, and a silicon strip detector, covering the outer region from 25 to 110 cm in radius, and within 280 cm on either side of the collision point along the beam axis.

The pixel detector, which is designed to provide the determination of three high precision three-dimensional points on track trajectories, has 66 million active elements covering a total area of ≈ 1 m^2 . The silicon strip detector has

9.3 million active elements instrumenting a surface area of 198 m^2. The layout of the CMS tracker is shown in Figure 3.6.
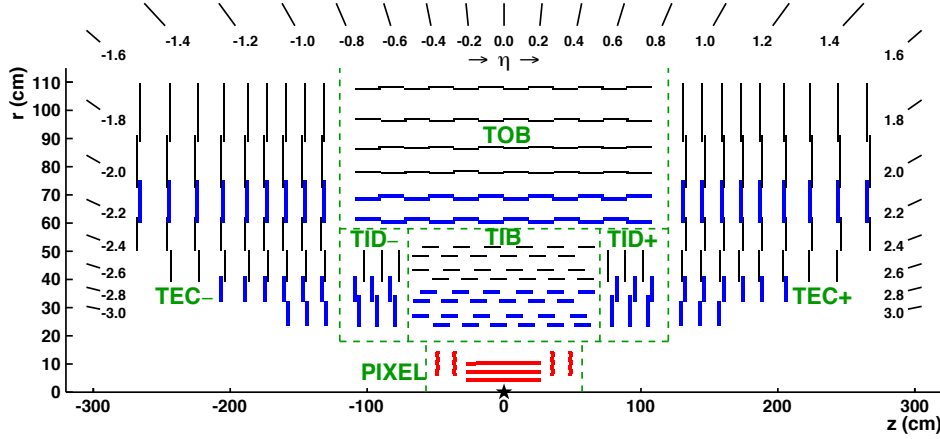

Figure 3.6: Schematic r-z view of the CMS tracker.

3.3.1 Pixel detector

The pixel detector is situated close to the interaction point. It consists of three concentric cylindrical barrel layers with two endcap disks on each side of them (see Fig.3.7). The barrel layers are located at average radii of 4.3 cm, 7.3 cm and 10.2 cm, and have an active length of 53 cm. The two end disks, extending from 4.8 to 14.4 cm in radius, are placed on each side at $|z| = 35.5$ cm and 48.5 cm. The system provides efficient three-hit coverage in the region of pseudorapidity $|\eta| < 2.2$ and efficient two-hit coverage in the region $|\eta| < 2.5$.

In order to achieve the optimal vertex position resolution, a design with an almost square pixel shape of $100 \times 150 \ \mu m^2$ in both the (r, ϕ) and the z coordinates has been adopted.

The barrel comprises 768 pixel modules which are oriented with the smaller pitch in the azimuthal direction. The large Lorentz drift of the collected electrons due to the 3.8 T magnetic field enhances the azimuthal charge sharing improving the $r - \phi$ resolution.

The endcap disks, that comprise 672 pixel modules, with 7 different modules in each blade, are assembled in a turbine-like geometry with blades rotated by 20° to benefit from the Lorentz effect.
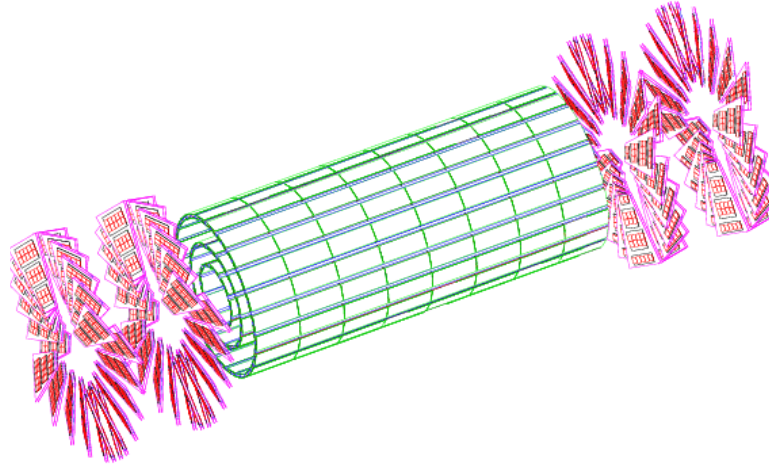
Figure 3.7: Layout of the CMS pixel detector.

3.3.2 Strip tracker

The strip tracker surrounds the pixel detector. It is composed of almost 15400 modules each of which carries either one thin (320 μm) or two thick (500 μm) single sided p-on-n type silicon micro-strip sensors. The thin sensors are used closest to the beam pipe to minimize the amount of material there. The tracker has four subsystems: the Tracker Inner Barrel (TIB), Inner Disks (TID), Outer Barrel (TOB) and End Caps (TEC).

The TIB and TID extend in radius to 55 cm and consist of four cylindrical barrel layers, supplemented by three disks at each end. The TIB/TID delivers up to four $r-\phi$ measurements on a trajectory using 320 μm thick silicon microstrip sensors, which have their strips oriented parallel to the beam axis in the barrel and oriented radially in the disks. The two inner TIB layers support modules with a strip pitch of 80 μm, whereas the outer two host modules with a strip pitch of 120 μm. In the TID, the mean pitch varies between 100 and 141 μm.

The TOB surrounds the TIB and the TID. It consists of six cylindrical layers that are centered on the z-axis and extend 1.18 m from the interaction point in both directions along the z-axis. The TOB uses 500 μm sensors with strip pitches of 183 μ in the first four layers and 122 μm in the last pair of layers.

The TEC encloses the rest of the tracker. It consists of nine disks on each side of the TOB that extend into the region 124 cm $< |z| <$ 280 cm. The sensors in the four inner rings are of the thinner, 320 μm variety, while the ones in the three outer rings are 500 μm thick; the average radial strip pitch varies from

97 to 184 μm.

The inner two layers of the TIB and TOB, the inner two rings of the TID and TEC, and the fifth ring of the TEC include a second microstrip detector module that is mounted back-to-back at a stereo angle of 100 mrad and enables a measurement of the orthogonal coordinate. Assuming fully efficient planes and not counting hits in stereo modules, there are from 8 to 14 high precision measurements of track impact points for $|\eta| < 2.4$.

3.4 Electromagnetic calorimeter

The Electromagnetic Calorimeter (ECAL) [88] is a homogeneous and hermetic calorimeter comprising 61200 lead tungstate (PbWO$_4$) scintillating crystals mounted in the barrel (EB), closed at each end by endcaps (EE) each containing 7324 crystals. In order to enhance photon identification capabilities, a preshower detector (ES) based on lead absorbers equipped with silicon strip sensors is placed in front of the endcap crystals. The ECAL layout is depicted in Fig. 3.8.
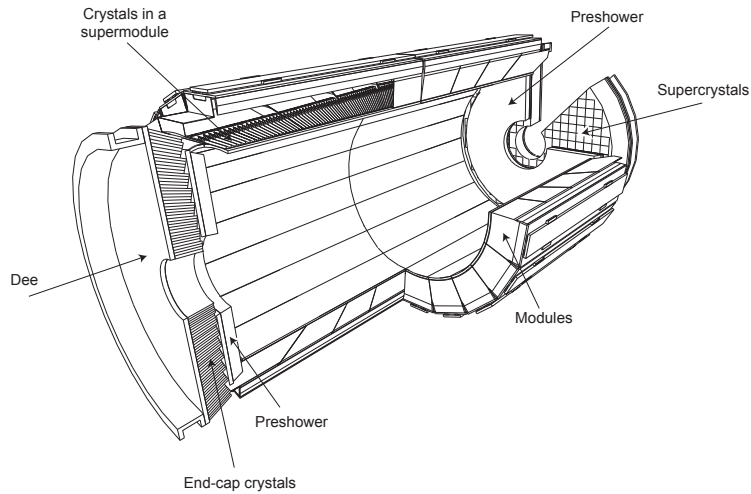

Figure 3.8: ECAL layout, showing the barrel supermodules, the two endcaps and the preshower detectors.

The high-density (8.28g/cm^3), short radiation length ($X_0 = 0.89$ cm), and small Moliere radius ($R_M = 2.2$ cm) of PbWO$_4$ allowed the construction of a compact calorimeter inside the solenoid with fine granularity. The relatively low light yield (30γ/MeV) requires use of photodetectors with intrinsic gain

that can operate in a magnetic field. Silicon avalanche photodiodes are used as photodetectors in the barrel and vacuum phototriodes in the endcaps.

The barrel section has an inner radius of 129 cm and is structured as 36 "supermodules", each covering half the barrel length, and provide 360-fold granularity in ϕ and 85-fold granularity in each η direction up to $|\eta| = 1.479$. Each supermodule is composed of four modules, formed by submodules with five pairs of crystals. The EB crystals have a truncated pyramidal shape and are mounted in a quasi-projective geometry (the axes are tilted at 3° with respect to the line from the nominal vertex position), to minimize inter-crystal gaps aligned to particle trajectories. They are 23 cm long and have a front face cross sections of around 2.2 cm×2.2 cm.

The endcaps are located at a distance of 314 cm from the vertex and extend the coverage to $1.479 < |\eta| < 3.0$. The 22 cm long crystals, with front face cross sections of 2.86 cm×2.86 cm, are arranged in an $x - y$ grid to form an approximately circular shape.

The ES contains two active planes of silicon strip sensors and associated mechanics, cooling and front-end electronics. It covers the region $1.65 < |\eta| < 2.6$. The sensors have an active area of 61 mm×61 mm, divided into 32 strips. The planes closer to the interaction point have their strips aligned vertically while the farther plane strips are horizontal, to provide accurate position measurement and fine granularity in both coordinates.

3.5 Hadron calorimeter

The primary purpose of the Hadron Calorimeter (HCAL) [89] is the measurement of hadronic energy from collisions in CMS. In addition to the energy measurement, the HCAL is also able to perform a precise time measurement for each energy deposit, valuable for excluding calorimeter noise and energy deposits from beam halo and cosmic ray muon.

The HCAL consists of a set of sampling calorimeters (Fig.3.9). The barrel and endcap calorimeters (HB and HE) are composed by alternated layers of brass as absorber and plastic scintillator as active material. The scintillation light is converted by wavelength-shifting fibers embedded in the scintillator and channeled to hybrid photodiode detectors via clear fibers. The HB part consists of 32 towers covering the pseudorapidity region $|\eta| < 1.4$, resulting in 2304 towers with a segmentation $\Delta\eta \times \Delta\phi = 0.087 \times 0.087$. Each hadron endcap is made by 2304 towers covering the pseudorapidity region $1.3 < |\eta| < 3.0$.

The outer calorimeter (HO) utilizes the CMS magnet coil/cryostat and the steel of the magnet return yoke as its absorber, and uses the same active material

and read-out system as HB and HE. It is divided into 5 sections along η, each of which covers 2.5 m in z.

The forward calorimeter (HF) is based on Cherenkov light production in quartz fibers and covers the region $3.0 < |\eta| < 5.0$. The front face is located at 11.2 m from the interaction point and the absorber depth is 1.65 m.
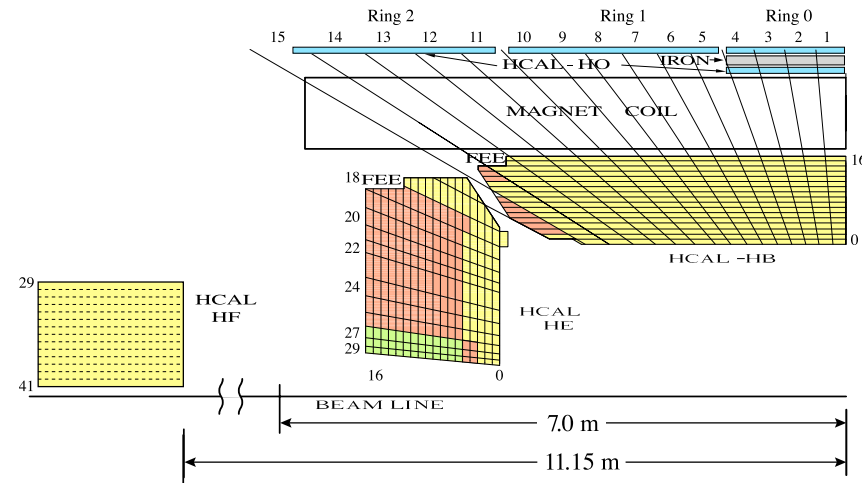

Figure 3.9: HCAL layout, showing the four sub-detectors and the locations of the Front End Electronics (FEE) for HB and HE.

3.6   The Muon system

Muon detection and reconstruction is a powerful tool for the discovery of new physics and for precision measurements of standard model processes. These require the robust detection of muons over the full acceptance of the CMS detector and over the very high background rate at the LHC.

The CMS muon system [90] has three primary functions: muon triggering, identification, and momentum measurement. Excellent muon momentum resolution and trigger capability are enabled by the high-field solenoidal magnet and its flux-return yoke, which also serves as a hadron absorber to facilitate the identification of muons.

The CMS detector uses 3 types of gas-ionization particle detectors arranged in a cylindrical barrel section and 2 planar endcap regions (Fig.3.10). The choice of the detector technologies has been driven by the very large surface to

be covered and by the different radiation environments. Drift tube (DT) chambers and cathode strip chambers (CSC) detect muons in the regions $|\eta| < 1.2$ and $0.9 < |\eta| < 2.4$, respectively and are complemented by a system of resistive plate chambers (RPC) covering the range $|\eta| < 1.6$.
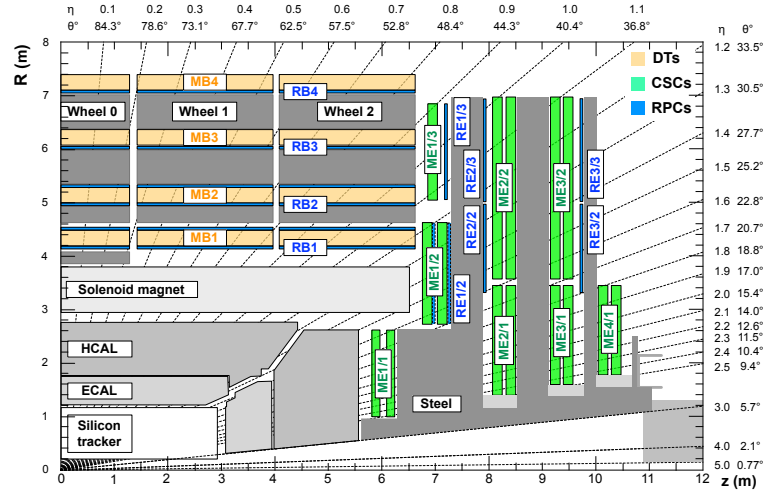

Figure 3.10: An r-z cross section of a quadrant of the CMS detector. The locations of the various muon stations and the steel disks (dark grey areas) are shown. The 4 DT (light orange) stations are labeled MB (muon barrel) and the CSC (green) are labeled ME (muon endcap). RPC (blue) are in both the barrel and the endcaps, where they are labeled RB and RE, respectively.

The barrel muon detector consists of 4 stations forming concentric cylinders around the beam line. The 3 inner cylinders have 60 DT chambers each and the outer cylinder has 70. The smallest unit of the DT detector is a drift cell 42 × 13mm in area by 2-3 m in depth; four rows of drift cells staggered by half a cell form a superlayer. The final geometrical arrangement is 2 superlayers along the beam and one perpendicular to it, spaced by a honeycomb structure to provide support and higher angular coverage. Each station is designed to give a muon vector in space, with a ϕ precision better than 100 μm in position and approximately 1 mrad in direction.

The Endcap Muon system consists of 468 CSC arranged in groups. A CSC unit is made of 6 sets of multiwire gas chambers planes with cathode strips glued to the walls, aligned along the radial direction and perpendicular to the wires. The innermost CSC detector lies inside the solenoid, so the wires have to be rotated at a Lorentz angle of 29° to compensate for the Lorentz drift. A

muon in the range $1.2 < |\eta| < 2.4$ crosses 3 or 4 CSCs. The spatial resolution provided by each chamber is typically about 200 μm and the angular resolution in ϕ is of order 10 mrad.

In addition to these tracking detectors, the CMS muon system includes a complementary, dedicated triggering detector system with excellent time resolution ($\sim$ 1 ns). The RPCs are double-gap chambers operated in avalanche mode to ensure reliable operation at high rates. They are located both in the barrel and the endcaps: in the barrel there are 4 stations, while in the endcap there are 3.

3.7   Track and vertex reconstruction

The trajectory of a charged particle in the quasi-uniform magnetic field of the tracker is a helix, and therefore it is described by five parameters.

Track reconstruction algorithms rely on a good estimate of the proton-proton interaction region, referred to as the *beamspot*. After the beamspot reconstruction (see Sec. 3.7.2), track reconstruction starts using the pixel hits. CMS standard track reconstruction uses an adaptation of the combinatorial Kalman filter [91, 92] named Combinatorial Track Finder (CTF). Multiple iterations of the CTF track reconstruction sequence (*iterative tracking*) are performed: the idea is to first search for those tracks that are easiest to find (large p_T, produced near the beamspot), remove the hits associated with these tracks and perform the following step in a cleaner environment, looking for more difficult classes of tracks. The final set of tracks is merged to form the collection of reconstructed tracks.

Each iteration proceeds in four steps:

SEED GENERATION The seeds define the initial estimate of the trajectory parameters and their corresponding uncertainty. Seeds are constructed in the inner part of the tracker and track candidates are built outwards. Seed generation requires information on the beamspot and primary vertices position, which is produced before starting the track reconstruction by a very fast algorithm using only hits from the pixel detector. Track seeds are then searched for: they can be be either a triplet of hits, or two hits plus a vertex constraint and must be found within a tracking region defined by limits on the acceptable track parameters, including minimum p_T, and maximum transverse and longitudinal distances of closest approach to the assumed production point of the particle.

TRACK FINDING This step is an iterative algorithm based on the Kalman filter

method. Starting from a coarse estimate of the track parameters provided by the trajectory seed, track candidates are built by adding hits from successive detector layers and updating the track parameters at each step. All track candidates found at each layer are propagated to the next compatible layers. The compatibility criterion is given by the charged particle equation of motion, corrected by energy losses and multiple scattering. For each compatible hit in the new layer, a new trajectory candidate is built and the procedure is repeated until a termination condition is satisfied. Since the track of a single charged particle can be reconstructed more than once (starting from different seeds or when a given seed develops into more candidates), a trajectory cleaner is applied after all the track candidates in a given iteration have been found.

TRACK FITTING The trajectory is refitted using a Kalman filter starting from the innermost hit and proceeding outwards. After a smoothing stage, a second filter, initialized with the results of the first one, is run backwards towards the beam line. The optimal track parameters are then obtained from the weighted average of these two filters. After filtering and smoothing, spurious hits, incorrectly associated to the track, are searched and removed, and the track is again filtered and smoothed.

TRACK SELECTION Quality requirements are applied to the reconstructed track candidates in order to discard fake tracks (tracks not associated to any charged particle). The selection is based on different variables, such as number of layers that have hits, fit $\chi^2/ndof$ and distance from the primary interaction vertex. Track selection criteria have different values for each iteration and are defined as *loose*, *tight* and *high purity*, providing progressively more stringent requirements, which reduce the fake rate but also the efficiency.

Results for tracking efficiency are shown in Fig.3.11. The efficiency is measured on simulated particles generated within $|\eta| < 2.5$, with a production point < 3 cm and < 30 cm from the centre of the beamspot for r and $|z|$, respectively.

3.7.1 Primary vertex reconstruction

The goal of primary-vertex reconstruction is to measure the position and the associated uncertainty of all pp interaction vertices in each event (both "signal" and vertices from pileup collisions). This is performed in three steps: track selection, track clustering and vertex fitting.
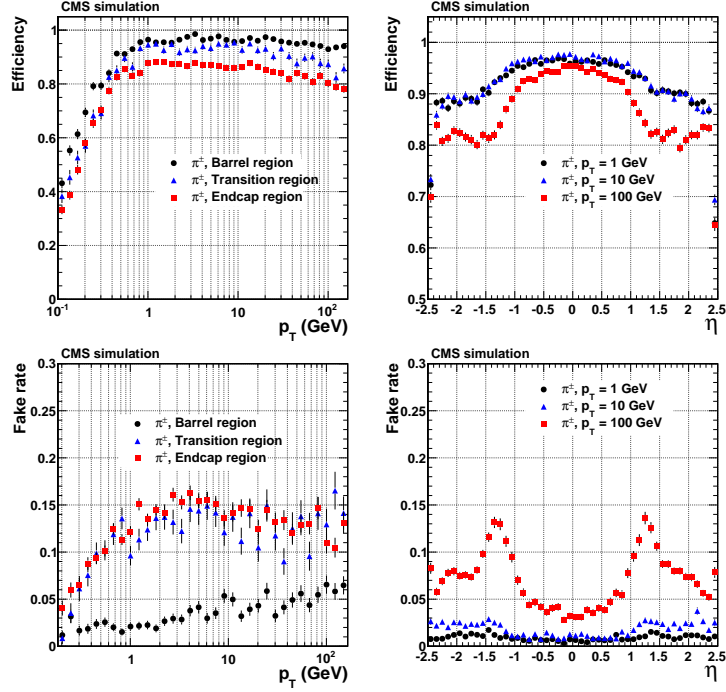
Figure 3.11: Top row: track reconstruction efficiencies for pions passing the high-purity quality requirements. Results are shown as a function of η (left), for $p_T = 1$, 10, and 100 GeV and as a function of p_T (center), for the barrel, transition, and endcap regions, which are defined by the η intervals of 0-0.9, 0.9-1.4 and 1.4-2.5, respectively. Bottom row: fake rate for single, isolated pions passing the high purity cuts, as a function of p_T and η [93].

The first step consists in choosing tracks consistent with being produced in the primary interaction region. This is accomplished by imposing requirements on the transverse impact parameter significance, number of hits in the pixel and strip detectors, and quality of the track fit.

The selected tracks are then grouped into clusters on the basis of their z-coordinates at their point of closest approach to the centre of the beam spot. The clustering is performed using a *deterministic annealing* (DA) algorithm, described in Ref. [94].

Candidates vertices identified via the DA clustering are finally fitted to find the best estimation of the vertex parameters. The fit is performed using an *adaptive vertex fitter* [95], which assign each track a weight based on the compatibility of the track with the vertex.

The efficiency of reconstructing a primary vertex and the resolution of the reconstructed primary-vertex position depends strongly on the number of tracks used to fit the vertex and their p_T, as shown in Fig. 3.12. The resolution in x and z for primary vertices reconstructed using at least 50 tracks are less than 20 and 25 μm, respectively, for minimum-bias events. It significantly improves (up to 10 and 12 μm) for jet-enriched events, where the average track p_T is higher.
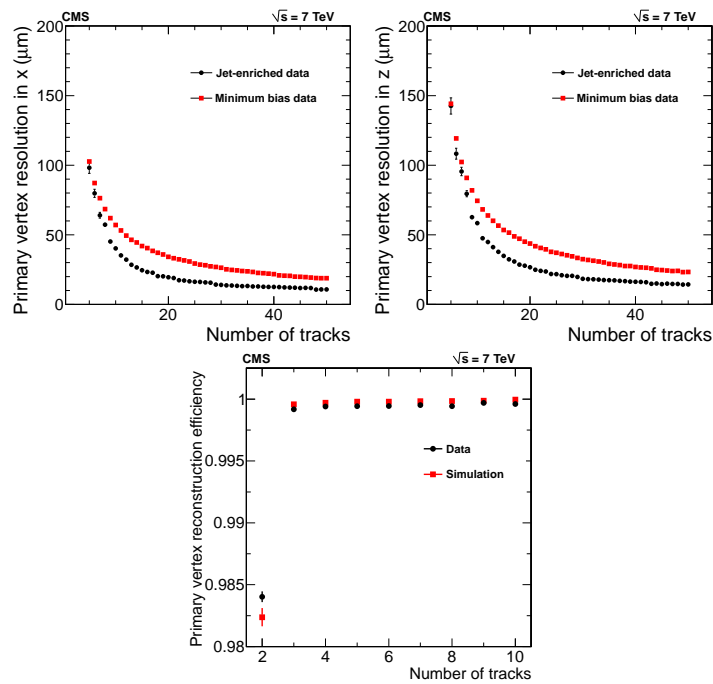

Figure 3.12: Plots in the first row show the x and z resolution as a function of the number of tracks at the fitted vertex, for two kinds of events with different average track p_T values [93]. The tracks in jet-enriched events have significantly higher mean p_T than minimum bias data, resulting in a better vertex resolution.
On the second row: primary-vertex reconstruction efficiency as a function of the number of tracks in a cluster, measured in minimum-bias data and in MC simulation.

3.7.2   Beamspot reconstruction

The beamspot is defined as a 3D profile of the luminous region where the LHC beams collide in the CMS detector. In contrast to the primary vertex reconstruction, that is performed for each collision, the beamspot parameters are

measured from an average over many events (precisely, it is determined every luminosity section, corresponding to a period of 23 seconds).

The position of the centre of the beamspot is determined through the combination of two methods: the first, used to measure the z coordinate and the RMS widths of the luminous region, consists in a fit to the 3D distribution of primary vertex positions; the second [96], used to determine the transverse coordinates, only needs track information and exploits the correlation between d_0 and ϕ that appears when the beamspot is displaced relative to its expected position.

The beamspot position is used to estimate the position of the interaction point prior to the reconstruction of the primary vertex and to provide an additional constraint in the reconstruction of all the event primary vertices.

3.7.3   Secondary vertex reconstruction

In this thesis, the secondary vertex reconstruction is performed using a kinematic fitting [97], which allows to apply user-defined constraints on the track and vertex parameters. This can be useful to improve the experimental resolution of the measurements.

The mathematical approach of the kinematic fitting is based on Least Mean Square minimization with Lagrange multipliers, which allows to formulate the problem in a form that has a unique solution. The fitting algorithm comprises multiple iterations, which take each time the result of the previous step as the starting point and are repeated until a maximum number of iterations or the residuals of the constraint equations are below a certain value.

The application of constraints in the fit procedure allows to improve the resolution on both the reconstructed mass (more than 50% improvement) and vertex transverse and longitudinal coordinates.

3.8   Muon reconstruction and identification

In the standard CMS reconstruction for pp collisions, muon tracks are first reconstructed independently in the inner tracker (tracker track) and in the muon system (standalone-muon track). Based on these objects, two reconstruction approaches are used:

GLOBAL MUON RECONSTRUCTION (OUTSIDE-IN) For each standalone-muon track, a matching tracker track is found by comparing parameters of the two tracks propagated onto a common surface. A global-muon track is fit combining hits from the tracker track and standalone-muon track, using

the Kalman-filter technique. At large transverse momenta, $p_T > 200\,\mathrm{GeV}$, the global-muon fit can improve the momentum resolution compared to the tracker-only fit.

TRACKER MUON RECONSTRUCTION (INSIDE-OUT) In this approach, all tracker tracks with $p_T > 0.5$ GeV and total momentum $p > 2.5$ GeV are considered as possible muon candidates and are extrapolated to the muon system taking into account the magnetic field, the average expected energy losses, and multiple Coulomb scattering in the detector material. If at least one muon segment (i.e., a short track stub made of DT or CSC hits) matches the extrapolated track, the corresponding tracker track qualifies as a Tracker Muon. Minimal requirements for performing track-to-segment matching are described in [98].

Tracker Muon reconstruction is more efficient than the Global Muon reconstruction at low momenta, $p < 5$ GeV, because it requires only a single muon segment in the muon system, whereas Global Muon reconstruction is designed to have high efficiency for muons penetrating through more than one muon station and typically requires segments in at least two muon stations. Owing to the high efficiency of the tracker-track reconstruction and the very high efficiency of reconstructing segments in the muon system, about 99% of muons produced in pp collisions within the geometrical acceptance of the muon system and having sufficiently high momentum are reconstructed either as a Global Muon or a Tracker Muon, and very often as both. Candidates found both by the Global and the Tracker Muon approaches sharing the same tracker track are merged into a single candidate. Muons reconstructed only as standalone-muon tracks have worse momentum resolution and higher admixture of cosmic-ray muons than the Global and Tracker Muons.

These basic reconstructions can be further refined for specific purposes: physics analyses can indeed accommodate the desired balance between identification efficiency and purity by applying a selection based on various muon identification variables.

A set of requisites suited to B-physics analyses has been studied and optimized (*Soft Muon* selection) for low p_T muons ($p_T < 10$ GeV).

This selection requires the candidate to be a Tracker Muon, with the additional request that a muon segment is matched in both x and y coordinates with the extrapolated tracker track. Segments that form a better match with a different tracker track are not considered.

The combined muon reconstruction and identification efficiency of the Soft Muon selection has been measured for prompt produced muons in Ref. [99]

using a "tag and probe" technique. The results are shown in Fig. 3.13 for data collected in 2010 and simulation; $J/\psi \to \mu^+\mu^-$ events are used to measure the efficiency for $p_T < 20$ GeV, while $Z \to \mu^+\mu^-$ decays are used for $p_T > 20$ GeV. The plateau of the efficiency is reached at $p_T \approx 4$GeV in the endcaps and $\approx$ 6 GeV in the barrel. The efficiency measured from $J/\psi \to \mu^+\mu^-$ ($Z \to \mu^+\mu^-$) data events is $\sim 98.4\%$ (99.2%) in the barrel and 98.0% (99.9%) in the endcap.
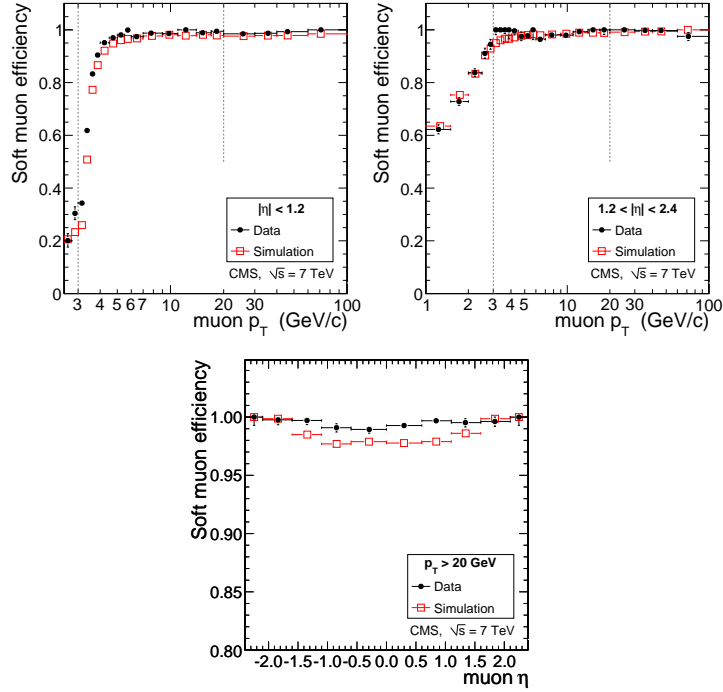

Figure 3.13: Tag-and-probe results [99] for combined muon reconstruction and identification efficiency in data compared to simulation. Given that a tracker track exists, the plots show the efficiency as a function of muon p_T in the barrel and overlap regions and in the endcaps (first row). The measurement is made using $J/\psi \to \mu^+\mu^-$ events for $p_T < 20$ GeV and $Z \to \mu^+\mu^-$ events for $p_T > 20$ GeV. The plot on the second row shows the efficiency as a function of muon pseudorapidity as measured from $Z \to \mu^+\mu^-$ events.

Further identification variables have been studied to suppress muons from decay in flight and guarantee a good p_T measurement. In particular, requirements on the number of hits in the tracker (>10), of which at least 2 in the pixel detector, and cuts on the transverse (longitudinal) impact parameter with respect to the primary vertex, $d_{xy} < 3$ cm ($d_z < 30$ cm) have been adopted.

Finally, the $\chi^2/ndof$ of the tracker-track fit is a good discriminant to suppress muons from decays in flight, and is required to be less than 1.8.

3.9   Trigger

At design luminosity, the LHC will collide proton bunches every 25 ns, with each collision resulting in an average of 20 proton-proton interactions. The total amount of data from these interactions is several orders of magnitude larger than what can be written to permanent storage. As a consequence, the selection of the interesting interactions must be performed online.

The CMS trigger system [100] is designed in two steps: the Level 1 (L1) trigger, which is built on custom electronics, and the High Level Trigger (HLT), which relies on commercial processors.

The L1 trigger performs a fast, coarse-grained analysis of the detector information and reduces the bunch crossing rate to around 100 kHz. The HLT then performs a slower, but more precise analysis and further reduces the rate to about 300 Hz.

3.9.1   L1 Trigger

The L1 trigger hardware is located partly on the detector and partly in the underground control room 90 m away. It stores the data from multiple bunch crossings in pipelines and takes at most 3.2 μs to decide whether the data from a particular bunch crossing should be sent to the HLT. It uses information from the calorimeters and the muon system, which provide trigger primitives in the form of local energy deposits and track segments or hits, respectively.

The L1 trigger system is organized into three subsystems: the calorimeter, the muon and the global L1 trigger.

The muon trigger is further divided in subsystems representing the three muon detectors, the DT trigger in the barrel, the CSC trigger in the endcap and the RPC trigger in both barrel and endcap. The Global Muon Trigger (GMT) combines information for DT, CSC and RPC by converting muon tracks into the same coordinates and correlating CSC and DT tracks with RPC tracks. It also connects muon tracks with an $\eta - \phi$ grid of quiet calorimeter to determine if these muons are isolated. Finally, muons are sorted based on their quality, correlation and p_T and the first four muons are sent to the L1 global trigger.

The calorimeter trigger is based on trigger towers each of which takes input from a grid of ECAL crystals and HCAL channels. A trigger primitive is generated for each trigger tower in the ECAL and HCAL, up to $|\eta| = 3.0$. HF provides

trigger primitives from the forward region, covering the range $3.0 < |\eta| < 5.0$, which are used for jet and energy sum triggers only. The pattern of energy deposited in the towers is used by the Regional Calorimeter Trigger to identify electron, photon and jet candidates, and the tower energies are summed to obtain the candidate transverse energy (E_T). Candidate electrons, photons, taus and jets are sent to the Global Calorimeter Trigger (GCT), which sorts them and forwards the top four of each type to the Global Trigger.

Information from GMT and GCT is finally collected and combined by the Global Trigger, which makes the final L1 trigger decision. A diagram of the L1 trigger system is shown in Fig. 3.14.
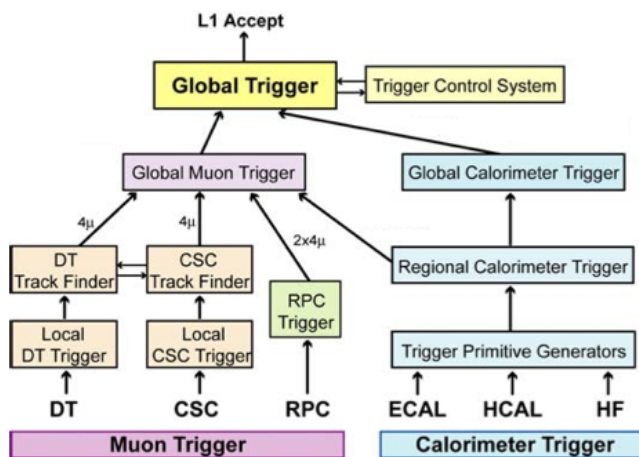

Figure 3.14: Architecture of the L1 trigger.

3.9.2 High Level Trigger

The HLT code performs the reconstruction and selection of physics objects using the full event data with fine granularity and matching information from different subdetectors. However, in order to meet the timing requirements for the online selection, the event reconstruction performed by the HLT is faster and less accurate than the offline one.

The HLT reconstruction starts from those candidates identified by the L1 trigger and is arranged in a chain of virtual trigger levels: the Level 2 uses calorimeter and muon detector information, the Level 2.5 additionally uses the tracker pixel information, and the Level 3 accesses the full event information.

The HLT decision is based on many independent algorithms called *paths*. Each trigger path is a sequence of software modules which do reconstruction and require the presence of one or more physics object passing specific kinematic thresholds.

A "prescale" factor can be applied to trigger paths with very low thresholds, in order to collect data samples for measuring and monitoring the efficiency of higher threshold paths.

In the 2011 Run, there were more than 100 different paths with different thresholds for various physics objects. As the instantaneous luminosity increased, both L1 and HLT selections evolved in order to keep the rate within the allowed bandwidth.

The analysis presented in this thesis relies on dimuon paths, exploiting the presence of a J/ψ meson decaying into two muons in the final state.

The muon reconstruction at HLT proceeds in two steps. The first is the Level 2 (L2) muon reconstruction, which build tracks in the muon chambers starting from L1 candidates and building the trajectory from inside out. The second step is the Level 3 (L3) reconstruction, which consists in extending the muon trajectories to include the full tracker information starting from the L2 track. After each step, filters on the track quality, η and p_T of the muon are applied in order to reduce the rate. Eventually, isolation criteria are also requested using calorimeter and tracker information. Fig. 3.15 is a schematic view of muon reconstruction.

As mentioned before, most of B-physics analyses rely on dimuon triggers. Many dimuon trigger paths have been implemented in the 2011 data-taking, each one covering a specific dimuon mass range and with specific requirements on the dimuon p_T, dimuon vertex probability and, eventually, displacement of the dimuon vertex with respect to the beamspot. Fig. 3.16 shows the dimuon mass distribution collected with the various dimuon triggers during the first 1.1 fb^{-1} of 2011 data.
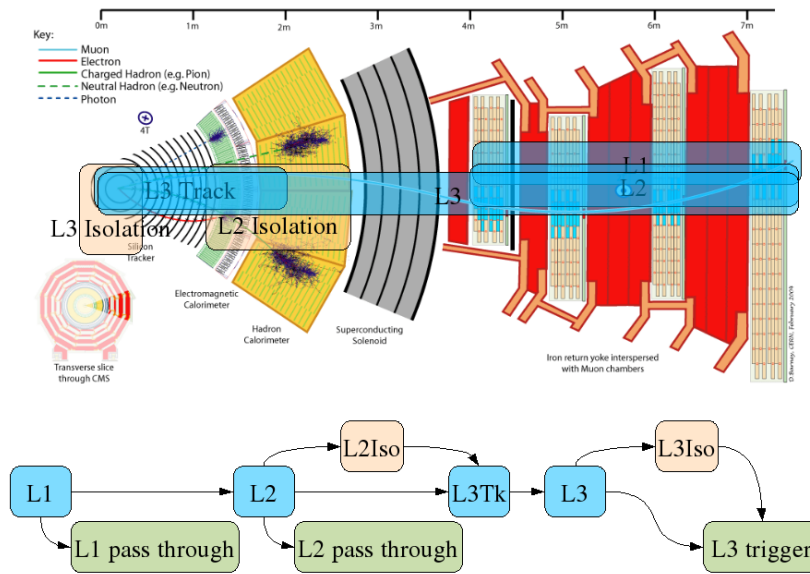
Figure 3.15: Schematic view of muon reconstruction at trigger level.
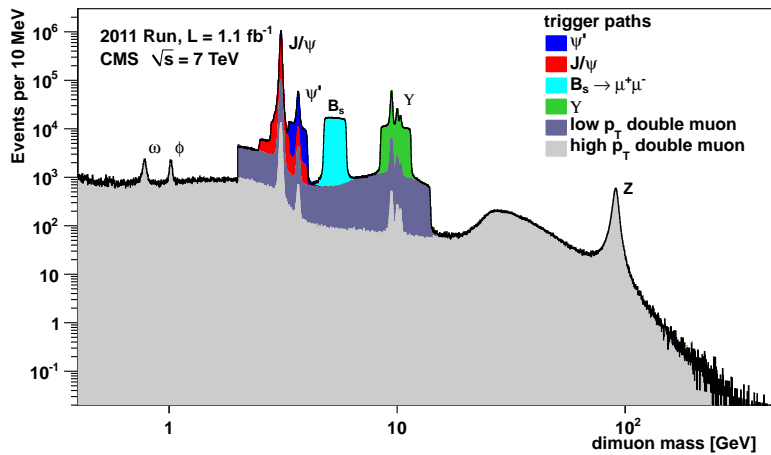
Figure 3.16: Dimuon mass distribution collected with various dimuon triggers during the first period of 2011 Run. The coloured paths correspond to dimuon triggers with low p_T thresholds but narrow mass windows; the light gray distribution represents events collected with a high p_T dimuon trigger, which allows to enlarge the dimuon mass window to the whole spectrum. The dark gray band is a low p_T dimuon trigger available in the first 220 pb^{-1} only.

Chapter 4

Measurement of R_{B_c} and $R_{c/u}$

In this Chapter I describe the analysis performed for the measurement of the ratios

$$R_{B_c} \equiv \frac{B(B_c^+ \to J/\psi \pi^+ \pi^- \pi^+)}{B(B_c^+ \to J/\psi \pi^+)}$$

and

$$R_{c/u} \equiv \frac{\sigma(B_c^+) \times B(B_c^+ \to J/\psi \pi^+)}{\sigma(B^+) \times B(B^+ \to J/\psi K^+)} \; .$$

The analysis general criteria are outlined in the first sections of the Chapter. The event selection and signal extraction are then described in details. The measurements of $R_{c/u}$ and R_{B_c} and the evaluation of their systematic uncertainties are reported in the following sections. Finally, some comments and comparison with results from other experiments are exposed.

4.1 Overview

This analysis exploits the two B_c hadronic decay channels $B_c^+ \to J/\psi \pi^+$ and $B_c^+ \to J/\psi \pi^+ \pi^+ \pi^-$ (charge conjugation is implied throughout this Chapter).

Signal events are identified using the J/ψ meson decay into two oppositely charged muons ($B(J/\psi \to \mu^+ \mu^-) = 5.93 \pm 0.06\,\%$), to which one charged track, assumed to be a pion, is paired to form a $B_c^+ \to J/\psi \pi^+$ candidate.

$B_c^+ \to J/\psi \pi^+ \pi^+ \pi^-$ candidates are analogously formed by combining a J/ψ candidate with three tracks, assuming that they are pions and requiring their total charge to be +1.

The same analysis strategy as for the $B_c^+ \to J/\psi \pi^+$ channel (except for the mass

hypothesis assigned to the track) is adopted to reconstruct the $B^+ \to J/\psi K^+$ decay, which is used as reference channel in the cross section measurement.

The event selection criteria have been first optimized on the $B_c^+ \to J/\psi \pi^+ \pi^+ \pi^-$ channel, which is affected by high combinatorial background; the kinematic region defined by the optimal selection cuts ($p_T(B_c) > 15$ GeV and $|y(B_c)| < 1.6$) is then propagated to the three-body decay $B_c^+ \to J/\psi \pi^+$ and, consequently, to the high-statistics decay $B^+ \to J/\psi K^+$.

Signal yields are extracted through unbinned maximum likelihoods fit to the resulting invariant mass distributions.

The ratio of the event yields is then converted into a measurement of the branching fractions R_{B_c} or cross sections times branching fractions $R_{c/u}$. Data are weighted event-by-event with the corresponding reconstruction efficiency as evaluated from the MonteCarlo (MC) simulation. Indeed, an accurate study of the selection efficiency and its dependence on the event kinematics is performed for each of the three decay modes considered in the analysis. The efficiency is modeled as a function of the meson transverse momentum for the three-body decays, while a more complicate set of variables (invariant mass combinations of the particles in the final state) is exploited for the parametrization of the reconstruction efficiency for the B_c five-body decay. Furthermore, the increasing instantaneous luminosity of the LHC during the data-taking has led to trigger menu evolving throughout the year. The different online requirements have been taken into account in the evaluation of the efficiency.

The efficiency-corrected data are fit with an unbinned maximum likelihood estimator, and the measurements of R_{B_c} and $R_{c/u}$ are obtained.

A careful evaluation of systematic uncertainties is carried out by considering contributions from the experimental methods employed in the analysis, the limited accuracy of the simulation and object reconstruction. Other sources of systematic uncertainties (integrated luminosity, trigger efficiency, muon reconstruction efficiency, $J/\psi \to \mu^+ \mu^-$ branching fraction) are not considered, since they cancel out in the ratio.

4.2 Dataset and triggers

This analysis is based on data collected by the CMS experiment at 7 TeV during the 2011 data-taking. During this data acquisition period, LHC delivered a maximum instantaneous luminosity (L) of 5×10^{33} cm^{-2}s^{-1}, with an average of 7.5 inelastic pp collisions per bunch crossing at the CMS interaction region.

The events are required to fulfill a good-run selection for muons, that is, data of good quality from the central tracker and the muon system. No additional requirement on the calorimeters status during the data taking is applied. The sample corresponds to an integrated luminosity (L_{int}) of 5.1 fb^{-1}.

4.2.1 MonteCarlo samples

High statistics MonteCarlo samples are used to optimize the selection cuts and measure the reconstruction efficiency.

Simulated events containing a B$_c$ meson have been generated using the dedicated B$_c$ meson generator as explained in Sec. 2.4. The B$_c$ decay modes $B_c^+ \to J/\psi \pi^+$, $B_c^+ \to J/\psi \pi^+ \pi^+ \pi^-$ and $B_c^+ \to J/\psi a_1 (a_1 \to \rho(770)\pi^+)$ have been simulated.

In order to optimize the sample production, acceptance cuts have been applied at generator level: a minimum p_T cut, $p_T(B_c) > 9$ GeV, and the rapidity interval $|y(B_c)| < 2.5$ have been required.

A simulated $B^+ \to J/\psi K^+$ sample is used to measure the reconstruction efficiency of the B^+ meson. Acceptance cuts at generator level are not applied for the production of this sample.

The transverse momentum and rapidity distributions of the generated particles are shown in Fig.4.1 and Fig.4.2 for the B_c^+ and the B^+ mesons, respectively.

4.2.1.1 Pileup distribution in the simulation

The simulated samples are generated with a distribution for the number of pileup interactions which is meant to cover the conditions expected for the whole 2011 Run.

The 2011 data-taking can be divided into three main instantaneous-luminosity periods (see Tab. 4.1), with an average number of reconstructed primary vertices of 5.4, 6.3 and 9.6 respectively. In order to accurately describe the actual data-taking conditions in each of the three luminosity phases, the MC sample is divided in three subsamples and the simulated primary vertex distribution is reweighted accordingly to the primary vertex distribution of data in the three periods.
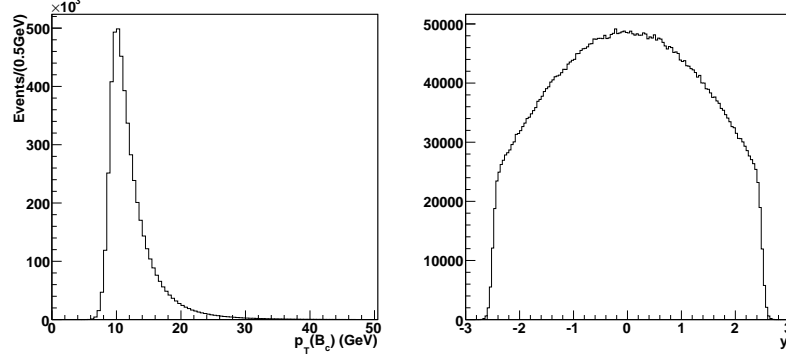
Figure 4.1: Transverse momentum (left) and rapidity (right) distributions of the B_c^+ meson at generator level.
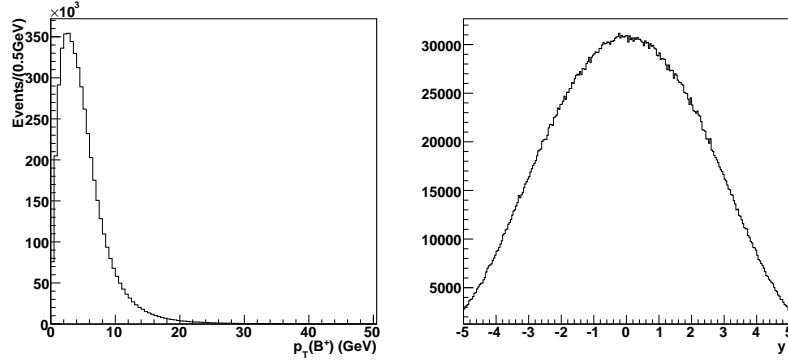

Figure 4.2: Transverse momentum (left) and rapidity (right) distribution of the B^+ meson at generator level.

The reweighting procedure is based on the actual number of pileup vertices per event (not the number of reconstructed primary vertices), allowing for a more careful emulation of the experimental environment. In fact, despite the primary vertex reconstruction with the Deterministic Annealing strategy (see Sec.3.7.1) is efficient and well-behaved up to relatively high levels of pileup, the final distribution for the number of reconstructed primary vertices is sensitive to the details of the primary vertex reconstruction and to differences in the underlying event in data versus simulation. Furthermore, the distribution for the number of reconstructed vertices can be biased by the offline event selection

criteria and even by the trigger.

In order to factorize these effects, instead of reweighting the Monte Carlo by the number of reconstructed Primary Vertices, the number of pileup interactions from the simulation truth is considered. The target pileup distribution for data is derived using the per-bunch-crossing-per-luminosity-section instantaneous luminosity together with the total pp inelastic cross-section to generate an expected pileup distribution, correctly weighted by the per-bunch-crossing-per-luminosity section integrated luminosity over the entire data-taking period.

The data and $B_c^+ \to J/\psi \pi^+$ MC reconstructed primary vertex distributions are compared in Fig. 4.3 before and after the pileup reweighting procedure is applied to the simulation. The data and reweighted MC distributions are in good agreement.

The same reweighting strategy is applied on the $B_c^+ \to J/\psi \pi^+ \pi^+ \pi^-$ and $B^+ \to J/\psi K^+$ simulated samples, and similar results are achieved.

4.2.2 Online selection

All L1 triggers involved in this analysis require the presence of two high quality muon objects in the event. L1 muons are requested to have $|\eta_{L1}| < 2.4$, and no cut on the muon transverse momentum is applied.

The HLT selection is based on two opposite-charge L3 muons, having a dimuon invariant mass within the J/ψ mass window (2.9 - 3.3 GeV). A vertex fit is performed to the two muon tracks to identify their crossing point. A minimum probability for the dimuon vertex (0.5%) and a minimum J/ψ transverse momentum (6.9 GeV) are required. In order to reject prompt produced J/ψ, the dimuon vertex is required to be displaced from the beamspot; the distance between the dimuon vertex and the beamspot ($L_{J/\psi}$), evaluated in the transverse plane, is required to be greater than three times its corresponding uncertainty ($\sigma_{L_{J/\psi}}$). In addition, the cosine of the angle α between $L_{J/\psi}$ and the J/ψ transverse momentum is required to be greater than 0.9. A selection based on the distance of closest approach (DCA) between the two muon tracks is also applied to reduce the pileup effects.

With the increase in the instantaneous luminosity of the LHC, tighter thresholds were applied to the muon momentum, pseudorapidity and dimuon vertex probability, in order to maintain an acceptable trigger rate. The evolving trigger requirements are summarized in Tab.4.2. The tighter selections will imply a lower efficiency for the B_c^+ and B^+ reconstruction, as shown later. The integrated luminosity collected by each trigger path is reported in Tab.reftab:lumi.
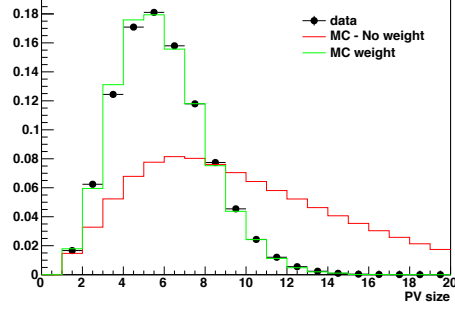
(a) $L = (1 + 1.4) \cdot 10^{33}$ cm^{-2} s^{-1}
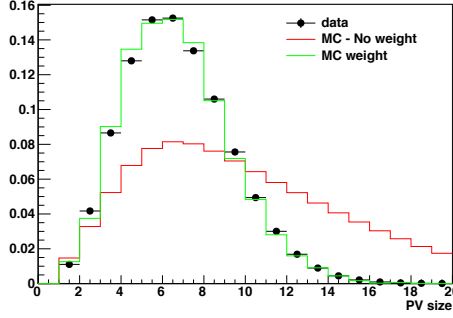
(b) $L = 2 \cdot 10^{33}$ cm^{-2} s^{-1}
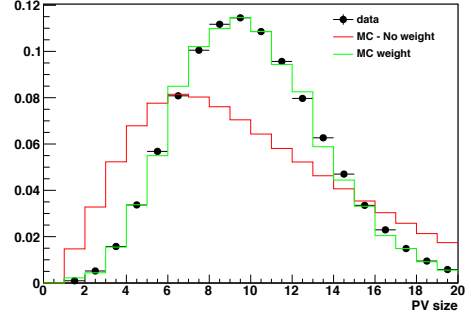
(c) $L = (3 + 5) \cdot 10^{33}$ cm^{-2} s^{-1}

Figure 4.3: Number of reconstructed primary vertices in data and MC ($B_c^+ \to J/\psi \pi^+$ sample) with and without pileup reweighting, for the three instantaneous-luminosity periods of Run I data-taking.

L (cm^{-2}s^{-1})	L_{int} (pb^{-1})	HLT Path
$1 \, (1.4) \cdot 10^{33}$	980	HLT_Dimuon7_Jpsi_Displaced
$2 \cdot 10^{33}$	924	HLT_DoubleMu3p5_Jpsi_Displaced
$3 \, (5) \cdot 10^{33}$	3139	HLT_DoubleMu4_Jpsi_Displaced

Table 4.1: Scheme of the three instantaneous luminosity periods of Run I, corresponding integrated luminosity and displaced J/ψ trigger path.

HLT Path	L1 seed	p_T^μ (GeV)	$|\eta^\mu|$	vtx CL
HLT_Dimuon7_Jpsi_Displaced	L1_DoubleMu0	0	2.4	0.5%
HLT_DoubleMu3p5_Jpsi_Displaced	L1_DoubleMu0	3.5	2.2	10%
HLT_DoubleMu4_Jpsi_Displaced	L1_DoubleMu0_HighQ	4	2.2	15%

Table 4.2: Selection requirements, implemented at HLT level, that changed in value during the 2011 data-taking.

4.3   Offline event selection

In the offline reconstruction the analysis is driven by the J/ψ meson identification via its decay into two opposite-charge muons.

The muon selection has been studied specifically for B-physics analyses (see also Sec.3.8). The two muons are required to have a track matched with at least one muon segment, and, in order to suppress muons from decays in flight, their transverse (longitudinal) impact parameter with respect to the primary vertex must be less than 3 cm (30 cm). For the same reason, and to guarantee a good p_T measurement, the muon tracks must leave at least 11 hits in the tracker, with at least 2 from the pixel detector. Finally, the hadronic punch-through is suppressed by requiring a track fit χ^2 per degree of freedom less than 1.8.

The J/ψ candidates formed by the two muons have to match the trigger criteria, and the muons themselves are required to be consistent with those which fired the trigger in a $\Delta R = \sqrt{(\Delta\eta)^2 + (\Delta\phi)^2}$ cone of 0.5.

The behavior of the trigger turn-on curves of the main variables ($p_T^{J/\psi}$, $L_{J/\psi}/\sigma_{L_{J/\psi}}$, $\cos\alpha$ and dimuon vertex probability) is studied in data and MC to verify that data are well reproduced by the simulation.

The study is performed for the two trigger paths HLT_Dimuon7_Jpsi_displaced and HLT_DoubleMu4_Jpsi_displaced. The HLT_DoubleMu3p5_Jpsi_displaced path is, indeed, very similar to the last one. The prescaled inclusive J/ψ trigger HLT_Dimuon0_Jpsi is used to select an unbiased sample of J/ψ mesons. This trigger path requires two muons with dimuon invariant mass in the J/ψ mass window and a minimum vertex probability (0.5%); it is used to study the $p_T^{J/\psi}$, $L_{J/\psi}/\sigma_{L_{J/\psi}}$ and $\cos\alpha$ requirements.

One variable is studied at a time. The requirements on the other two variables are applied in the offline reconstruction in order to disentangle the effects of the different selection cuts. Let's define $N_{Dimuon7}$ ($N_{DoubleMu4}$) as the number of reconstructed J/ψ's firing both the HLT_Dimuon7_Jpsi_displaced (HLT_DoubleMu4_Jpsi_displaced) and the HLT_Dimuon0_Jpsi paths, and

$N_{Dimuon0}$ as the number of reconstructed J/ψ's selected by the HLT_Dimuon0_Jpsi trigger and satisfying the offline requirements on those variables not under study.

The idea is to study the behavior of the ratio $N_{Dimuon7}/N_{Dimuon0}$ as a function of the variable under investigation, and compare data and MC turn-on curves. If the simulation well reproduces the data, the turn-on curves should reach the plateau at the same cut value.

The data and MC turn-on curves corresponding to $p_T^{J/\psi}$, $L_{J/\psi}/\sigma_{L_{J/\psi}}$ and $\cos\alpha$ are shown in Fig.4.4. These plots show that:

- $p_T^{J/\psi}$: the ratio $N_{Dimuon7}/N_{Dimuon0}$ reaches the plateau at 7.1 GeV, both in data and MC. The ratio $N_{DoubleMu4}/N_{Dimuon0}$ is already flat at 7 GeV due to the requirement on the single muon transverse momentum (p_T > 4 GeV). The requirement $p_T^{J/\psi} \geq 7.1$ GeV is introduced in the offline analysis to ensure a uniform behavior of the trigger for data and MC.

- $L_{J/\psi}/\sigma_{L_{J/\psi}}$: the turn-on curves are flat where $L_{J/\psi}/\sigma_{L_{J/\psi}} \geq 5$. Therefore the requirement $L_{J/\psi}/\sigma_{L_{J/\psi}} \geq 5$ is applied in the offline selection.

- $\cos\alpha$: no significant discrepancy is found between the data and MC turn-on curves. The online requirement $\cos\alpha > 0.9$ is thus repeated in the offline selection.

In order to study the turn-on curve of the dimuon vertex probability, the unbiased J/ψ sample is selected with the HLT_Dimuon0_Jpsi_NoVertexing trigger path, which does not require any minimum dimuon vertex confidence level. Since this path is only available in the last part of the data sample, the study is performed only for the HLT_DoubleMu4_Jpsi_displaced trigger. The ratio $N_{DoubleMu4}/N_{Dimuon0\_NoVtx}$ evolved as a function of the dimuon vertex probability is shown in Fig.4.5: data and MC turn-on curves have a similar behavior, thus the offline requirement is set to reproduce the online selection.

After the selection procedure described so far, only one J/ψ per event is reconstructed in 99.99% of cases, while in the remaining 0.01% of events two J/ψ candidates are found. In the latter case, both J/ψ's are retained for the following analysis steps.

The $B_c^+ \to J/\psi\pi^+$ ($B^+ \to J/\psi K^+$) candidates are formed by combining a J/ψ candidate with one track, assuming that it is a pion (kaon). The track must not be identified as a muon. The $B_c^+ \to J/\psi\pi^+\pi^+\pi^-$ candidates are analogously formed by combining a J/ψ candidate with three tracks, assuming that
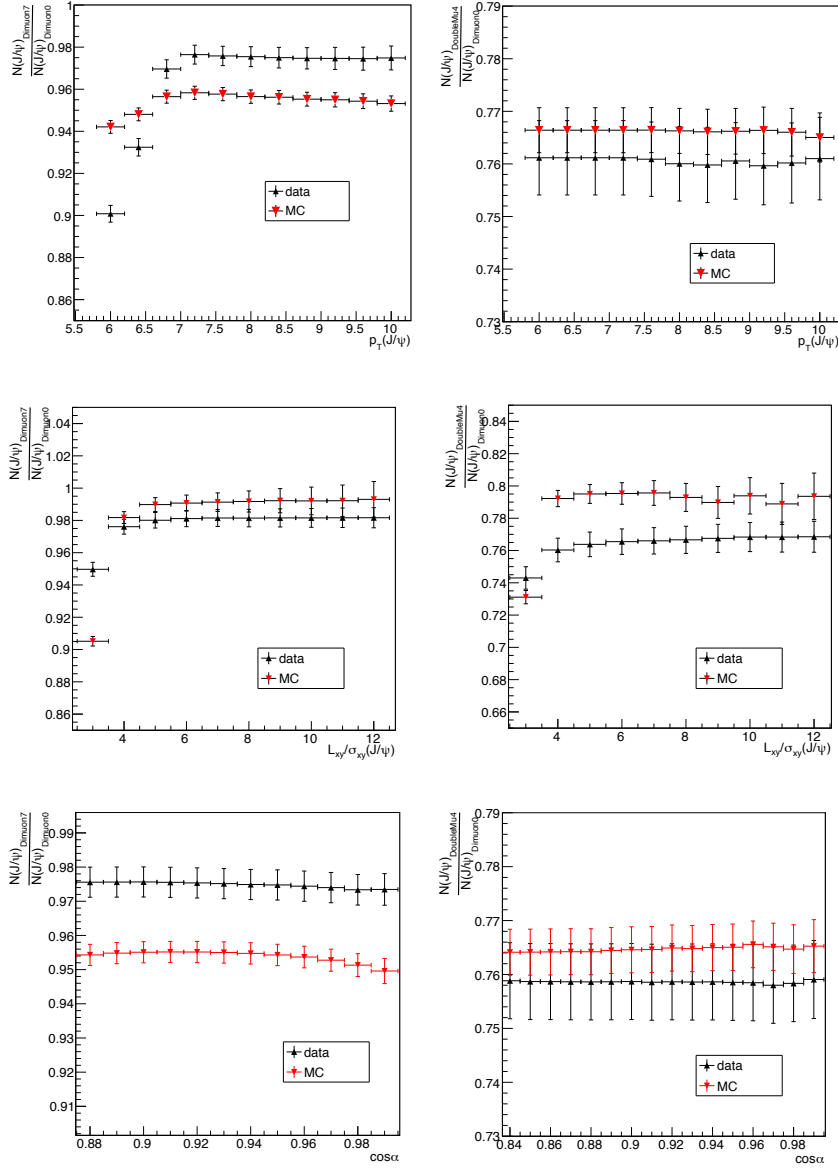
Figure 4.4: Number of reconstructed J/ψ's firing the HLT_Dimuon7_Jpsi_displaced (left) or HLT_DoubleMu4_Jpsi_displaced (right) trigger normalized to the number of J/ψ's collected by the inclusive trigger, as a function of an offline cut on $p_T^{J/\psi}$ (first row), $L_{J/\psi}/\sigma_{L_{J/\psi}}$ (second row) and $\cos\alpha$ (third row).
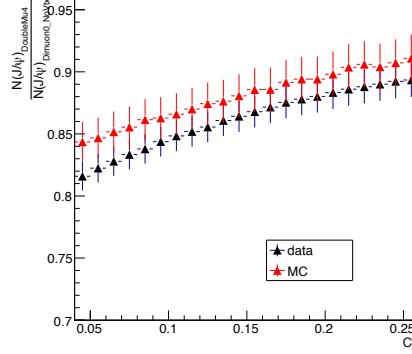
Figure 4.5: Number of reconstructed J/ψ firing the HLT_DoubleMu4_Jpsi_displaced trigger normalized to the J/ψ collected by the inclusive trigger, as a function of an offline cut on the dimuon vertex probability.

they are pions and requiring their total charge to be $+1$. The pion (kaon) candidates must have a track fit χ^2 less than three times the number of degrees of freedom; ≥ 6 tracker hits; ≥ 2 pixel hits; $|\eta| < 2.4$; and $p_T > 0.9$ GeV.

The three-dimensional impact parameter (IP) significance between each pion and the J/ψ vertex is set ≤ 6 to reduce combinatorial background and effect of pileup, and limit the vertexing computing time. The value $\mathrm{IP}(\pi, J/\psi) \leq 6\sigma_{IP}$ is inferred from the signal MC simulation (see Fig.4.6).

The ΔR between the J/ψ and the pion track is required to be < 2.5; this value is obtained from the $B_c^+ \to J/\psi\pi^+$ simulation (shown in the left plot of Fig. 4.7). For the $B_c^+ \to J/\psi\pi^+\pi^+\pi^-$ mode, a ΔR cut is applied on each of the three pions in the event. In particular, $\Delta R < 1$ is required for the highest p_T track (referred to as π_1), while $\Delta R < 1.6$ is required for the other two pions (π_2 and π_3). The corresponding MC distributions are shown in the right plot of Fig. 4.7.

The decay vertex is reconstructed using a kinematic vertex fit (see Sec.3.7.3), which constrains the invariant mass of the two muons to the J/ψ nominal mass. The three (five) track vertex fit confidence level is required to be greater than 0.001. After the vertex fit, the track parameters are re-estimated at the fitted vertex, effectively using this vertex as a constraint.

In case of multiple B_c^+ (B^+) candidates, the one with highest p_T is retained. Additional topological selections are required to improve the signal-to-background ratio, and are optimized separately for the $B_c^+ \to J/\psi\pi^+\pi^+\pi^-$ and $B_c^+ \to J/\psi\pi^+$ signals, as described in the following Sections.
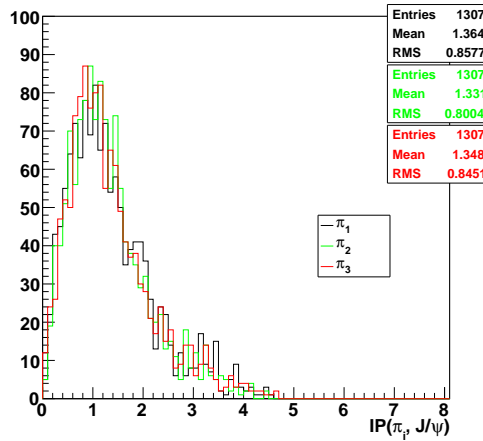
Figure 4.6: Significance of the 3D impact parameter between each pion and the J/ψ vertex in the simulation. The distribution is computed at the level of the pre-selection (after trigger cuts and the requirement of a valid five-track vertex), for those events lying in the B_c mass range.
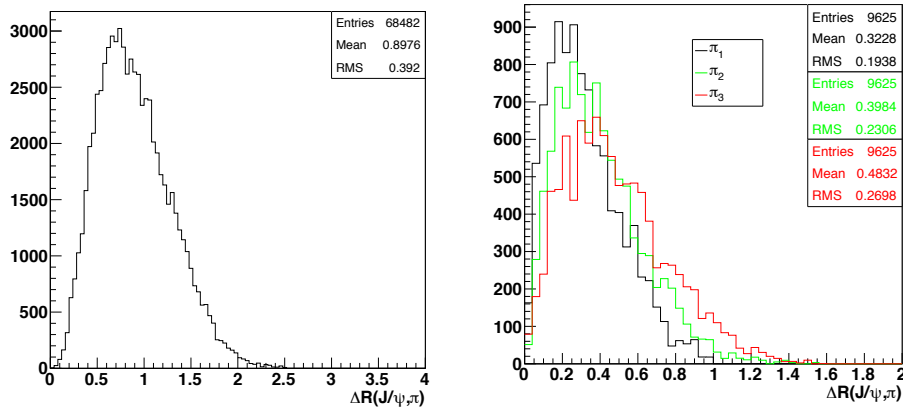

Figure 4.7: $\Delta R(J/\psi, \pi)$ from $B_c^+ \to J/\psi \pi^+$ (left) and $B_c^+ \to J/\psi \pi^+ \pi^+ \pi^-$ (right) MC simulation.

4.3.1 $B_c^+ \to J/\psi \pi^+ \pi^+ \pi^-$ signal

The selection cuts are optimized maximizing the $S/\sqrt{(S+B)}$ figure of merit, where S is the signal yield obtained from a Gaussian fit to the MC reconstructed events, rescaled to the data integrated luminosity, and B is the amount of background extrapolated from the $J/\psi \pi^+ \pi^+ \pi^-$ invariant mass sidebands in the data. The two sideband regions are defined as being between $5\sigma_{m(B_c)}$ and $8\sigma_{m(B_c)}$ of the world-average B_c mass [101], where $\sigma_{m(B_c)}$ is the resolution of the signal as determined in simulation.

The optimization procedure evaluates $S/\sqrt{(S+B)}$ over a N-dimensional grid, where N is the number of the variables on which the selection is optimized. The selection cuts scanned for the optimization are: $p_T(B_c)$; $y(B_c)$; five-track vertex probability; $cos\theta$, where $cos\theta = L \cdot p_{B_c}/(|L||p_{B_c}|)$, evaluated with respect to the beamspot, in the xy plane; $p_T(\pi_1)$, $p_T(\pi_2)$ and $p_T(\pi_3)$, where π_1, π_2 and π_3 are sorted from the highest to the lowest p_T; $\Delta R(J/\psi, \pi_s)$ where π_s is the vector sum of the three-pion quadrimomenta.

The procedure selects the following cut set:

- $p_T(B_c) > 15$ GeV,

- $|y(B_c)| < 1.6$,

- five-track vertex probability > 20%,

- $cos\theta > 0.99$,

- $p_T(\pi_1) > 2.5$ GeV, $p_T(\pi_2) > 1.7$ GeV, $p_T(\pi_3) > 0.9$ GeV,

- $\Delta R(J/\psi, \pi_S) < 0.5$.

A check has been performed scanning one selection cut at a time and searching for the maximum of $S/\sqrt{(S+B)}$. The selection cut under optimization is varied from the loosest to the tightest value considered in the full optimization procedure, while all other cuts are applied with their optimized value. The single-cut value corresponding to the maximum of $S/\sqrt{(S+B)}$ identified with this strategy coincides with the value suggested by the grid scan. The corresponding plots are collected in App.A.

The $J/\psi \pi^+ \pi^+ \pi^-$ invariant-mass distribution after all the selection cuts are applied is shown in Fig.4.8. A fit is performed with an unbinned maximum likelihood estimator. The signal is parametrized as a Gaussian distribution and the background as a second-order Chebychev polynomial. The signal yield is 92 ± 27 events and fitted mass and resolution values are 6.266 ± 0.006 GeV and 0.021 ± 0.006 GeV, respectively, where the uncertainties are statistical only.
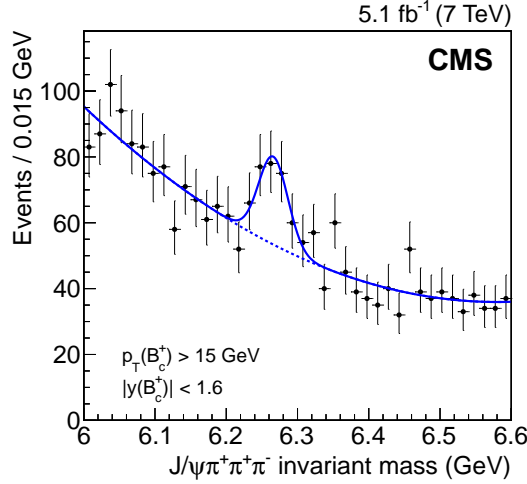
Figure 4.8: $J/\psi\pi^+\pi^+\pi^-$ invariant mass distribution. The result of the fit is super-imposed: the solid line represent the signal-plus-background fit (Gaussian distribution for the signal and second-order Chebychev polynomial for the background) and the dashed one is the background-only component.

4.3.1.1 Background studies

The main contribution to background events comes from the association of a displaced J/ψ meson with three random tracks. This background has a smooth trend in the invariant mass distribution.

Peaking background events from B meson decays should be negligible in the considered invariant mass range. Since the B_c meson mass is ~ 1 GeV higher than that of the other B mesons, it is in fact unlikely to have contributions due to misidentified or partially reconstructed B decays in the B_c signal region.

However, a non-smooth behavior of the background or peaking structures can arise in this region due to other misidentified or partially reconstructed B_c decays. Possible contamination from different B_c decay modes is therefore investigated.

A search for $B_c^+ \to J/\psi K^+K^-\pi^+$ events is performed by assigning the kaon mass to two opposite-charge tracks. No hints of B_c^+ mesons decaying into this final state is observed in data with the applied selection cuts.

A possible effect due to an undetected π^0 from the decay $B_c^+ \to J/\psi\pi^+\pi^+\pi^-\pi^0$ is also investigated on a dedicated MC sample. The partially reconstructed $J/\psi\pi^+\pi^+\pi^-$ mass spectrum from the simulation is fit

with an ARGUS function [102] convolved with a Gaussian distribution describing the detector resolution. The resulting parametrization is added to a linear polynomial function to describe the background in the fit to the $J/\psi\pi^+\pi^+\pi^-$ mass spectrum in data (Fig. 4.9). Since no significant variation in the $B_c^+ \rightarrow J/\psi\pi^+\pi^+\pi^-$ signal yield is found with this background model and, most importantly, the relative amount of $B_c^+ \rightarrow J/\psi\pi^+\pi^+\pi^-\pi^0$ is unknown, the parametrization of the background with a second order Chebychev polynomial is chosen.
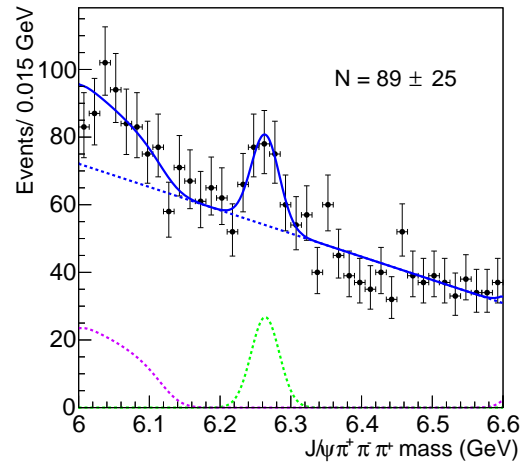
Figure 4.9: Alternative fit to the $J/\psi\pi^+\pi^+\pi^-$ invariant mass distribution. The different components are represented (dashed lines): the signal is parametrized with a Gaussian distribution (green) and the combinatorial background with a linear polynomial (blue). An Argus function convolved with a Gaussian distribution for the detector resolution is used to model partially reconstructed $B_c^+ \rightarrow J/\psi\pi^+\pi^+\pi^-\pi^0$ decays (violet).

4.3.2 $B_c^+ \to J/\psi\pi^+$ **signal**

The same figure of merit $S/\sqrt{(S+B)}$ is maximized in the selection of the $B_c^+ \to J/\psi\pi^+$ channel. $S/\sqrt{(S+B)}$ is evaluated on a N-dimensional grid in the same kinematic phase space as defined for the $B_c^+ \to J/\psi\pi^+\pi^+\pi^-$ decay (i.e. $p_T(B_c) > 15$ GeV and $|y(B_c)| < 1.6$). The procedure points at the following cut set:

- three-track vertex probability $> 6\%$,

- $cos\theta > 0.9$,

- $p_T(\pi) > 2.7$ GeV,

- $\Delta R(J/\psi, \pi) < 1$.

One selection cut is then scanned at a time searching for the maximum of $S/\sqrt{(S+B)}$ to check the optimization procedure. As explained in the previous Section, the selection cut under optimization is varied from the loosest to the tightest value considered in the full optimization procedure, while all other cuts are applied with their optimal value. Plots collected in App. A show that the single-cut value corresponding to the maximum of $S/\sqrt{(S+B)}$ as identified with this strategy coincides with the value suggested by the grid scan.

The $B_c^+ \to J/\psi\pi^+$ signal is shown in Fig. 4.10. The $J/\psi\pi^+$ invariant-mass distribution is fit through an unbinned maximum likelihood estimator. The signal is parametrized with a Gaussian distribution and the background as a second order Chebychev polynomial. The B_c^+ signal yield is 176 ± 19 and fitted mass is 6.267 ± 0.003 GeV (statistical uncertainty only). The fitted resolution value is 0.025 ± 0.003 GeV.

4.3.2.1 Background studies

Contamination from other B_c^+ decay modes is investigated. A possible reflection of the Cabibbo-suppressed $B_c^+ \to J/\psi K^+$ mode in the $J/\psi\pi^+$ mass spectrum is modeled on a simulated sample of $B_c^+ \to J/\psi K^+$ events with a Crystal Ball distribution [103]. Its contribution in data is constrained using the value of the relative branching fraction to $B_c^+ \to J/\psi\pi^+$ [67].

Furthermore, the effect due to a possible undetected π^0 from $B_c^+ \to J/\psi\pi^+\pi^0$ decay is modeled from a dedicated MC sample. The partially reconstructed $J/\psi\pi^+$ mass spectrum obtained from the simulated events is fit with an ARGUS function convolved with a Gaussian function describing the detector resolution. The resulting parametrization, added to a linear polynomial function, is used to describe the background in the fit to the $J/\psi\pi^+$ mass spectrum in data.
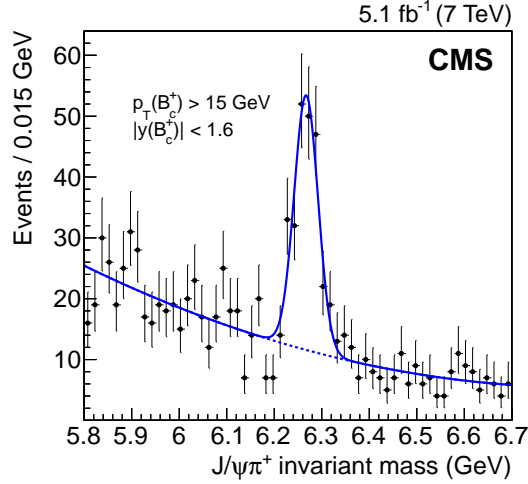
Figure 4.10: $J/\psi\pi^+$ invariant mass distribution. The result of the fit is superimposed; the lines represent the signal-plus-background fit (solid) and the background-only component (dashed).

Fig. 4.11 shows the result of the fit to the $J/\psi\pi^+$ invariant mass distribution with the background parametrization discussed above. No significant variation of the $B_c^+ \to J/\psi\pi^+$ signal yield is found, nor the fit χ^2 improves. Thus, the second-order Chebychev polynomial is chosen to describe the background contribution.

4.3.3 $B^+ \to J/\psi K^+$ signal

The $B^+ \to J/\psi K^+$ signal is obtained with the same selection cuts as for the $B_c^+ \to J/\psi\pi^+$ decay mode and is shown in Fig. 4.12. The $J/\psi K^+$ invariant mass distribution is fit with a sum of two Gaussian distributions with a common mean for the signal and a second-order Chebychev polynomial for the background. Additional contributions from partially reconstructed B^0 and B^+ decays are parametrized with functions determined from inclusive $B^+ \to J/\psi X$ and $B^0 \to J/\psi X$ MC samples. In particular, the $J/\psi K^+$ invariant mass distribution from the simulated samples B^+ and B^0 samples, shown in Fig. 4.13, is fit with a double-Gaussian distribution for the $B^+ \to J/\psi K^+$ signal, and two additional Gaussian distributions, one on the left side and one on the right side of the signal, accounting for the partially reconstructed B^0 and $B^+ \to J/\psi\pi^+$
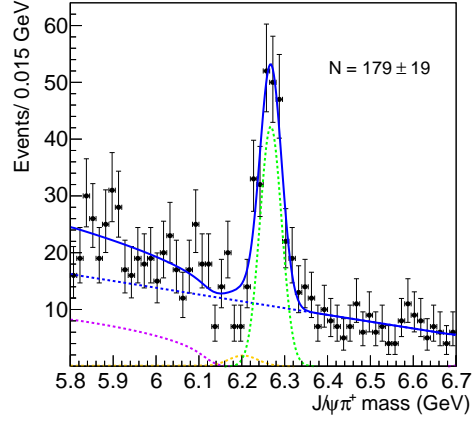
Figure 4.11: Fit to the $J/\psi\pi^+$ invariant mass distribution (solid line). The different components are represented (dashed lines): the signal is parametrized with a Gaussian distribution (green) and the background with a first-order polynomial (blue). The contribution from $B_c^+ \to J/\psi K^+$ decays is modeled with a Crystal Ball function (orange) and the partially reconstructed $B_c^+ \to J/\psi\pi^+\pi^0$ decays with an Argus function convolved with a Gaussian for the detector resolution (violet).

contributions respectively.

The $B^+ \to J/\psi K^+$ signal yield in data returned by the fit is 90419 ± 352, and fitted mass value is 5.2785 ± 0.0001 GeV.
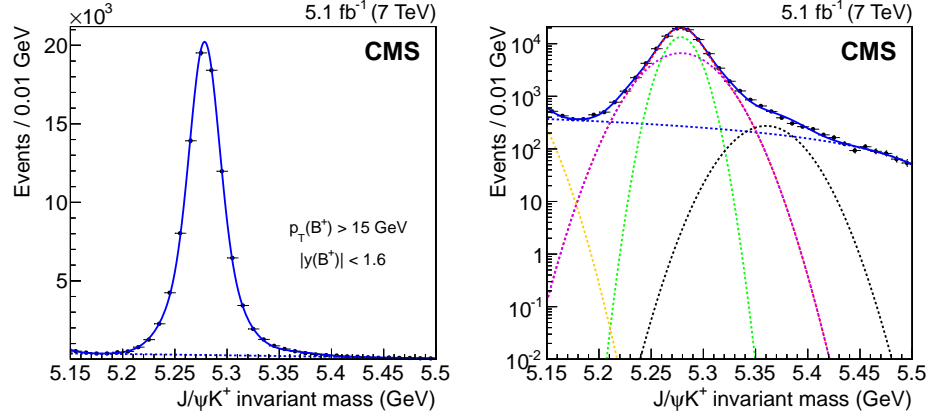
Figure 4.12: $J/\psi K^+$ invariant mass distribution with linear (left) and semi-logarithmic (right) scale. The result of the fit is superimposed with a solid blue line. The signal is parametrized with two gaussian, shown with the dashed green and violet lines in the right plot. The dashed black and yellow curves represent the $B^+ \to J/\psi \pi^+$ and B^0 contributions, respectively, while the dashed blue line represents the second order Chebychev polynomial.
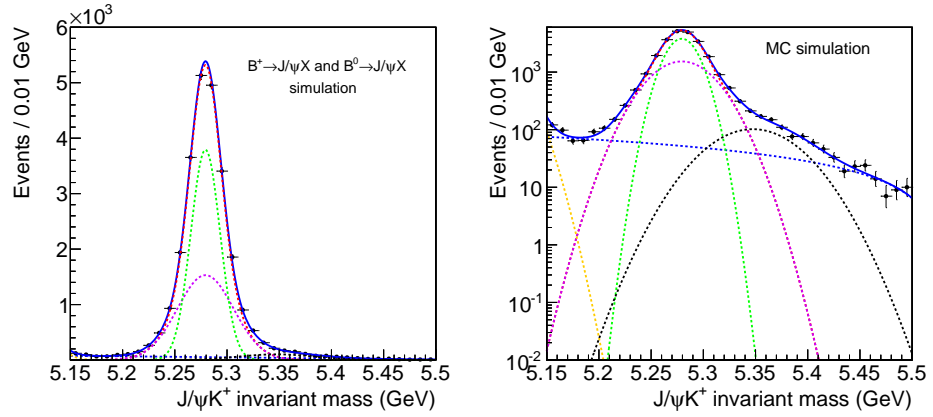
Figure 4.13: $J/\psi K^+$ invariant mass distribution obtained from simulated samples of $B^+ \to J/\psi X$ and $B^0 \to J/\psi X$ with linear (left) and semi-logarithmic (right) scale. A fit is superimposed: the dashed green and violet lines represents the double Gaussian distribution used to parametrize the $B^+ \to J/\psi K^+$ signal; the dashed black and yellow curves represent the $B^+ \to J/\psi \pi^+$ and B^0 contributions, respectively.

4.3.4 Data-simulation comparison

The distributions of the relevant variables are compared in data and MC. The comparison is performed for the $B_c^+ \to J/\psi \pi^+$ and $B^+ \to J/\psi K^+$ signals, where the available number of signal events in data is higher.

In Fig. 4.14 the distributions of the B_c transverse momentum and rapidity and the pion p_T are shown for the $B_c^+ \to J/\psi \pi^+$ signal. Background subtracted data distributions (error bars) are compared to those from the simulation (azure). Background distributions are derived from two sideband regions defined as being between $5\sigma_{m(B_c)}$ and $7\sigma_{m(B_c)}$ of the measured B_c^+ mass, where $\sigma_{m(B_c)}$ is the resolution of the signal as determined from the fit to data.

A Kolmogorov test [104] is performed to evaluate the compatibility of the distributions. The returned values for the probability are 0.98, 0.88 and 0.97 for $p_T(B_c)$, $y(B_c)$, and $p_T(\pi)$ respectively.

Figure 4.14: Background subtracted data distributions (black) of $p_T(B_c)$, $y(B_c)$ and pion p_T are compared to MC (azure) for the $B_c^+ \to J/\psi \pi^+$ channel. The hashed region represents the MC statistical error.

Fig. 4.15 shows the comparison between data and MC distributions for the B^+ signal. As done before, the background distributions are derived from two sideband regions defined as being between $5\sigma_{m(B^+)}$ and $7\sigma_{m(B^+)}$ of the measured B^+ mass, where $\sigma_{m(B^+)}$ is the resolution of the signal as determined from the fit to data.

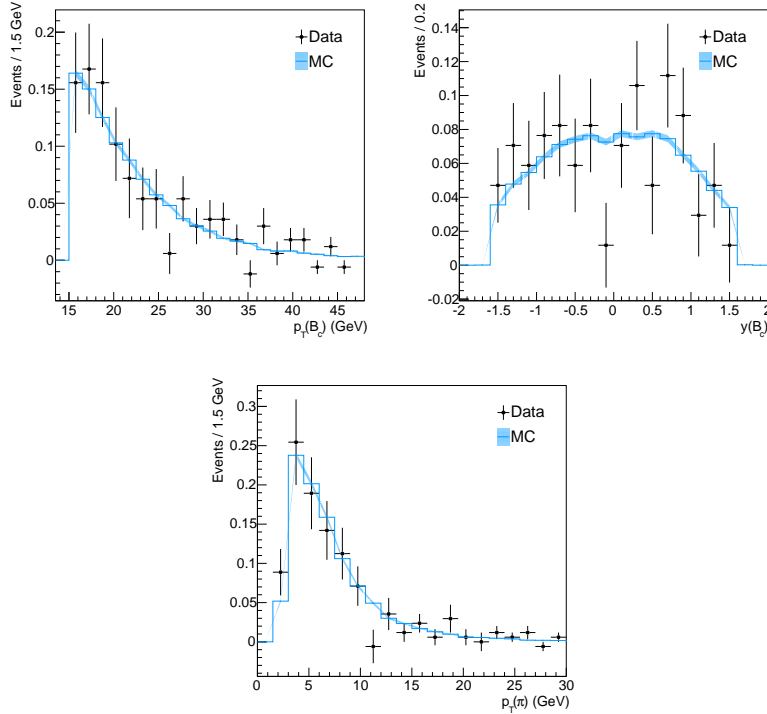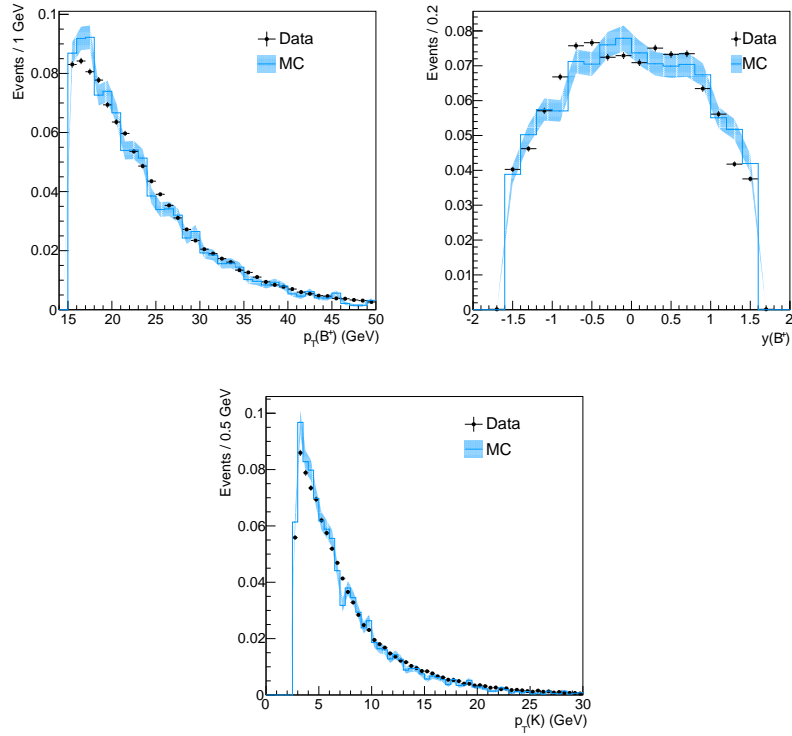**Figure 4.15:** Background subtracted data distributions (black) of $p_T(B^+)$, $y(B^+)$ and kaon p_T are compared to MC (azure). The hashed region represents the MC statistical error.

4.4 Measurement of R_{B_c}

The ratio R_{B_c} is defined as

$$R_{B_c} = \frac{B(B_c^+ \to J/\psi\pi^+\pi^+\pi^-)}{B(B_c^+ \to J/\psi\pi^+)} = \frac{Y_{3\pi}}{Y_{B_c}}, \qquad (4.1)$$

where $Y_{3\pi}$ and Y_{B_c} are the signal yields extracted from the efficiency-corrected invariant mass distributions for the $B_c^+ \to J/\psi\pi^+\pi^+\pi^-$ and $B_c^+ \to J/\psi\pi^+$ channels, respectively, in the kinematic region $p_T(B_c) > 15$ GeV and $|y(B_c)| < 1.6$.

4.4.1 Efficiency measurement for $B_c^+ \to J/\psi\pi^+\pi^+\pi^-$

The $B_c^+ \to J/\psi\pi^+\pi^+\pi^-$ decay can involve intermediate resonant states; indeed, the $\pi^+\pi^-\pi^+$ and $\pi^+\pi^-$ invariant mass projections from data show evidence for the presence of $a_1(1260)$ and $\rho(770)$ in the decay (Fig. 4.16).

The quantitative determination of the resonant contributions and their interferences in the decay requires a sophisticated amplitude analysis which is not feasible with the available amount of data. However, the reconstruction efficiency for the five-body decay could be affected by the decay dynamics, since different dynamics could favor, or disfavor, different regions of the phase space. It is then necessary to study the efficiency as a function of a complete set of variables for the five-body final state to gauge possible variations across the entire phase space.

A five-body decay of a spinless particle can be described in its center-of-mass frame by 20 variables, i.e. the 5 four-vectors of the final state. They are constrained by the 4 conservation (energy and momentum) equations and by the 5 particle masses in the final state. In addition, the initial state is isotropic (the B_c meson is a pseudoscalar) and the final state, in its rest frame, does not depend on the 3 angles describing the relative orientation.

In the end, the decay can be described by eight independent mass combinations of the type m_{ij}^2 $(i \neq j)$, where m_{ij}^2 is the squared invariant mass of the pair of particles i and j in the final state. In the present case, the J/ψ constraint on the dimuon invariant mass reduces the number of independent m_{ij}^2 to seven.

The following seven mass combinations have been chosen: $m^2(\mu^+\pi^+)_{low}$, $m^2(\pi^+\pi^-)_{high}$, $m^2(\mu^+\pi^-)$, $m^2(\pi^+\pi^+)$, $m^2(\mu^-\pi^+)_{low}$, $m^2(\mu^-\pi^+)_{high}$ and $m^2(\mu^-\pi^-)$; the "low" and "high" subscripts refer to the lower and higher invariant mass combination where a π^+ is involved.
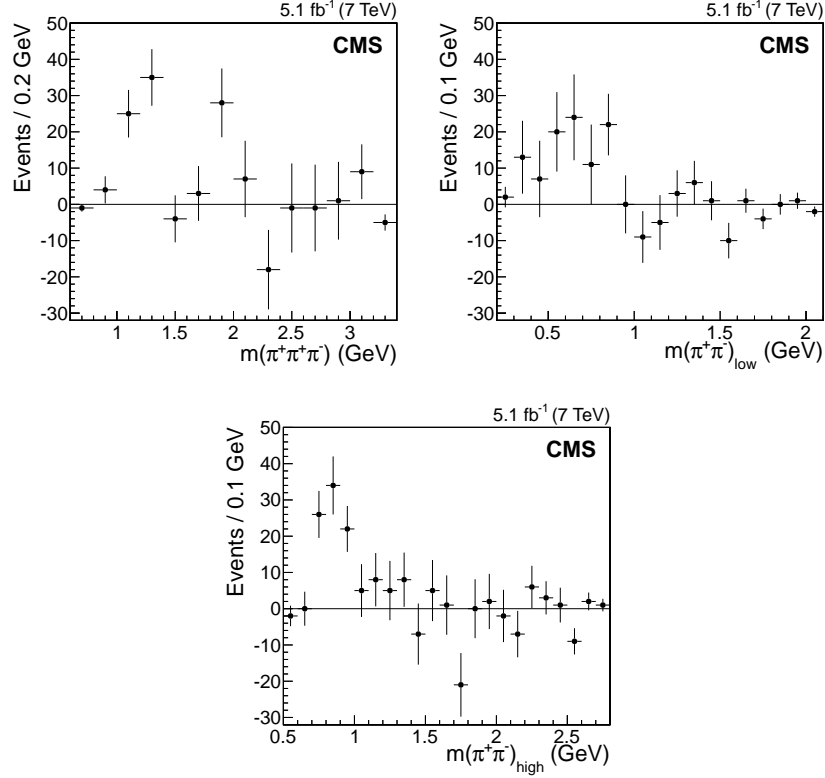
Figure 4.16: Background-subtracted invariant mass projection for $\pi^+\pi^-\pi^+$ (left), $(\pi^+\pi^-)_{low}$ (center) and $(\pi^+\pi^-)_{high}$ (right). Since two same-sign pions are present in the final state, we indicate with $(\pi^+\pi^-)_{low}$ the $\pi^+\pi^-$ pair with the lower invariant mass and with $(\pi^+\pi^-)_{high}$ the higher invariant mass combination.

The efficiency is parametrized as a linear function of these seven mass combinations:

$$\epsilon = |p_0 + p_1 \cdot x + p_2 \cdot y + p_3 \cdot z + p_4 \cdot w + p_5 \cdot r + p_6 \cdot t + p_7 \cdot v| \qquad (4.2)$$

where $x = m^2(\mu^+\pi^+)_{low}$, $y = m^2(\pi^+\pi^-)_{high}$, $z = m^2(\mu^+\pi^-)$, $w = m^2(\pi^+\pi^+)$, $r = m^2(\mu^-\pi^+)_{low}$, $t = m^2(\mu^-\pi^+)_{high}$, $v = m^2(\mu^-\pi^-)$ and p_i are free parameters to be determined via an unbinned maximum likelihood fit to the generated events in the seven-dimensional space using a binomial probability density function. The absolute value is required to prevent the function from assuming negative values.

The fit is performed on a non resonant $B_c^+ \to J/\psi \pi^+ \pi^+ \pi^-$ MC sample, which allows to access all the phase-space configurations. Generated events in the kinematic region $p_T(B_c) > 15$ GeV and $|y(B_c)| < 1.6$ are considered. Reconstructed events have to fulfill all the analysis requirements and lie in the invariant mass range within $3\sigma_{m(B_c)}$ from the B_c mass, where $\sigma_{m(B_c)}$ is the resolution of the signal as determined from the fit to simulation.

Different efficiency models have been tested by adding a few second order terms in the polynomial function, but no improvement in the fit χ^2 is found. The fit with a more complex function does not converge due to the limited number of simulated events.

The projections of the expected number of reconstructed events on the seven invariant-mass combinations are shown in Fig. 4.17 for simulated events selected by the HLT_Dimuon7_Jpsi_Displaced trigger path (for events selected by the other two trigger paths, see App.C). The number of reconstructed events is denoted with error bars, while the predicted number of events is represented with the continuous line.

Fig. 4.18 shows the expected number of reconstructed events for the three HLT paths used in the analysis (the number of predicted events per trigger path is not scaled by the corresponding integrated luminosity). As expected, the HLT_DoubleMu3p5_Jpsi_displaced and HLT_DoubleMu4_Jpsi_displaced paths collect fewer events than the looser trigger path HLT_Dimuon7_Jpsi_displaced. Precisely, the overall efficiency is reduced by ~ 16 and 32%, respectively.

The overall $B_c^+ \to J/\psi \pi^+ \pi^+ \pi^-$ selection efficiency, evaluated as the total number of reconstructed events divided by the total number of generated events in the considered kinematic region, and averaged over the three trigger paths according to the corresponding integrated luminosity in data, is $(6.13 \pm 0.10) \cdot 10^{-3}$.
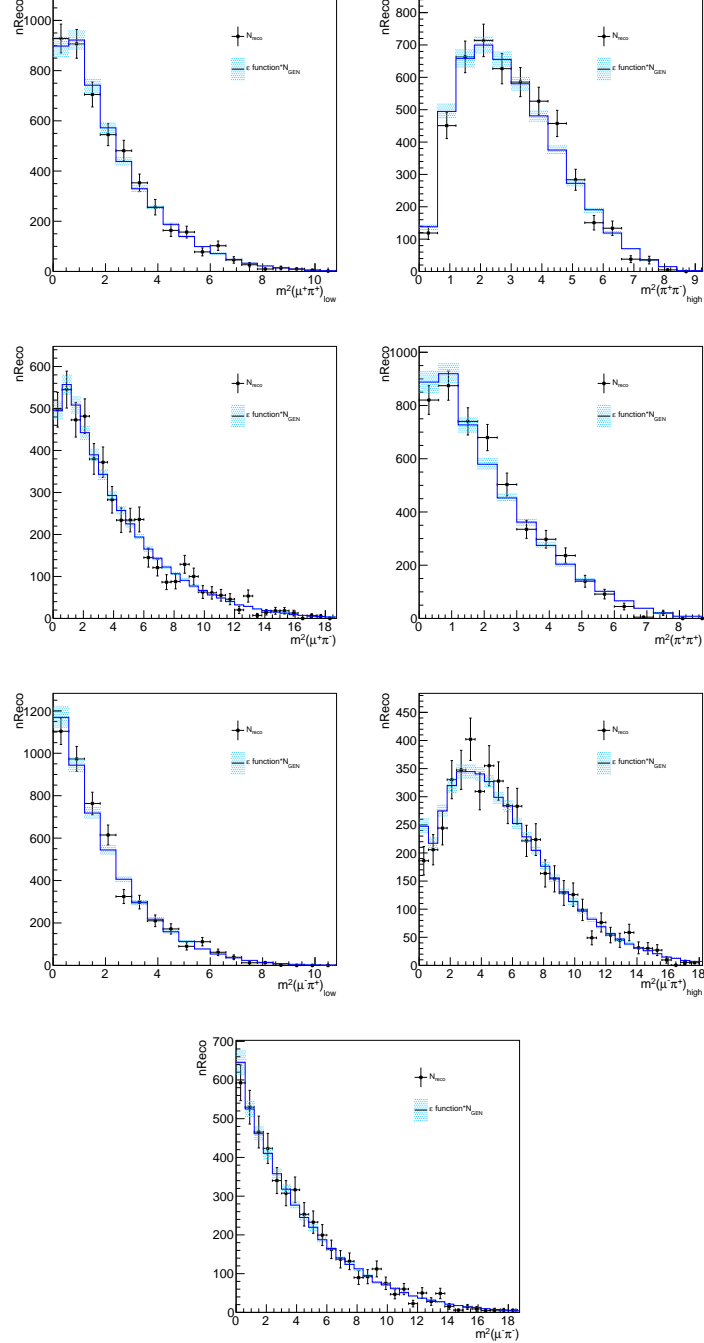
Figure 4.17: Number of simulated reconstructed events projected on the 7 two-body mass combinations used to describe the $B_c^+ \rightarrow J/\psi \pi^+ \pi^+ \pi^-$ decay. The black dots represent the number of reconstructed events; the blue line is the expected number of reconstructed events as resulting from the 7-dimensional fit; the hashed region represents the statistical uncertainty on the fit function. Events are selected with the HLT_Dimuon7_Jpsi_Displaced trigger.
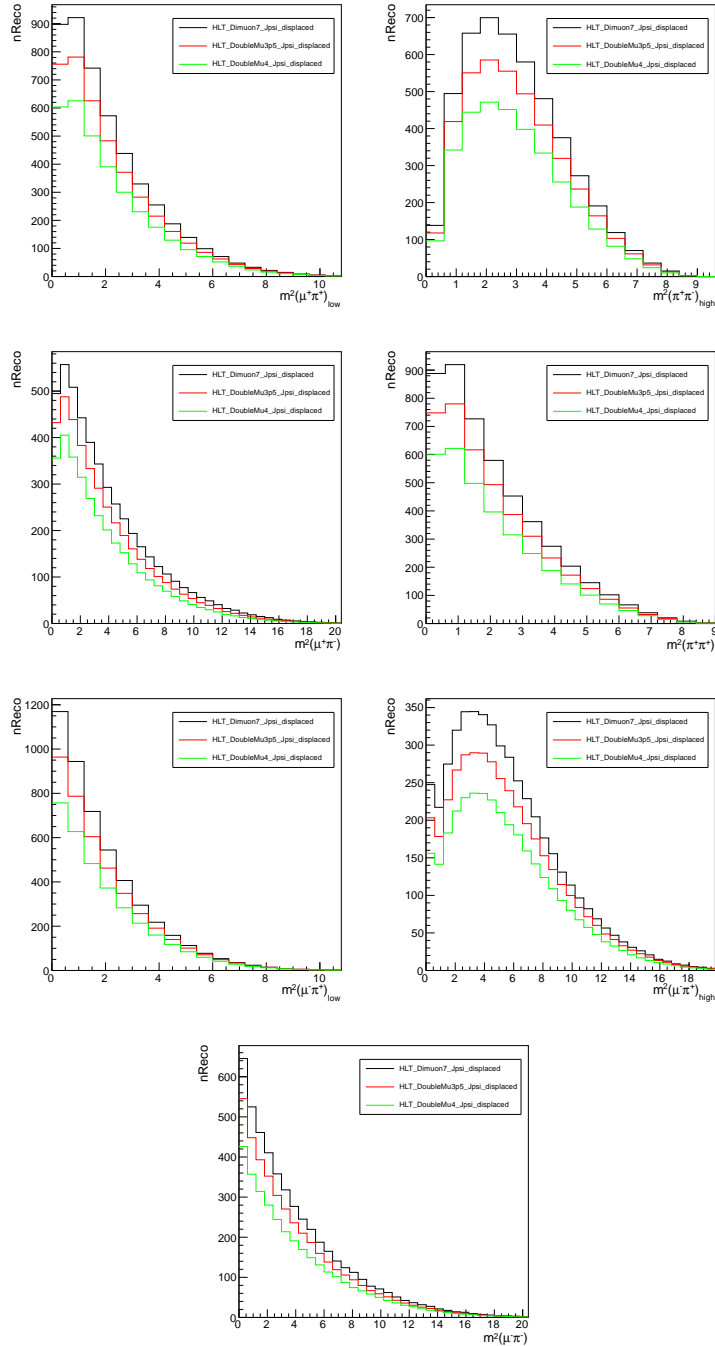
Figure 4.18: Projection on the 7 two-body mass combinations of the expected number of reconstructed events as resulting from the 7-dimensional fit, for each of the three HLT paths used in the analysis. The number of predicted events per trigger path is not scaled by the corresponding integrated luminosity.

4.4.2   Efficiency measurement for $B_c^+ \to J/\psi \pi^+$

The $B_c^+ \to J/\psi \pi^+$ reconstruction efficiency is measured as a function of the B_c^+ transverse momentum on the simulated $B_c^+ \to J/\psi \pi^+$ samples in 24 p_T-bins. The bin size is determined by the number of reconstructed events per bin available in the MC sample. The efficiency ε in the ith bin is evaluated as $\varepsilon_i = N_i^{reco}/N_i^{GEN}$, where N_i^{reco} is the number of reconstructed events in the given bin, obtained from a Gaussian fit to the invariant mass distribution of simulated events passing the full selection procedure. N_i^{GEN} is the number of generated B_c^+ events in the same p_T bin and within the rapidity region $|y(B_c)| < 1.6$.

The efficiency behavior as a function of $p_T(B_c)$ is shown in Fig. 4.19. As expected, the efficiency is lower when events are selected by the HLT_DoubleMu3p5_Jpsi_displaced and HLT_DoubleMu4_Jpsi_displaced paths, due to tighter requirements on muon transverse momentum and dimuon vertex probability. In particular, the overall efficiency is reduced by 14 and 29%, respectively, with respect to that achieved using the loosest trigger path. The overall $B_c^+ \to J/\psi \pi^+$ selection efficiency, integrated over p_T and averaged over the three trigger paths according to the corresponding collected integrated luminosity in data, is $(1.43 \pm 0.02) \cdot 10^{-2}$.
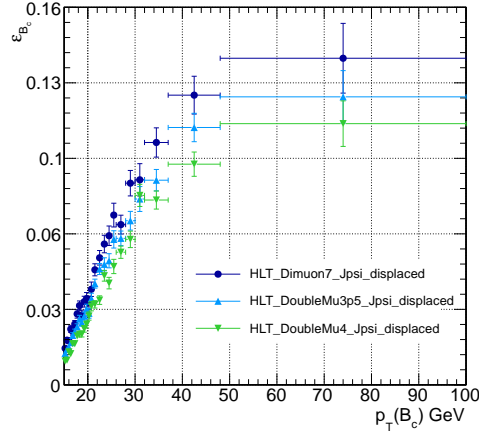

Figure 4.19: $B_c^+ \to J/\psi \pi^+$ reconstruction efficiency as a function of its transverse momentum. The three set of points refer to the reconstruction efficiency for events selected by the three HLT paths used in the analysis.

4.4.3 Measurement of $Y_{3\pi}$ and Y_{B_c}

$B_c^+ \to J/\psi \pi^+ \pi^+ \pi^-$ and $B_c^+ \to J/\psi \pi^+$ data events are weighted by the corresponding efficiency, as measured on the simulation and explained in Sec.4.4.1 and 4.4.2. The corresponding data efficiency-corrected invariant mass distributions are shown in Fig.4.20.

The efficiency corrected yields $Y_{3\pi}$ and Y_{B_c} are obtained by fitting the distributions of Fig.4.20 through an unbinned maximum likelihood estimator. The fit function consists in a Gaussian distribution for the signal and a second-order Chebychev polynomial for the background for both the investigated decay modes. The measurements of $Y_{3\pi}$ and Y_{B_c} are $Y_{3\pi} = 16066 \pm 4715$ and $Y_{B_c} = 6302 \pm 680$, respectively.

The measured ratio is

$$R_{Bc} = 2.55 \pm 0.80, \qquad (4.3)$$

where the error is statistical only.
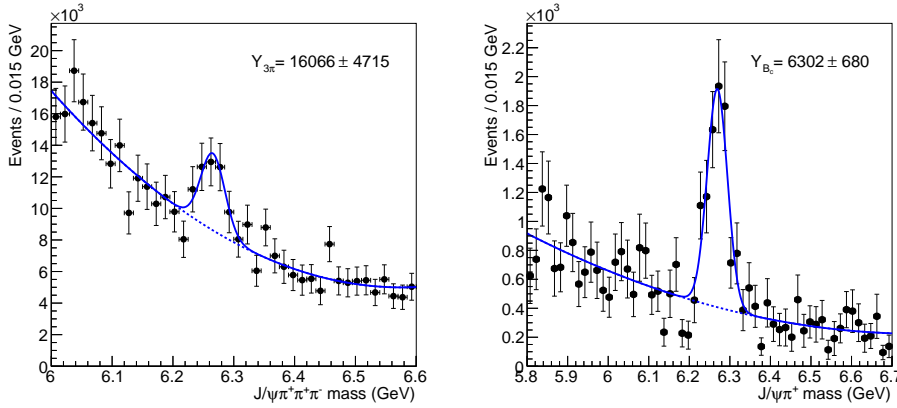
Figure 4.20: Fit to efficiency-corrected invariant mass distribution for $B_c^+ \to J/\psi \pi^+ \pi^+ \pi^-$ (left) and $B_c^+ \to J/\psi \pi^+$ (right).

4.4.4 Systematic uncertainties

In this Section the main sources of systematic uncertainties are presented. Contributions from the investigated sources are summarized in Table 4.3. Tables 4.4 and 4.5 list individual systematics contributions to $Y_{3\pi}$ and Y_{B_c}, respectively.

All contributions, except for the uncertainty on the B_c lifetime which is quoted separately in the result, are added in quadrature, since the hypothesis of

independence is assumed to be reasonable, given the nature of the systematic uncertainties involved and the way they are investigated.

Other possible sources of systematic uncertainty have been studied and turned out to introduce negligible contributions. They are discussed in the last part of this Section.

Systematic source	Percentage	Abs. value
Fit function	9.4	0.24
MC sample size	4.1	0.10
Efficiency fit function	1.0	0.03
Efficiency binning	1.9	0.05
Tracking efficiency	7.8	0.20
Total uncertainty	13.1	0.33
Lifetime	$^{+1.6}_{-0.4}$	$^{+0.04}_{-0.01}$

Table 4.3: Systematic uncertainties on the measurement of R_{B_c}.

Systematic source	Percentage
Fit function	8.1
MC sample size	3.9
Efficiency fit function	1.0
Tracking efficiency	7.8

Table 4.4: Systematic uncertainties on $Y_{3\pi}$.

Systematic source	Percentage
Fit function	4.8
MC sample size	1.1
Efficiency binning	1.9

Table 4.5: Systematic uncertainties on Y_{B_c}.

4.4.4.1 Fit function

Uncertainties from the different signal and background fit functions and fit ranges are evaluated through a "fit variant" approach, which is discussed in App. D. The $J/\psi\pi^+\pi^+\pi^-$ and $J/\psi\pi^+$ efficiency corrected invariant-mass distributions are fit in different mass ranges and with different models. The values of $Y_{3\pi}$ and Y_{B_c} obtained with the different fits are summarized in Tab. 4.6 and 4.7, respectively. The corresponding plots are collected in App. D.1 and D.1. All fit parameters are free to float, except for the widths of the two gaussians and their relative amount, which are fixed to MC values, in fit (g) to the $J/\psi\pi^+$ efficiency-corrected invariant mass.

The systematic uncertainties on $Y_{3\pi}$ and Y_{B_c} are 8.1% and 4.8%, respectively. Adding the two contributions in quadrature, the resulting total systematic uncertainty on R_{B_c} is 9.4%.

	Signal PDF	Bkg PDF	Range (GeV)	$Y_{3\pi}$
a	Gaussian	1st ord. Chebychev pol.	6.13 - 6.4	15471 ± 4690
b	Gaussian	2nd ord. Chebychev pol.	6.10 - 6.4	16890 ± 6673
c	Gaussian	2nd ord. Chebychev pol.	6.1 - 6.505	17853 ± 5951
d	Gaussian	2nd ord. Chebychev pol.	5.8 - 6.7	14745 ± 4115
e	Gaussian	3rd ord. Chebychev pol.	6 - 6.6	17947 ± 5422
f	Gaussian	3rd ord. Chebychev pol.	5.8 - 6.7	15973 ± 4357

Table 4.6: Alternative signal and background models used to fit the $J/\psi\pi^+\pi^+\pi^-$ efficiency-corrected invariant mass distribution. The value of $Y_{3\pi}$ resulting from each fit is shown in the last column of the table.

4.4.4.2 Finite size of the MC sample

As described in Sec. 4.4.1 and 4.4.2, the efficiency correction is entirely derived from the simulation. Therefore, the number of events in the simulation directly affects the accuracy of the efficiency determination. This uncertainty is propagated to the efficiency corrected yields $Y_{3\pi}$ and Y_{B_c} using pseudo-experiments. The following procedure is adopted:

1. N pseudo-efficiency distributions are generated;

2. the analysis is run N-times, each time data are weighted with the toy efficiency and $Y_{3\pi}$ and Y_{B_c} are computed;

	Signal PDF	Bkg PDF	Range (GeV)	Y_{B_c}
a	Gaussian	1st ord. Chebychev pol.	5.8 - 6.7	5773 ± 607
b	Gaussian	1st ord. Chebychev pol.	6.05 - 6.55	6272 ± 658
c	Gaussian	2nd ord. Chebychev pol.	6.05 - 6.55	6419 ± 742
d	Gaussian	2nd ord. Chebychev pol.	5.6 - 6.7	6361 ± 640
e	Gaussian	3rd ord. Chebychev pol.	5.8 - 6.7	6328 ± 673
f	Gaussian	Exponential	5.8 - 6.7	6209 ± 623
g	Double Gaussian	2nd ord. Chebychev pol.	5.8 - 6.7	6790 ± 652

Table 4.7: Alternative signal and background models used to fit the $J/\psi\pi^+$ efficiency-corrected invariant mass distribution. The value of Y_{B_c} resulting from the fit is shown in the last column of the table.

3. the resulting $Y_{3\pi}$ and Y_{B_c} distributions (Fig. 4.21) are fit with a Gaussian, whose width is the systematic uncertainty associated to the finite size of the MC sample.

Two different strategies are followed for the efficiency distribution generation (first step), since the efficiency for $B_c^+ \to J/\psi\pi^+\pi^+\pi^-$ reconstruction is modeled through an analytical function, while that for $B_c^+ \to J/\psi\pi^+$ is measured in transverse momentum bins. In particular, in the $B_c^+ \to J/\psi\pi^+\pi^+\pi^-$ case, 2000 curves of the form as in Eq. 4.2 are generated by varying the parameter values as sampled from a multivariate Gaussian probability density function constructed from the fit covariance matrix. On the other hand, toy $B_c^+ \to J/\psi\pi^+$ efficiencies are generated by randomly varying the efficiency value in each p_T bin within its statistical uncertainty.

The resulting systematic uncertainties on $Y_{3\pi}$ and Y_{B_c} are 3.9% and 1.1%, respectively.

4.4.4.3 Efficiency fit function

The $B_c^+ \to J/\psi\pi^+\pi^+\pi^-$ efficiency has been modeled with a seven-dimensional polynomial function as described in Eq. 4.2. In order to check if the choice of the model introduces a systematic effect in the $Y_{3\pi}$ evaluation, data are weighted according to the binned efficiency distribution obtained from the simulation. The efficiency is measured in six 4-GeV bins for each of the seven invariant-mass combinations and for each of the three trigger paths separately.

Efficiency corrected data are fit and $Y_{3\pi}$ is measured to be 15945 ± 4680. The resulting ratio R_{B_c} is 2.53 ± 0.79. The difference between this result and
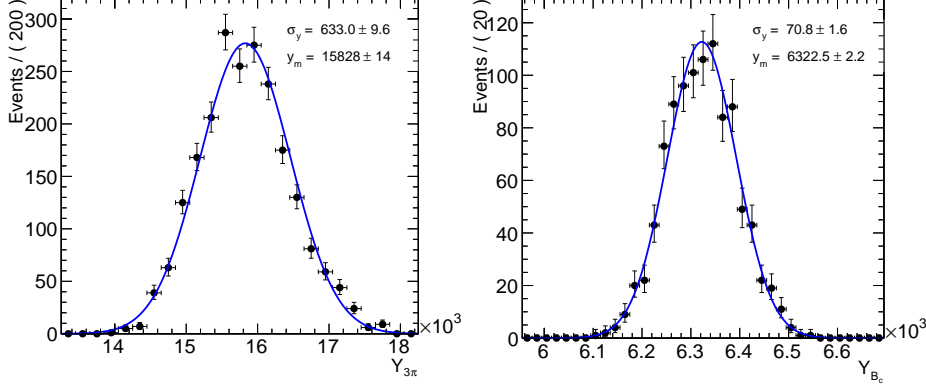
Figure 4.21: Distributions of the efficiency corrected yields $Y_{3\pi}$ (left) and Y_{B_c} (right) returned by the fit to N pseudo-experiments.

the central value quoted in the analysis is assumed as systematic uncertainty (1%).

4.4.4.4 Efficiency binning

In order to estimate the possible bias due to the choice of the p_T binning for the $B_c^+ \rightarrow J/\psi\pi^+$ efficiency description, three different bin choices are tested (binning definitions are summarized in Table 4.8). The efficiency, as evaluated with the different binning choices, is shown in Fig. 4.22.

Data are corrected with the alternative efficiency model and Y_{B_c} is extracted from a fit to efficiency-corrected data. A maximum deviation from the central Y_{B_c} value of 1.9% is found and is taken as systematic uncertainty.

4.4.4.5 Tracking efficiency

The measurement of R_{B_c} exploits final states with different pion track multiplicity. A systematic uncertainty due to the different pion tracking efficiency in data and simulation is therefore considered.

The relative efficiency of pion track reconstruction in data and simulation in CMS is measured in Ref. [105] studying the D^0 decays into four or two charged particles.

In particular, the relative decay rate R between the $D^0 \rightarrow K^-\pi^+\pi^-\pi^+$ and $D^0 \rightarrow K^-\pi^+$ modes is measured on 0.47 nb^{-1} of data collected in 2010. The

Bin	Binning1	Binning2	Binning3
1	15 - 15.6	15-15.3	15 - 15.8
2	15.6 - 16.2	15.3 - 15.6	15.8 - 16.6
3	16.2 - 16.8	15.6 - 15.9	16.6 - 17.4
4	16.8 - 17.4	15.9 - 16.2	17.4 - 18.2
5	17.4 - 18	16.2 - 16.5	18.2 - 19
6	18 - 18.6	16.5 - 16.8	19 - 19.8
7	18.6 - 19.2	16.8 - 17.2	19.8 - 20.6
8	19.2 - 19.8	17.2 - 17.5	20.6 - 21.4
9	19.8 - 20.5	17.5 - 17.8	21.4 - 22.5
10	20.5 - 21.5	17.8 - 18.4	22.5 - 23.5
11	21.5 - 22.5	18.4 - 19	23.5 - 24.5
12	22.5 - 23.5	19 - 19.8	24.5 - 26
13	23.5 - 24.5	19.8 - 20.6	26 - 27.5
14	24.5 - 26	20.6 - 21.4	27.5 - 29
15	26 - 27.5	21.4 - 22.2	29 - 32
16	27.5 - 29.5	22.2 - 23	32 - 36
17	29.5 - 32	23 - 24	36 - 44
18	32 - 36	24 - 25.5	44 - 100
19	36 - 45	25.5 - 26.5	
20	45 - 100	26.5 - 28.5	
21		28.5 - 31	
22		31 - 34	
23		34 - 42	
24		42 - 100	
Y_{B_c}	6186 ± 668	6267 ± 677	6225 ± 672

Table 4.8: Three alternative binning definitions for $B_c^+ \to J/\psi\pi^+$ efficiency evaluation and the resulting Y_{B_c}.
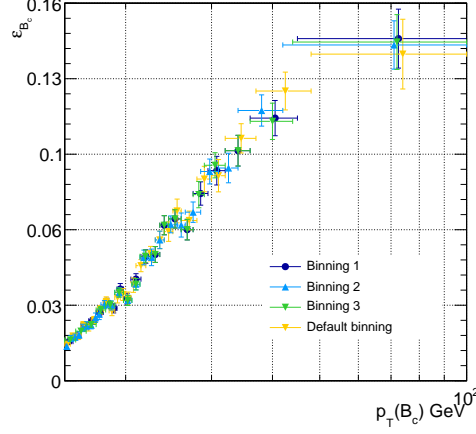
Figure 4.22: $B_c^+ \rightarrow J/\psi \pi^+$ reconstruction efficiency as a function of $p_T(B_c)$. Three alternative binning definitions (blue, azure and green points) are compared with the default option (orange).

measurement of R is compared to the world-average ratio of branching fractions $R(PDG)$ to extract the relative tracking efficiency for pions in data and simulation through the relation:

$$\frac{\epsilon(data)}{\epsilon(MC)} = \sqrt{\frac{R}{R(PDG)}} \qquad (4.4)$$

The ratio of efficiencies is measured to be $\epsilon(data)/\epsilon(MC) = 1.007 \pm 0.034 \pm 0.014 \pm 0.012$, where the first uncertainty is statistical, the second is systematic, and the third is due to the error on $R(PDG)$. The resulting total uncertainty on pion tracking efficiency, obtained by adding all the uncertainties in quadrature, is 3.9%.

The measurement of R_{B_c} presented in this thesis involves final states with one or three pion tracks. The uncertainty on one pion track cancels out in the ratio of the branching fractions. The uncertainty on the reconstruction efficiency for the two remaining pion tracks is accounted for with a 2×3.9% error.

4.4.4.6 B_c **Lifetime uncertainty**

The $B_c^+ \to J/\psi \pi^+ \pi^+ \pi^-$ and $B_c^+ \to J/\psi \pi^+$ reconstruction efficiencies have a dependence on the B_c lifetime. The MC samples have been generated with the B_c lifetime quoted in the PDG [101], which has an uncertainty of about ∼7%. Recently, the LHCb Collaboration published a new, more precise B_c lifetime measurement [75], which is significantly higher than the previous world average.

To determine the systematic uncertainty associated with the uncertainty in the B_c lifetime, the efficiencies are evaluated while changing the B_c lifetime in the simulation to cover the range from the world average minus its one standard deviation uncertainty, to the new LHCb measurement. The left plot of Fig. 4.23 shows the distribution of the simulated B_c^+ proper decay time in the simulation. The efficiency as evaluated with different simulated values for τ_{B_c} is shown in the right plot of Fig. 4.23 and in Fig. 4.24 for the $B_c^+ \to J/\psi \pi^+$ and $B_c^+ \to J/\psi \pi^+ \pi^+ \pi^-$ decay modes, respectively.

The resulting variation in the R_{B_c} ratio is asymmetric and is quoted separately in the result and is +1.6%, -0.4%.
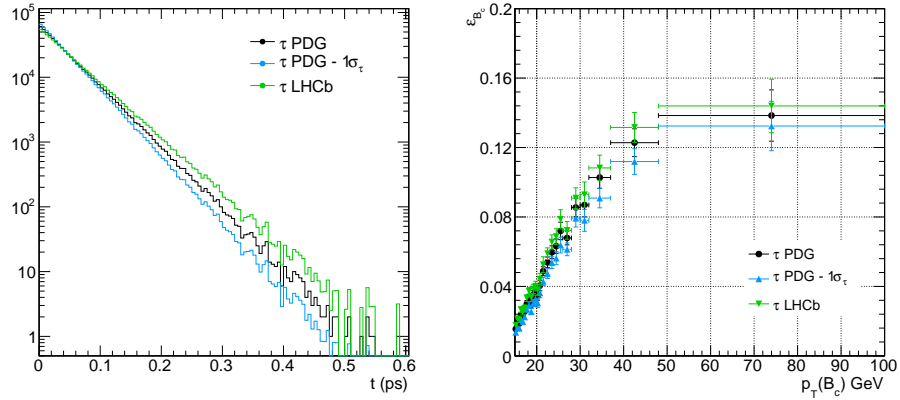
Figure 4.23: Left plot: Distribution of the simulated B_c^+ proper decay time (t) at generator level (black histogram). The azure and green histograms show the distribution of t when τ_{B_c} is changed to the PDG value minus its one standard deviation or to the value from LHCb measurement, respectively.
Right plot: $B_c^+ \to J/\psi \pi^+$ reconstruction efficiency with the two alternative values of the B_c lifetime.
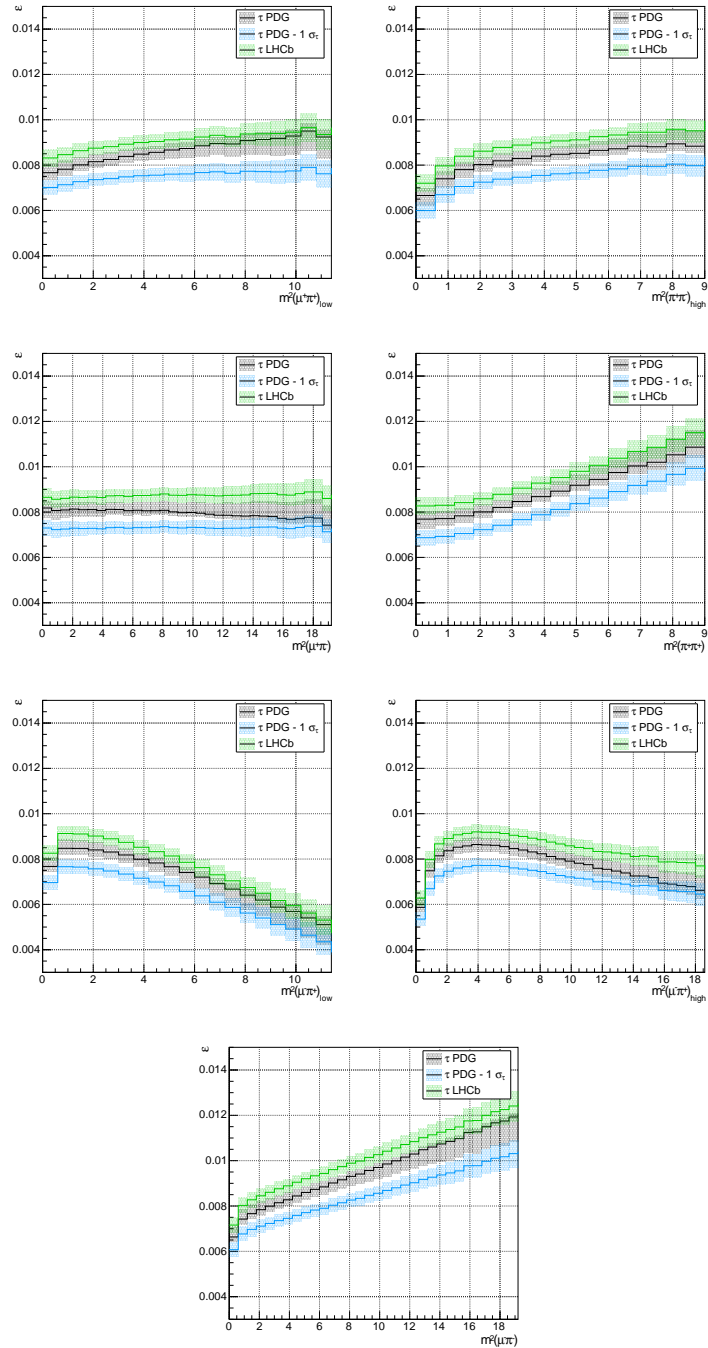
Figure 4.24: Projections on the two-body mass combinations of the reconstruction efficiency resulting from the seven-dimensional fit to the simulation when the MC B_c lifetime value is changed from the PDG value (black) to the PDG value minus one standard deviation (azure) and to the LHCb measurement (green).

4.4.4.7 Split samples

Possible systematic uncertainties introduced by different pileup conditions and analysis selections are investigated by dividing the data and evaluating the statistical consistency [101] of the measurement of R_{B_c} in the independent samples.

Data and simulated samples are split according to the number of primary vertices per event and main analysis variables, and the measurement of R_{B_c} is performed in each sub-sample. The split of the samples is designed in order to have comparable statistics in the two independent regions.

Results for the measurement of R_{B_c} in each sample are summarized in Table 4.9. The statistical consistency is verified and the possible systematic uncertainty is obtained following the procedure described in App.E. The resulting systematic contributions are found to be insignificant.

These studies have been carried out fixing the signal width parameter in the fit to data to that inferred from the simulation in order to have more accurate fit results. It has also been verified that, by leaving all the parameters free when possible, no systematic uncertainty was present.

Variable	Split	$Y_{3\pi}$	Y_{B_c}	R_{B_c}	χ^2	σ_{sys}
Pileup	$N_{vtx} < 7$	7820 ± 2380	2127 ± 325	3.68 ± 1.25	1.43	0
	$N_{vtx} \geq 7$	7892 ± 2806	4043 ± 501	1.95 ± 0.73		
$y(B_c)$	$|y| \leq 0.6$	12286 ± 3754	5212 ± 695	2.36 ± 0.79	0.1	0
	$0.6 < |y| < 1.6$	17781 ± 6046	6431 ± 789	2.76 ± 1.00		
$p_T(B_c)$	$15 < p_T \leq 28$	10491 ± 3854	6229 ± 673	1.68 ± 0.64	1.61	0
	$p_T > 28$	1413 ± 338	440 ± 91	3.21 ± 1.02		
$L_{J/\psi}/\sigma_{L_{J/\psi}}$	$5 \leq L_{J/\psi}/\sigma_{L_{J/\psi}} \leq 12$	9696 ± 4458	5897 ± 670	1.64 ± 0.80	0.91	0
	$L_{J/\psi}/\sigma_{L_{J/\psi}} > 12$	20448 ± 3916	7768 ± 1254	2.63 ± 0.66		

Table 4.9: Results of the measurement of R_{B_c} in each data sub-sample, as defined in the second column. The statistical consistency of the measurements (χ^2 with N-1 degrees of freedom) and the resulting systematic uncertainty are reported in the last two columns of the table.

4.4.4.8 Candidate selection

When multiple B_c candidates are found in a single collision event, the candidate with the highest p_T is selected. Since the number of candidates depends on the final state multiplicity, the average number of candidates per event is higher in the $B_c^+ \to J/\psi \pi^+ \pi^+ \pi^-$ channel with respect to the $B_c^+ \to J/\psi \pi^+$ one. In fact, the average number of candidates per event in the whole invariant mass spectrum is 2.7 for the three-body decay modes and ~ 5 for the five-body B_c decay.

Choosing one candidate per event allows to significantly reduce the combinatorial background, especially in the $B_c^+ \to J/\psi \pi^+ \pi^+ \pi^-$ mode. In the three-body decays, indeed, the amount of signal and background does not significantly change when retaining all the candidates of the event.

In order to evaluate a possible systematic uncertainty introduced by selection of the highest-p_T candidate (*arbitration*), the $B_c^+ \to J/\psi \pi^+ \pi^+ \pi^-$ analysis is performed keeping all the B_c^+ candidates. The efficiency of this arbitration is measured on the simulation to be $\varepsilon_{arb} = 0.91\varepsilon_{na}$, where ε_{arb} and ε_{na} are the overall reconstruction efficiencies when the arbitration strategy is adopted or all the B_c candidates are kept, respectively.

From the fit to the $J/\psi \pi^+ \pi^+ \pi^-$ invariant mass distribution resulting from the analysis of the full data sample retaining all the candidates in each event, the $B_c^+ \to J/\psi \pi^+ \pi^+ \pi^-$ signal yield is 117 ± 47.

Since the arbitrated sample Y is fully contained in the non-arbitrated sample X, one can write X = Y + Z, where Y and Z are disjoint samples. It is expected that, if there are no systematic effects:

$$\frac{N_X}{\varepsilon_X} = \frac{N_Y}{\varepsilon_Y} + \frac{N_Z}{\varepsilon_Z} \tag{4.5}$$

where N_K is the yield obtained from the fit to the mass spectrum from sample K and ε_K is the efficiency for sample K.
From Eq.4.5, we obtain that:

$$N_X \cdot \frac{\varepsilon_Y}{\varepsilon_X} = N_Y + N_Z \cdot \frac{\varepsilon_Y}{\varepsilon_Z} \tag{4.6}$$

In order to measure possible systematic effects, the relation in Eq.4.6 can be checked through a simultaneous fit to the invariant mass spectra from the samples Y and Z, having reweighted the signal yield N_Z with the ratio of the efficiencies for samples Y and Z.
To this extent, a simultaneous fit to the mass spectra from the samples Y and Z is performed with the following model:

$$f_1 = N_Y \cdot Gauss(m_{Bc}, \sigma_{m_{Bc}}) + B_Y \cdot Pol(c_1, c_2) \tag{4.7}$$

for the fit to sample Y, and

$$f_2 = \frac{\varepsilon_Y}{\varepsilon_Z} \cdot N_Y \cdot Gauss(m_{Bc}, \sigma_{m_{Bc}}) + B_Z \cdot Pol(c_1', c_2') \tag{4.8}$$

for the fit to sample Z. ε_Y and ε_Z are the efficiencies as evaluated for the samples Y and Z. The backgrounds functions $Pol(c_1, c_2)$ and $Pol(c_1', c_2')$ are two independent second-order Chebychev polynomials. All the parameters are free to float and the efficiency ratio has a gaussian constraint with mean and error provided by the simulation.

The resulting value is $N_Y = 91.8 \pm 26$ (Fig.4.25), to be compared with the quoted yield equal to 92 ± 27. Since the difference between these values is $\sim 2 \cdot 10^{-3}$, we conclude that the possible systematics associated to the arbitration strategy is negligible.
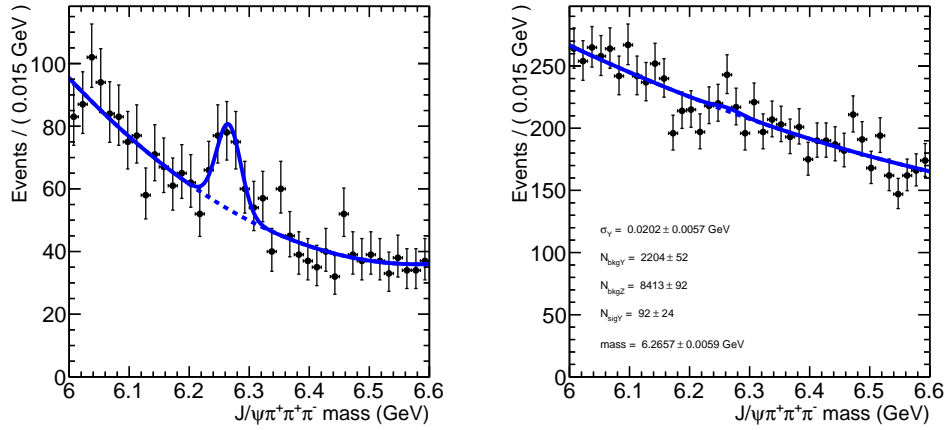

Figure 4.25: Results of the simultaneous fit to the disjoint samples Y (left) and Z (right), as desribed in the text.

4.4.5 Result

The resulting ratio of the B_c^+ hadronic branching fractions, including all uncertainties, is

$$R_{B_c} = 2.55 \pm 0.80 \, (\text{stat}) \pm 0.33 \, (\text{syst}) \, {}^{+0.04}_{-0.01} \, (\tau_{B_c}), \qquad (4.9)$$

where the systematic uncertainty due to the experimental uncertainty on the B_c lifetime τ_{B_c} is quoted separately.

This result is consistent with the theoretical predictions discussed in Section 2.3.2.1, which expect values ranging from 1.5 to 2.3, depending on the chosen set of B_c meson form factors.

The measurement in Eq.4.9 is in good agreement with the measurement of R_{B_c} from the LHCb experiment [66]:

$$R_{B_c} = 2.41 \pm 0.30 \, (\text{stat}) \pm 0.33 \, (\text{syst}), \qquad (4.10)$$

which uses a phenomenological model by Berezhnoy, Likhoded and Luchinsky (BLL model) [106, 51] to simulate $B_c^+ \to J/\psi \pi^+ \pi^+ \pi^-$ decays and measure the corresponding reconstruction efficiency. In this model the W^{+*} decays via the exchange of virtual $a_1(1260)$ and $\rho^0(770)$ resonances and axial-vector form-factors are implemented for the $B_c^+ \to J/\psi W^{*+}$ transition. The model-dependence of the efficiency has to be taken into account with an additional systematic uncertainty ($\sim 9\%$), evaluated using alternative phase-space models to simulate the five-body decay.

On the contrary, the result presented in this thesis provides a measurement of R_{B_c} independent of the decay-model assumed in the simulation of the $B_c^+ \to J/\psi \pi^+ \pi^+ \pi^-$ channel.

4.5   Measurement of $R_{c/u}$

The ratio $R_{c/u}$ of the production cross sections times branching fractions is obtained from the relation

$$R_{c/u} = \frac{\sigma(B_c^+) \times B(B_c^+ \to J/\psi\pi^+)}{\sigma(B^+) \times B(B^+ \to J/\psi K^+)} = \frac{Y_{B_c}}{Y_B} \qquad (4.11)$$

where Y_{B_c} and Y_B are the signal yields obtained from the efficiency corrected mass distributions for the $B_c^+ \to J/\psi\pi^+$ and $B^+ \to J/\psi K^+$ channels, respectively. The ratio $R_{c/u}$ is measured in the kinematic region $p_T > 15$ GeV and $|y| < 1.6$.

The measurement of $B_c^+ \to J/\psi\pi^+$ efficiency and efficiency-corrected yield Y_{B_c} has already been described in Sec. 4.4. The following Sections describe in details the treatment of the $B^+ \to J/\psi K^+$ channel.

4.5.1   Efficiency measurement for $B^+ \to J/\psi K^+$

The $B^+ \to J/\psi K^+$ reconstruction efficiency is measured as a function of the B^+ transverse momentum on the corresponding MC simulation, as done in the $B_c^+ \to J/\psi\pi^+$ channel. The efficiency is computed in 19 p_T-bins, whose widths are determined by the available size of the two body $B^+ \to J/\psi K^+$ MC sample. The number of bins is lower than that of the $B_c^+ \to J/\psi\pi^+$ decay, due to the smaller statistics of the B^+ simulation.

The efficiency ε in the ith bin is evaluated as $\varepsilon_i = N_i^{reco}/N_i^{GEN}$ where N_i^{reco} is the number of reconstructed events in the given bin and N_i^{GEN} is the number of generated B^+ events in the same p_T bin and within the considered rapidity region $|y(B^+)| < 1.6$.

The efficiency behavior as a function of $p_T(B^+)$ is shown in Fig. 4.26. The three set of points correspond to the reconstruction efficiency measured with the three trigger paths used in the analysis.
The reconstruction efficiency is lower when events are selected by the HLT_DoubleMu3p5_Jpsi_displaced and HLT_DoubleMu4_Jpsi_displaced paths, due to their tighter requirements on muon transverse momentum and dimuon vertex probability. The overall efficiency loss with respect to the loosest trigger path is 18 and 32%, respectively.
The overall B^+ selection efficiency, integrated over p_T and averaged over the three trigger paths according to the corresponding collected integrated luminosity in data, is $(3.86 \pm 0.08) \cdot 10^{-2}$.
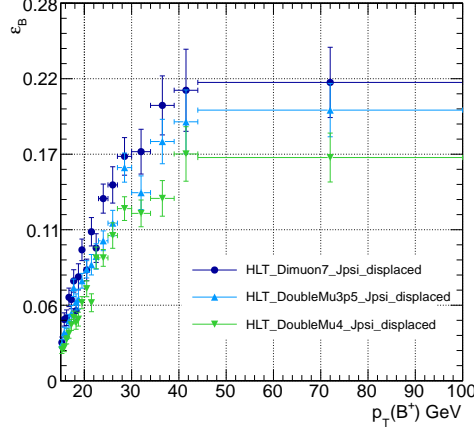
Figure 4.26: $B^+ \to J/\psi K^+$ reconstruction efficiency as a function of the B^+ transverse momentum. The three set of points correspond to the reconstruction efficiency measured with the three trigger paths used in the analysis.

4.5.2 Measurement of Y_B

Data are then corrected event-by-event according to the B^+ meson transverse momentum and the efficiency determined from the simulation. The $J/\psi K^+$ efficiency-corrected invariant mass distribution is shown in Fig. 4.27. The value of Y_B is extracted through an unbinned maximum likelihood fit to the efficiency-corrected mass distribution of Fig. 4.27, and is $Y_B = 1320256 \pm 5140$.

The fit function consists in the sum of two Gaussian distributions with a common mean for the signal and a second order Chebychev polynomial for the background. Contributions from partially reconstructed B^0 and B^+ decays are modeled by two additional Gaussian distributions, as explained in Sec.4.3.3.

The uncertainty on Y_B due to the statistical uncertainty on the efficiency is accounted for in the systematic uncertainty (see Sec.4.5.3.2).

The resulting ratio $R_{c/u}$ is

$$R_{c/u} = (0.48 \pm 0.05) \cdot 10^{-2}, \tag{4.12}$$

where the error is statistical only.
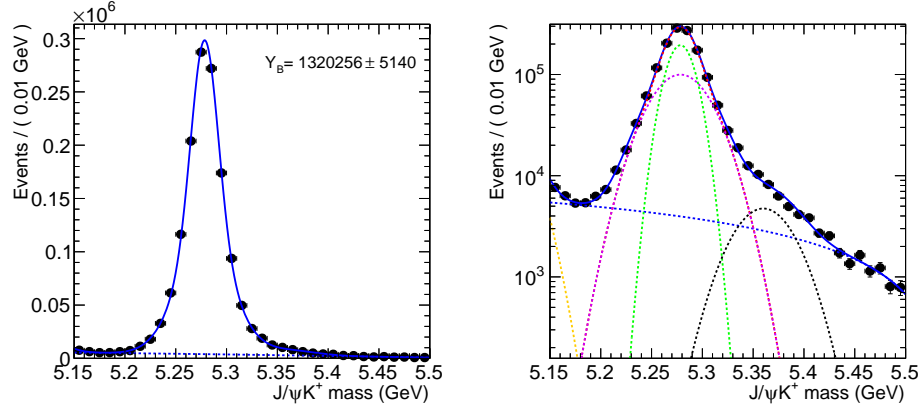
Figure 4.27: Efficiency corrected $J/\psi K^+$ invariant mass distributions in linear (left) and semi-log (right) scale.

4.5.3   Systematic uncertainties

This Section describes the main contributions to the systematic uncertainty on the measurement of $R_{c/u}$.

The same sources of systematic uncertainties considered in Section 4.4.4 are evaluated and their contributions are summarized in Table 4.10.
Table 4.11 lists individual contributions to Y_B; systematic uncertainties on Y_{B_c} have already been described in Sec. 4.4.4 and summarized in Tab. 4.5.

All contributions, except for the uncertainty on the B_c lifetime which is quoted separately in the result, are added in quadrature, and yield a total systematic uncertainty of 6.5% in the ratio.

Systematic source	Percentage	Abs. value (10^{-2})
Fit function	5.3	0.03
MC sample	2.1	0.01
Efficiency binning	3.1	0.01
Total uncertainty	6.5	0.03
B_c lifetime	10.4	0.05

Table 4.10: Systematic uncertainties on the measurement of $R_{c/u}$.

Systematic source	Percentage
Fit function	2.2
MC sample size	1.8
Efficiency binning	2.4

Table 4.11: Systematic uncertainties on Y_B.

4.5.3.1 Fit function

Uncertainties from the signal and background fit functions are evaluated through a "fit variant" approach, as done in Sec. 4.4.4.1.

The efficiency corrected $J/\psi K^+$ invariant mass distribution is fit with different models for the signal and combinatorial background. Partially reconstructed B^+ decays have also been described with alternative functions, while the background due to B^0 decays is always fit with a Gaussian distribution. The fit range is varied to include or exclude such reflections. Details are collected in Table 4.12 and corresponding plots can be found in App. D.1.

The resulting systematic uncertainty on Y_B is 2.2%. Adding in quadrature the uncertainties on Y_{B_c} (4.5%) and Y_B, the resulting systematic uncertainty on $R_{c/u}$ is 5.3%.

Signal PDF	Bkg PDF	$B^+ \to J/\psi \pi^+$ pdf	Range (GeV)	Y_B
Crystal Ball	2nd ord. Ch. pol	Crystal Ball	5.15-5.5	1252794 ± 7601
Crystal Ball	2nd ord. Ch. pol	Landau	5.15-5.5	1307042 ± 5384
Crystal Ball	2nd ord. Ch. pol	Gaussian	5.15-5.5	1257149 ± 5230
Double Gauss.	2nd ord. Ch. pol	Crystal Ball	5.15-5.5	1328524 ± 5738
Double Gauss.	2nd ord. Ch. pol	Landau	5.15-5.5	1319095 ± 4880
Double Gauss.	3rd ord. Ch. pol	Gaussian	5.15-5.5	1295249 ± 8819
Double Gauss.	2nd ord. Ch. pol	Gaussian	5.05-5.6	1311804 ± 4654
Double Gauss.	2nd ord. Ch. pol	Gaussian	5.18-5.4	1324893 ± 5217

Table 4.12: Alternative signal and background models used to fit the $J/\psi K^+$ efficiency-corrected invariant mass distribution. The value of Y_B resulting from the corresponding fit is reported in the last column of the table.

4.5.3.2   Finite size of the MC sample

As described in Sec. 4.5.1, the $B^+ \to J/\psi K^+$ reconstruction efficiency is entirely derived from the simulation. Therefore, the number of events in the simulation affects the accuracy of the efficiency determination.

Pseudo-experiments are used to propagate the statistical uncertainty of the MC sample on the efficiency corrected yield Y_B. The procedure, that was already described in Sec. 4.4.4.2, starts from generating 1000 toy efficiency distributions by randomly varying the efficiency value in each p_T bin within its statistical error. Data are then weighted with the generated pseudo-efficiencies and Y_B is extracted through a fit to the efficiency-corrected invariant mass distributions. The resulting Y_B distribution is finally fit with a gaussian (Fig. 4.28), whose width is taken as systematic uncertainty (1.8%).

The total systematic uncertainty on $R_{c/u}$ due to the finite size of the MC sample is obtained by adding in quadrature the uncertainty on Y_B and Y_{B_c} (as evaluated in Sec. 4.4.4.2). This result in an uncertainty of 2.1%.

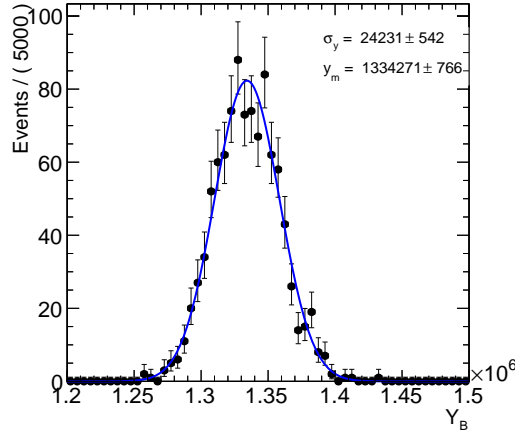**Figure 4.28:** Distribution of the efficiency corrected yield Y_B obtained by the fit to pseudo-experiments.

4.5.3.3   Efficiency binning

In order to estimate a possible bias due to the choice of the p_T binning for the $B^+ \to J/\psi K^+$ efficiency description, three different bin choices have been tested (binning definitions are summarized in Table 4.13) to measure the efficiency,

as shown in Fig.4.29.

Data have been corrected with the alternative efficiency models and Y_B is extracted through a fit to the efficiency-corrected data. A maximum deviation from the central value of Y_B of 2.4% is found.

Combining this uncertainty with that on Y_{B_c}, as measured in Sec. 4.4.4.4, the total systematic uncertainty on $R_{c/u}$ results to be 3.1%.
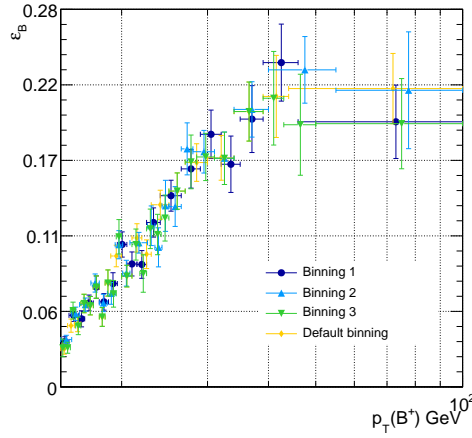
Figure 4.29: $B^+ \rightarrow J/\psi K^+$ reconstruction efficiency as a function of $p_T(B^+)$. Three alternative binning definitions (blue, azure and green points) are compared with the default option (orange points).

4.5.3.4 B_c **lifetime uncertainty**

As already discussed in Sec. 4.4.4.6, the $B_c^+ \rightarrow J/\psi\pi^+$ reconstruction efficiency depends on the B_c lifetime. The systematic uncertainty on $R_{c/u}$ from the B_c lifetime uncertainty is estimated by varying the B_c lifetime in the simulation from the world average value minus its one standard deviation uncertainty, to the new LHCb measurement [75]. The effect on the $B_c^+ \rightarrow J/\psi\pi^+$ reconstruction efficiency was shown in Fig. 4.23. The resulting variation in the $R_{c/u}$ ratio is 10.4%.

Since the B^+ lifetime is known with a much better accuracy, the propagation of its uncertainty to the $R_{c/u}$ ratio systematic uncertainty is neglected. The uncertainty from the B_c lifetime is quoted separately in the final result.

Bin	Binning1	Binning2	Binning3
1	15 - 15.6	15 - 15.8	15-15.3
2	15.6 - 16.3	15.8 - 16.4	15.3 - 15.7
3	16.3 - 16.8	16.4 - 17.3	15.7 - 16.1
4	16.8 - 17.5	17.3 - 18	16.1 - 16.5
5	17.5 - 18	18 - 18.7	16.5 - 17
6	18 - 18.8	18.7 - 19.4	17 - 17.5
7	18.8 - 19.6	19,4 - 20.1	17.5 - 18
8	19.6 - 20.5	20.1 - 20.8	18 - 18.5
9	20.5 - 21.5	20.8 - 22.6	18.5 - 19
10	21.5 - 22.5	22.6 - 23.4	19 - 19.5
11	22.5 - 24	23.4 - 24.2	19.5 - 20
12	24 - 26.5	24.2 - 25	20 - 21
13	26.5 - 29	25 - 26.5	21 - 21.8
14	29 - 32	26.5 - 28	21.8 - 22.5
15	32 - 35	28 - 31	22.5 - 23.3
16	35 - 39	31 - 34	23.3 - 24.1
17	39 - 46	34 - 40	24.1 - 25
18	46 - 100	40 - 55	25 - 27
19		55 - 100	27 - 28.5
20			28.5 - 31
21			31 - 34
22			34 - 39
23			39 - 43
24			43 - 50
25			50 - 100
Y_B	1288844 ± 5017	1292228 ± 5031	1344265 ± 5233

Table 4.13: Three alternative binning definitions for the $B^+ \to J/\psi K^+$ efficiency evaluation and the resulting Y_B.

4.5.3.5 Split samples

Possible systematic uncertainties introduced by different trigger and pileup conditions and analysis selections have been investigated by dividing the data and evaluating the statistical consistency [101] of the measurement of $R_{c/u}$ in the independent samples.

Data and simulated samples are split according to the trigger path, number of primary vertices per event and main analysis variables, and the measurement of $R_{c/u}$ is performed in each sub-sample. The split of the samples is designed to have a comparable statistics in each independent region.

The definition of the samples and corresponding measurements of $R_{c/u}$ are summarized in Table 4.14; the statistical consistency of the measurements in the sub-samples is also reported. The resulting systematic contributions, evaluated following the procedure described in App. E, are found to be insignificant.

Variable	Split	Y_{B_c}	Y_B	$R_{c/u}$ (10^{-2})	χ^2	σ_{sys}
Trigger	Dimuon7	1366 ± 238	282874 ± 2284	0.48 ± 0.08		
	DoubleMu3p5	1100 ± 314	246800 ± 2088	0.45 ± 0.13	0.25	0
	DoubleMu4	4088 ± 632	791146 ± 4134	0.52 ± 0.08		
Pileup	$N_{vtx} < 7$	2127 ± 325	424253 ± 1277	0.50 ± 0.08	0.14	0
	$N_{vtx} \geq 7$	4043 ± 501	751218 ± 3685	0.54 ± 0.07		
$L_{J/\psi}/\sigma_{L_{J/\psi}}$	$5 \leq L_{J/\psi}/\sigma_{L_{J/\psi}} \leq 10$	5487 ± 776	1223514 ± 10375	0.45 ± 0.06	0.64	0
	$L_{J/\psi}/\sigma_{L_{J/\psi}} > 10$	6166 ± 894	1159447 ± 5075	0.53 ± 0.08		

Table 4.14: Results of the measurement of $R_{c/u}$ in different data samples. The statistical consistency of the measurements (χ^2 with N-1 degrees of freedom) and the resulting systematic uncertainty are reported in the last two columns.

4.5.3.6 Fragmentation function

Uncertainties in the production of B hadrons from the fragmentation of a b-quark can affect the efficiency estimate.

A possible systematic uncertainty is computed as the difference between the default result and that obtained with an alternative hadronization model available in the PYTHIA simulation, the Peterson [107] functions.

A $B^+ \to J/\psi K^+$ sample is generated with the Peterson fragmentation function and is used to compute the $B^+ \to J/\psi K^+$ reconstruction efficiency. Fig. 4.30 shows the $B^+ \to J/\psi K^+$ reconstruction efficiency as a function of $p_T(B^+)$ for the standard simulation (black dots) and for the alternative simulation via the Peterson function (blue dots).

Data are corrected with the "new" efficiency and the efficiency-corrected invariant mass distribution is shown in Fig. 4.31. The difference in the measurement of Y_B when using the Peterson function in the MC sample generation is tiny, about 0.2%. Indeed, the $p_T(B^+) > 15$ GeV cut applied in the analysis selects a kinematic region where the two production models do not reveal important differences; the effect on the results of this analysis is negligible.

Since the B_c momentum distribution is already embedded in the LHE file produced by the BCVEGPY package, it is not possible to generate a B_c^+ sample with a different B_c^+ momentum spectrum using PYTHIA hadronizer. On the other hand, it is verified that the impact of the different fragmentation function on the B^+ momentum spectrum above 15 GeV is very small. Therefore, we assume that the effect on R_{B_c} of using a different fragmentation function for the B_c meson simulation is negligible.
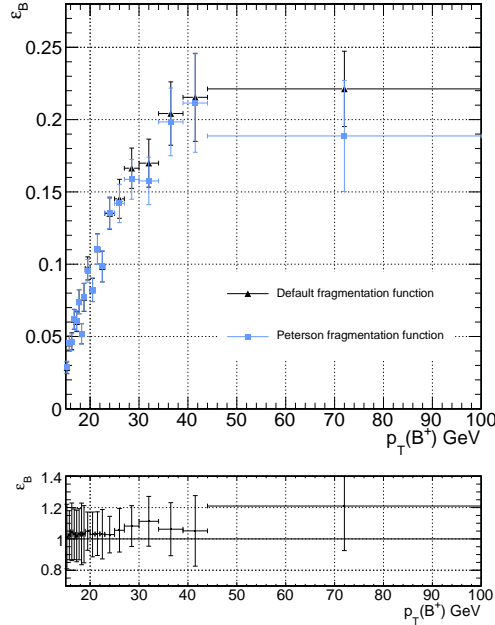

Figure 4.30: $B^+ \rightarrow J/\psi K^+$ reconstruction efficiency versus $p_T(B^+)$ for the standard MC (black dots) and for the alternative simulation via the Peterson function (green dots). Their ratio is shown in the bottom panel.
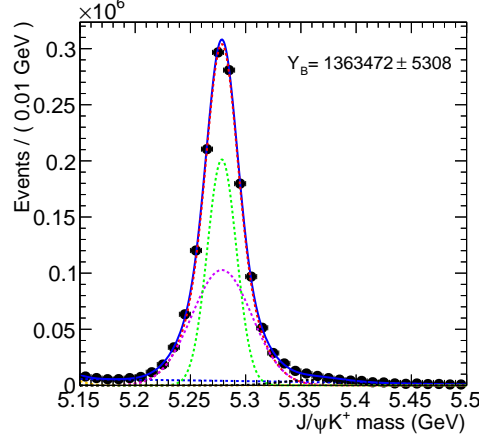
Figure 4.31: Efficiency corrected $J/\psi K^+$ invariant mass distribution. The $B^+ \rightarrow J/\psi K^+$ reconstruction efficiency is measured on a simulated sample generated via the Peterson fragmentation function.

4.5.4 Result

The resulting ratio $R_{c/u}$, including all uncertainties, is

$$R_{c/u} = [0.48 \pm 0.05 \,(\text{stat}) \pm 0.03 \,(\text{syst}) \pm 0.05 \,(\tau_{B_c})]\%. \qquad (4.13)$$

This measurement describe the ratio of the cross sections times branching fractions for $B_c^+ \rightarrow J/\psi \pi^+$ and $B^+ \rightarrow J/\psi K^+$ when meson have $p_T > 15$ GeV and live in the central rapidity region $|y| < 1.6$. A similar measurement from LHCb in the kinematic region $p_T > 4$ GeV, $2.5 < \eta < 4.5$ gives [76]:

$$[0.68 \pm 0.10 \,(\text{stat}) \pm 0.03 \,(\text{syst}) \pm 0.05 \,(\tau_{B_c})]\%. \qquad (4.14)$$

The two measurements, performed in different kinematic regions, are expected to vary because of the softer p_T distribution of the B_c with respect to that of the B^+. This implies a lower value of the $R_{c/u}$ ratio at higher p_T. The measurements are consistent with this expectation.

Measurements of the production cross section times branching fraction for $B_c^+ \rightarrow J/\psi l^+ \nu_l$ relative to that for $B^+ \rightarrow J/\psi K^+$ are also available from the CDF experiment [59] in the kinematic region $p_T > 4$ GeV and $|y| < 1$. With the present B_c (p_T, y) coverage, these experimental results can give guidance to improve the theoretical calculations, which are still affected by large uncertainties, and constrain the various B_c production models.

Chapter 5

Conclusions

The B_c meson offers a unique insight into the dynamics of the heavy quarks and measurements of its properties provide a new testing ground for predictions in the context of effective models inspired by quantum chromodynamics.

The physics of the B_c meson has entered a new era with the advent of the CERN LHC. Thanks to the unprecedented energy and instantaneous luminosity provided by the LHC, the available B_c statistics is much higher than in previous experiments, allowing for a precise investigation of its properties. The CMS experiment is particularly suited to study the production and decay features of B_c mesons through the decay modes with a J/ψ meson in the final state.

In this thesis we presented the measurement of the relative branching fractions of the two hadronic decays $B_c^+ \rightarrow J/\psi \pi^+ \pi^+ \pi^-$ and $B_c^+ \rightarrow J/\psi \pi^+$ performed with the CMS experiment. The measurement has been carried out on the data sample collected by CMS in 2011 at 7 TeV, which corresponds to 5.1 fb^{-1}.

The signal selection has been optimized using the simulated signal and the real background from data. Efficiencies have been evaluated on the MC simulation taking into account the event kinematic. The efficiency-corrected data are fit with an unbinned maximum likelihood estimator. Systematic effects due to analysis strategy and detector efficiency are measured to be $\sim 13\%$.

The measurement of the ratio R_{B_c} is

$$R_{B_c} = 2.55 \pm 0.80 \text{ (stat)} \pm 0.33 \text{ (syst)} {}^{+0.04}_{-0.01} (\tau_{B_c}), \qquad (5.1)$$

which is in good agreement with theoretical expectations and the result [66] from the LHCb experiment.

A measurement of the ratio $R_{c/u}$ of the cross sections times branching fractions for $B_c^+ \to J/\psi\pi^+$ and $B^+ \to J/\psi K^+$ is also presented for B_c and B^+ mesons with $p_T > 15$ GeV and in the central rapidity region $|y| < 1.6$.

The measurement is affected by a systematic uncertainty of $\sim 6\%$ due to analysis procedure and object reconstruction. A further systematic effect ($\sim 10\%$) is introduced by the experimental uncertainty on the B_c lifetime.

The measurement

$$R_{c/u} = [0.48 \pm 0.05 \text{ (stat)} \pm 0.03 \text{ (syst)} \pm 0.05 \ (\tau_{B_c})]\%, \qquad (5.2)$$

is complementary to the results provided by the LHCb [76] and CDF [59] experiments in different kinematic regions and decay modes.

The results presented in this thesis enrich the current B_c experimental scenario, and have opened the way for further studies of B_c properties in the CMS experiment.

Appendix

A   Selection cuts optimization procedure

In this Section the plots related to the selection cut optimization procedure explained in Sec. 4.3.1 and 4.3.2 are collected.

In particular, Fig.A.1 shows the trend of the figure of merit $S/\sqrt{S+B}$ for the $B_c^+ \to J/\psi\pi^+\pi^+\pi^-$ signal as a function of the selection cut value. As explained in Chapter Sec.4.3.1, S is the signal yield obtained from a Gaussian fit to the MC reconstructed events, properly rescaled to the data integrated luminosity, and B is the amount of background extrapolated from $J/\psi\pi^+\pi^+\pi^-$ invariant mass sidebands in the data.

Similarly, Fig. A.2 shows the behavior of the $S/\sqrt{S+B}$ figure of merit for the $B_c^+ \to J/\psi\pi^+$ decay mode.
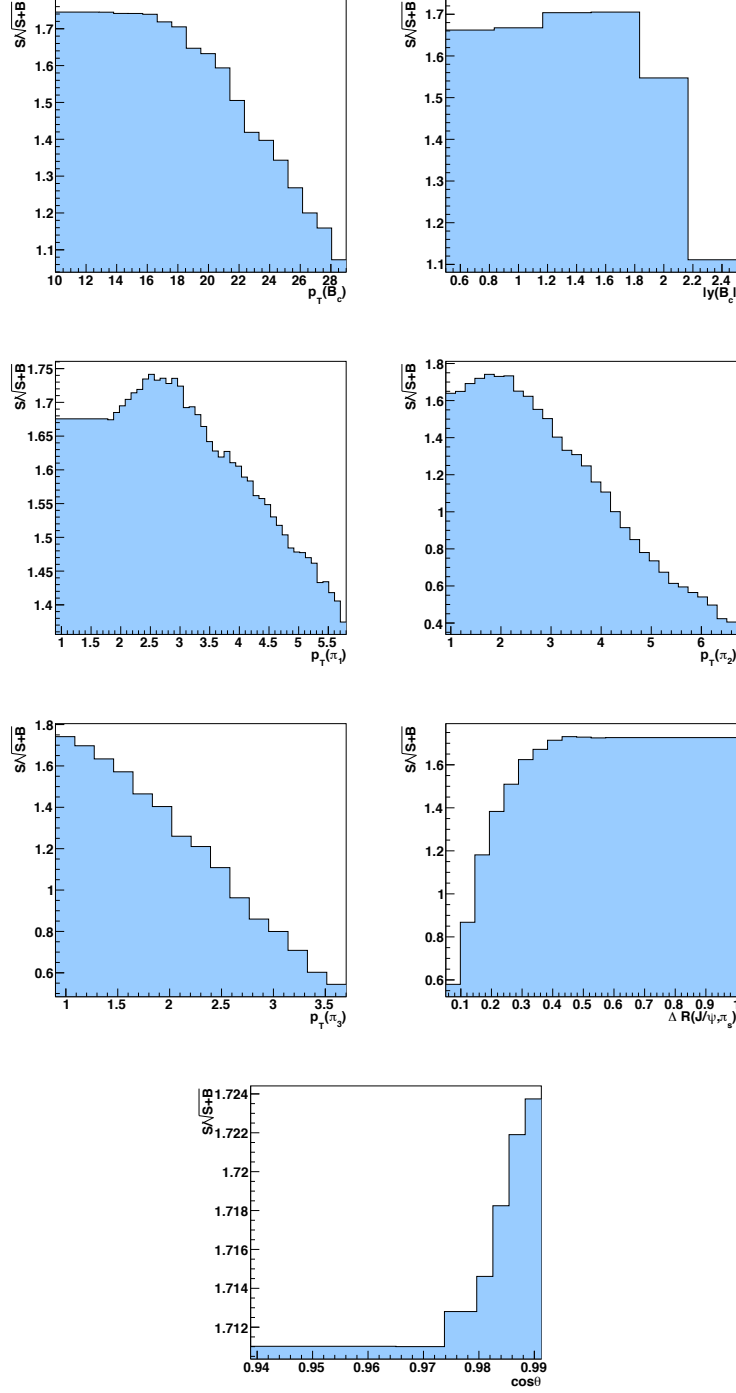
Figure A.1: Trend of the $S/\sqrt{(S+B)}$ figure of merit as a function of the selection cut value, namely $p_T(B_c)$, $y(B_c)$, $p_T(\pi_1)$, $p_T(\pi_2)$ and $p_T(\pi_3)$, $\Delta R(J/\psi, \pi_s)$ and $cos\theta$, for the $B_c^+ \to J/\psi \pi^+ \pi^+ \pi^-$ decay mode

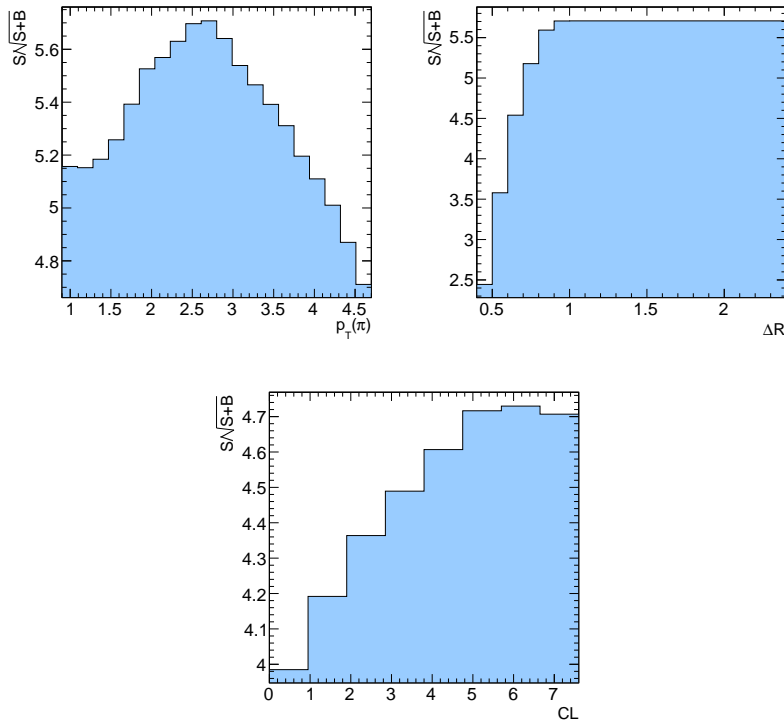**Figure A.2:** Trend of the $S/\sqrt{(S+B)}$ figure of merit as a function of the selection cut value, namely pion p_T, $\Delta R(J/\psi, \pi)$ and vertex probability, for the $B_c^+ \to J/\psi \pi^+$ decay mode.

B   MonteCarlo truth matching

The measurement of the reconstruction efficiency on the simulation relies on the capability of associating the reconstructed events to the corresponding generated events. This procedure (*truth-matching*) is usually performed requiring the reconstructed and generated tracks to be within a cone $\Delta R \equiv \sqrt{(\Delta\eta)^2 + (\Delta\phi)^2}$, where $\Delta\eta$ and $\Delta\phi$ are the differences between the reconstructed candidate pseudorapidity and azimuthal angles from the true values. The optimal cone sizes ΔR for matching pion and muon candidates to signal simulation events are chosen in such a way that the total number of true signal events in the signal region failing the matching is equal to the total number of signal events outside of the signal region passing the matching.

However, the application of this requirement introduces a bias in the efficiency evaluation, because it discards events in which muons undergo final state radiation (FSR). Indeed, the muon momentum decreases when the radiation is emitted, and, consequently, the trajectory is modified, shifting the reconstructed muon track outside the cone of the original track. This effect causes an underestimation in the efficiency evaluation of about 2-3%, depending on the decay channel.

In order to avoid this bias, the ΔR truth-matching procedure is not applied in the analysis. On the other hand, in order to discard those reconstructed candidates that are not associated to the generated ones, but formed by the random association of a J/ψ plus one (or three) track, we exploit the *a priori* flat trend in the invariant-mass distribution of background events.

The number of reconstructed true signal events is in fact extracted through a fit to the invariant mass distribution of the reconstructed B_c (B^+) candidates, performed with a function formed by a Gaussian distribution and a flat polynomial function. This procedure allows to subtract the yield of background events from the total number of reconstructed events.

A different strategy is applied for the $B_c^+ \to J/\psi\pi^+\pi^+\pi^-$ mode, since the efficiency is evaluated by an unbinned maximum likelihood fit (see Sec.4.4.1) to generated events. In this case, the alternative to the truth-matching procedure is:

1. evaluate the total number of reconstructed signal events (N_s) through a fit to the reconstructed $J/\psi\pi^+\pi^+\pi^-$ invariant-mass distribution with a function composed by the sum of Gaussian distribution and flat polynomial function;

2. define the signal mass range as $\pm\,4\sigma$ from the mean of the Gaussian distribution, where σ is the signal resolution obtained from the fit;

3. extrapolate the number of background events within the signal mass range (N_b);

4. in the unbinned fit to generated events described in Sec.4.4.1, retain a reconstructed event if its invariant mass is in the signal region and the value of a variable r randomly generated between 0 and 1 is greater than the percentage of background events in the signal region ($r > N_b/N_s$).

C $B_c^+ \to J/\psi \pi^+ \pi^+ \pi^-$ efficiency function

In this Section the results of the fit to the simulated $B_c^+ \to J/\psi \pi^+ \pi^+ \pi^-$ events to obtain the efficiency function (Eq. 4.2) parameters are collected. In particular, they are shown in the form of projections of the expected number of reconstructed events on the seven invariant-mass combinations. Results of the fit to events selected by the HLT_Dimuon7_Jpsi_Displaced trigger path have already been shown in Sec. 4.4.1.

Here we report the results of the fit to events selected by the HLT_DoubleMu3p5_Jpsi_displaced (Fig. C.3) and HLT_DoubleMu4_Jpsi_displaced trigger paths (Fig. C.4), respectively.

Figure C.3: Number of simulated reconstructed events projected on the 7 two-body mass combinations used to describe the $B_c^+ \to J/\psi \pi^+ \pi^+ \pi^-$ decay. The black dots represent the number of reconstructed events; the blue line is the expected number of reconstructed events as resulting from the 7-dimensional fit; the hashed region represents the statistical uncertainty on the fit function. Events are selected with the HLT_DoubleMu3p5_Jpsi_Displaced trigger.
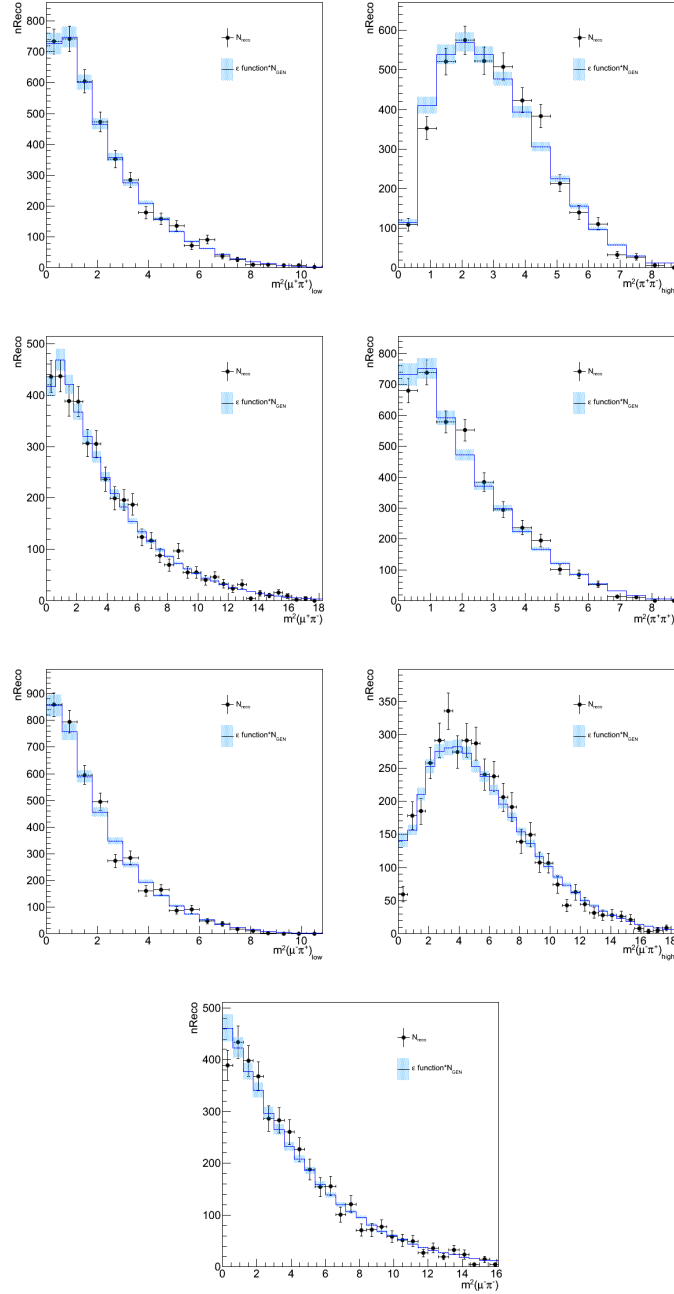
Figure C.4: Number of simulated reconstructed events projected on the 7 two-body mass combinations used to describe the $B_c^+ \to J/\psi \pi^+ \pi^+ \pi^-$ decay. The black dots represent the number of reconstructed events; the blue line is the expected number of reconstructed events as resulting from the 7-dimensional fit; the hashed region represents the statistical uncertainty on the fit function. Events are selected with the HLT_DoubleMu4_Jpsi_Displaced trigger.
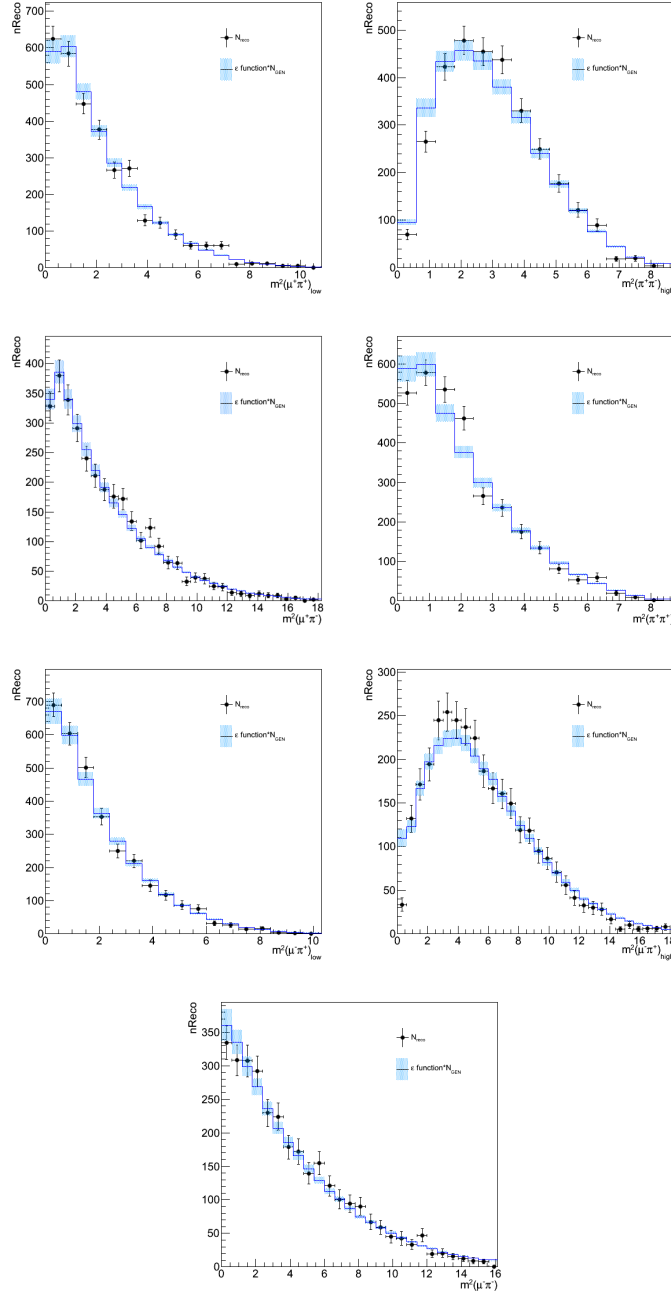
D Fit variant systematics

The method to evaluate the systematic uncertainty from different signal and background fit functions relies on the "fit variant" approach. Fitting conditions are varied, within reasonable limits, and only fits with sufficiently good fit quality and χ^2 are retained. Results from different fits are considered to be equally valid, and the statistical errors on the measurements correlated. Since each fit is *a priori* as likely, it is given equal weight and the estimate of the systematic error is simply the standard deviation of the set of variants. The systematic error is then evaluated as

$$\sigma_{sys} = \sqrt{\frac{\sum_{i=1}^{N} x_i^2 - N\bar{x}^2}{N-1}}, \tag{.1}$$

where x_i are the individual measurements and $\bar{x}$ is their mean.

D.1 Fit results

We summarize here the results for the different fits to the efficiency-corrected invariant mass distributions of $B_c^+ \to J/\psi \pi^+ \pi^+ \pi^-$, $B_c^+ \to J/\psi \pi^+$ and $B^+ \to J/\psi K^+$ respectively.

Fits to the $J/\psi \pi^+ \pi^+ \pi^-$ efficiency-corrected invariant mass

Plots of the different fits to the $J/\psi \pi^+ \pi^+ \pi^-$ efficiency-corrected invariant mass distribution are shown in Fig. D.5. The signal and background parametrization used in each fit are summarized in Table .1.

	Signal PDF	Bkg PDF	Range (GeV)
a	Gaussian	1st ord. Chebychev pol.	6.13 - 6.4
b	Gaussian	2nd ord. Chebychev pol.	6.10 - 6.4
c	Gaussian	2nd ord. Chebychev pol.	6.1 - 6.505
d	Gaussian	2nd ord. Chebychev pol.	5.8 - 6.7
e	Gaussian	3rd ord. Chebychev pol.	6 - 6.6
f	Gaussian	3rd ord. Chebychev pol.	5.8 - 6.7

Table .1: Alternative signal and background models used to fit the $J/\psi \pi^+ \pi^+ \pi^-$ efficiency-corrected invariant mass distribution. The corresponding plots are shown in Fig. D.5.
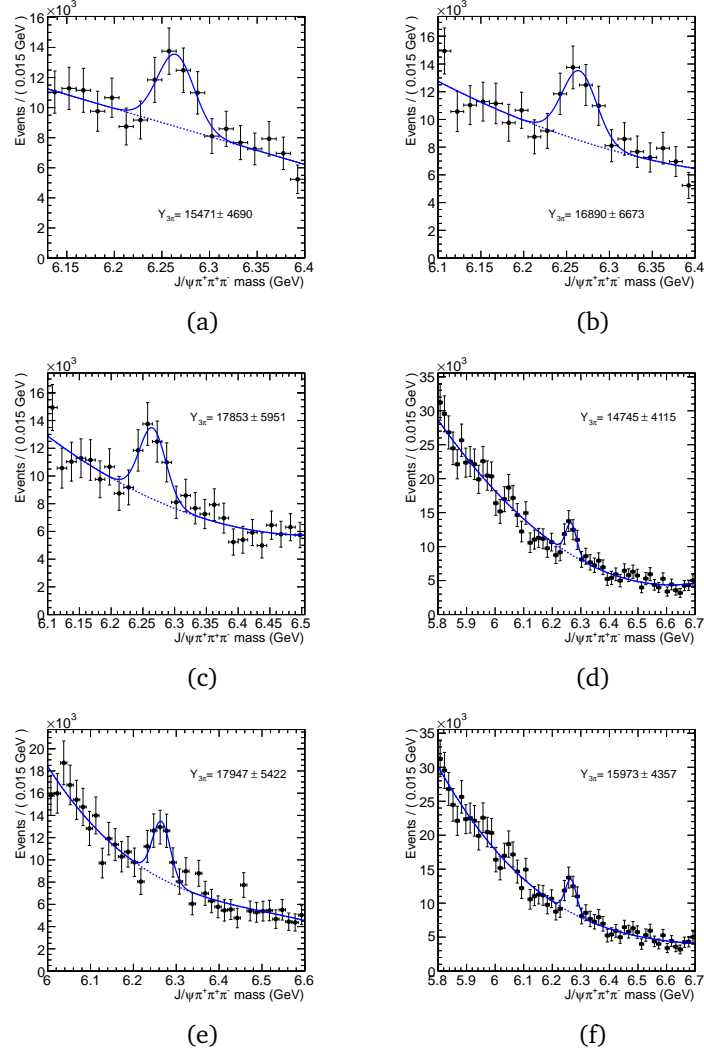
Figure D.5: Fits to the $J/\psi\pi^+\pi^+\pi^-$ efficiency-corrected invariant mass distribution with alternative signal and background parametrizations. The fit function corresponding to each fit is reported in Table .1.

Fits to the $J/\psi\pi^+$ efficiency-corrected invariant mass

Plots of the different fits to the $J/\psi\pi^+$ efficiency-corrected invariant mass distribution are shown in Fig. D.6. The definition of the signal and background model used in each fit is summarized in Table .2.

	Signal PDF	Bkg PDF	Range (GeV)
a	Gaussian	1st ord. Chebychev pol.	5.8 - 6.7
b	Gaussian	1st ord. Chebychev pol.	6.05 - 6.55
c	Gaussian	2nd ord. Chebychev pol.	6.05 - 6.55
d	Gaussian	2nd ord. Chebychev pol.	5.6 - 6.7
e	Gaussian	3rd ord. Chebychev pol.	5.8 - 6.7
f	Gaussian	Exponential	5.8 - 6.7
g	Double Gaussian	2nd ord. Chebychev pol.	5.8 - 6.7

Table .2: Alternative signal and background models used to fit the $J/\psi\pi^+$ efficiency-corrected invariant mass distribution. The corresponding plots are shown in Fig. D.6.

Fits to the $J/\psi K^+$ efficiency-corrected invariant mass

Plots of the different fits to the $J/\psi K^+$ efficiency-corrected invariant mass distribution are shown in Fig. D.7. The signal and background parametrization of each fit is reported Table .3. The $B^0 \to J/\psi X$ component is always parametrized with a Gaussian distribution.

	Signal PDF	Bkg PDF	$B^+ \to J/\psi\pi^+$ pdf	Range (GeV)
a	Crystal Ball	2nd ord. Ch. pol	Crystal Ball	5.15-5.5
b	Crystal Ball	2nd ord. Ch. pol	Landau	5.15-5.5
c	Crystal Ball	2nd ord. Ch. pol	Gaussian	5.15-5.5
d	Double Gauss.	2nd ord. Ch. pol	Crystal Ball	5.15-5.5
e	Double Gauss.	2nd ord. Ch. pol	Landau	5.15-5.5
f	Double Gauss.	3rd ord. Ch. pol	Gaussian	5.15-5.5
g	Double Gauss.	2nd ord. Ch. pol	Gaussian	5.05-5.6
h	Double Gauss.	2nd ord. Ch. pol	Gaussian	5.18-5.4

Table .3: Alternative signal and background models used to fit the $J/\psi K^+$ efficiency-corrected invariant mass distribution. The corresponding plots are shown in Fig. D.7.

(a)

(b)

(c)

(d)

(e)

(f)

(g)

Figure D.6: Fits to the $J/\psi\pi^+$ efficiency-corrected invariant mass distribution with alternative signal and background models. The fit function corresponding to each fit is reported in Table .2.
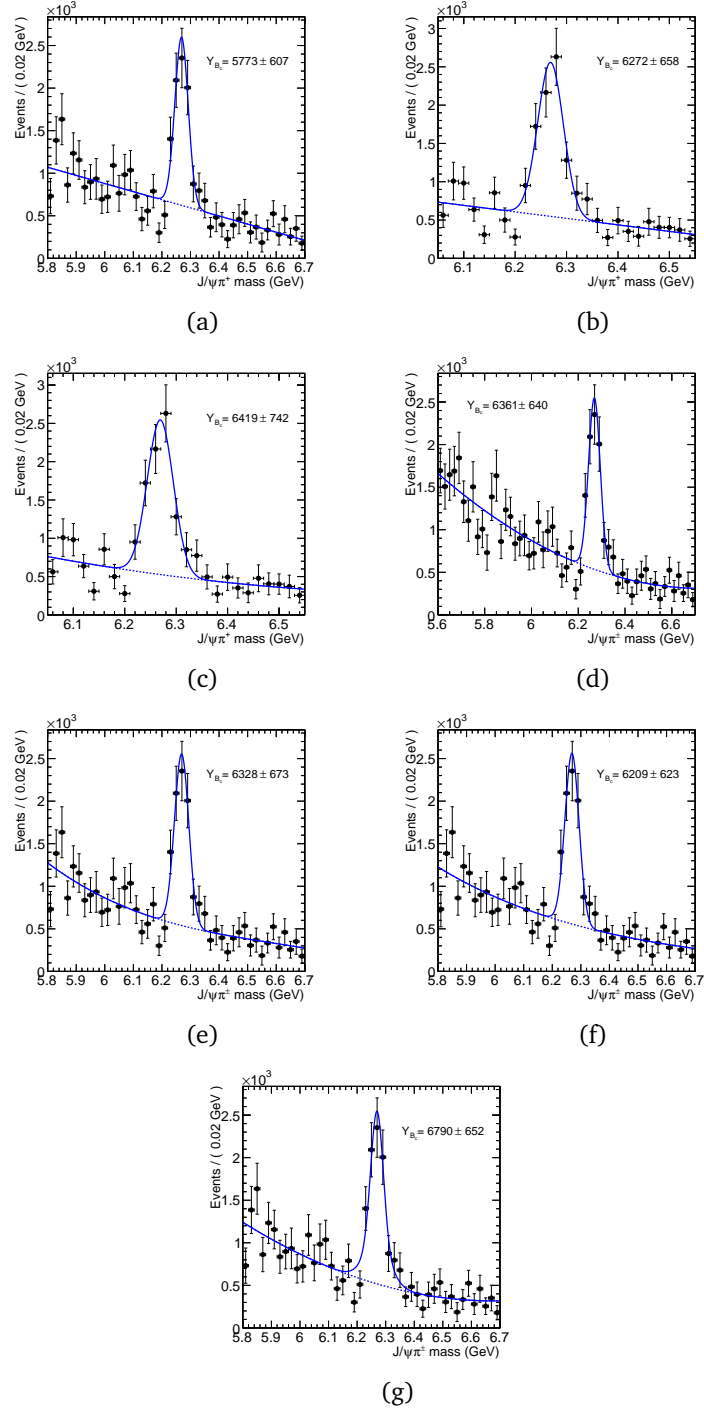
Figure D.7: Fits to the $J/\psi K^+$ efficiency-corrected invariant mass distribution with alternative signal and background models. The fit function corresponding to each fit is reported in Table .3.
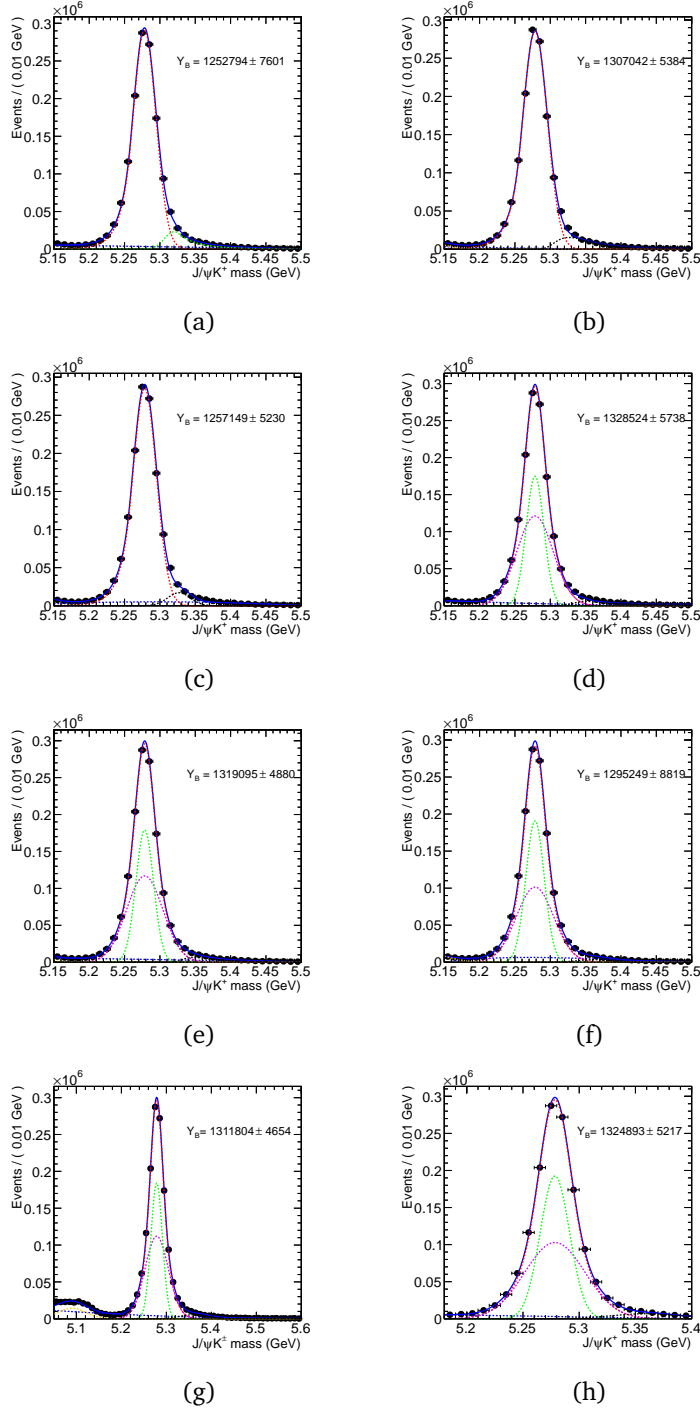
E   Split sample method

The split sample method is adopted asses a possible systematic uncertainty introduced by a residual difference between data and Monte Carlo, due to a possible mismatch in the reproduction of the main kinematic variables and experimental conditions of the spectrometer during data collection. This technique, modeled after the S-factor method [101], aims to separate true systematic variations from statistical fluctuations.

The data set is split in N independent samples and x_i individual measurements are performed with the associated errors σ_i ($i = 1, ...N$). If the N independent measurements are statistically consistent, there is no evidence for a split sample systematic uncertainty. To test the statistical consistency a χ^2 with N-1 degrees of freedom is calculated through the form

$$\chi^2 = \sum_{i=1}^{N} \frac{(x_i - \bar{x})^2}{\sigma_i^2} \tag{.2}$$

where $\bar{x}$ and $\bar{\sigma}$ are the weighted average and associated statistical error

$$\bar{x} = \frac{\sum_{i=1}^{N} x_i/\sigma_i^2}{\sum_{i=1}^{N} 1/\sigma_i^2} \qquad \text{and} \qquad \bar{\sigma} = \frac{1}{\sqrt{\sum_{i=1}^{N} 1/\sigma_i^2}}. \tag{.3}$$

If $\chi^2/(N-1) \leq 1$, then the measurements are statistically consistent with each other. However, if $\chi^2/(N-1) > 1$, it is likely that the split sample true errors are underestimated due to a systematic effect not taken into account. If each subsample statistical error σ_i is scaled by a factor S

$$S = \sqrt{\frac{\chi^2}{(N-1)}} \tag{.4}$$

it is guaranteed that $\chi^2/(N-1) = 1$ and also $\bar{\sigma}$ scales by the same factor to become a scaled variance $\tilde{\sigma}$.

The split sample variance σ_{split} is defined as the difference between the statistical variance of the entire dataset and the scaled variance, if the scaled variance exceeds the statistical variance, that is

$$\begin{aligned} \sigma_{split} &= \sqrt{\tilde{\sigma}^2 - \sigma_{stat}^2} && \text{if} \quad \tilde{\sigma} > \sigma_{stat}, \\ \sigma_{split} &= 0 && \text{if} \quad \tilde{\sigma} \leq \sigma_{stat}. \end{aligned} \tag{.5}$$

F B^+ **cross section**

In order to check the analysis procedure and the possible biases in the measurement of the reconstruction efficiency on the simulation, the B^+ cross section is calculated and compared to the CMS published results in Ref.[108], where the reconstruction efficiency is measured with a data-driven technique.

The differential cross section for B^+ production as a function of p_T is defined as

$$\frac{d\sigma(pp \to B^+ X)}{dp_T^B} = \frac{n_{sig}(p_T^B)}{\varepsilon(p_T^B)BL\Delta p_T^B},$$ (.6)

where $n_{sig}(p_T^B)$ is the signal yield in the given p_T bin, $\varepsilon(p_T^B)$ is the reconstruction efficiency in the given bin, Δp_T^B is the bin size in p_T. B is the total branching fraction, given by the product of the individual branching fractions $B(B^+ \to J/\psi K^+) = (1.014 \pm 0.034) \times 10^{-3}$ and $B(J/\psi \to \mu^+ \mu^-) = (5.93 \pm 0.06) \times 10^{-2}$ [101]. L is the integrated luminosity of the data sample.

The reference analysis provides the cross section measurement in five p_T bins starting from $p_T(B^+) > 5$ GeV, and considers the rapidity region $|y| < 2.4$.

We compare the results for two p_T bins common in the two analyses $[17, 24]$ and $[24, 30]$ GeV in Table .4. Note that the considered rapidity range is different in the two analysis. Cross section values from this work increase of $\sim$10% when enlarging the rapidity region to be the same as in $[108]$. Results are therefore compatible within the statistical error.

p_T^B (GeV)	This work	Ref.[108]
17-24	0.15 μb/GeV	0.181 $\pm$ 0.015 $\pm$ 0.012 μb/GeV
24-30	0.042 μb/GeV	0.042 $\pm$ 0.007 $\pm$ 0.004 μb/GeV

Table .4: Measured differential cross section $d\sigma/dp_T^B$ from this analysis and previous CMS result in Ref.[108]. Note that the considered rapidity range is different in the two analysis. Results from this work increase of $\sim$10% when enlarging the rapidity region to $|y| < 2.4$.

Bibliography

[1] S.L. Glashow. Partial Symmetries of Weak Interactions. *Nucl. Phys.*, 22, 1961. `doi:10.1016/0029-5582(61)90469-2`.

[2] A. Salam. Weak and Electromagnetic Interactions. *Conf. Proc.*, C680519, 1968.

[3] S. Weinberg. A Model of Leptons. *Phys. Rev. Lett.*, 19, 1967. `doi:10.1103/PhysRevLett.19.1264`.

[4] K. G. Wilson. Confinement of quarks. *Phys. Rev. D*, 10, 1974. `doi:10.1103/PhysRevD.10.2445`.

[5] P. W. Higgs. Broken symmetries, massless particles and gauge fields. *Phys. Lett.*, 12, 1964. `doi:10.1016/0031-9163(64)91136-9`.

[6] F. Englert and R. Brout. Broken Symmetry and the Mass of Gauge Vector Mesons. *Phys. Rev. Lett.*, 13, 1964. `doi:10.1103/PhysRevLett.13.321`.

[7] G. Aad et al. Observation of a new particle in the search for the Standard Model Higgs boson with the ATLAS detector at the LHC. *Phys. Lett.*, B716, 2012. `arXiv:1207.7214`, `doi:10.1016/j.physletb.2012.08.020`.

[8] S. Chatrchyan et al. Observation of a new boson at a mass of 125 GeV with the CMS experiment at the LHC. *Phys. Lett.*, B716, 2012. `arXiv:1207.7235`, `doi:10.1016/j.physletb.2012.08.021`.

[9] Precise determination of the mass of the Higgs boson and studies of the compatibility of its couplings with the standard model. Technical Report CMS-PAS-HIG-14-009, CERN, Geneva, 2014.

[10] Constraints on anomalous HVV interactions using H to 4l decays. Technical Report CMS-PAS-HIG-14-014, CERN, Geneva, 2014.

[11] N. Cabibbo. Unitary Symmetry and Leptonic Decays. *Phys. Rev. Lett.*, 10, 1963. `doi:10.1103/PhysRevLett.10.531`.

[12] M. Kobayashi and T. Maskawa. CP Violation in the Renormalizable Theory of Weak Interaction. *Prog. Theor. Phys.*, 49, 1973. `doi:10.1143/PTP.49.652`.

[13] L. Wolfenstein. Parametrization of the Kobayashi-Maskawa Matrix. *Phys. Rev. Lett.*, 51, 1983. `doi:10.1103/PhysRevLett.51.1945`.

[14] J. Charles et al. CP violation and the CKM matrix: Assessing the impact of the asymmetric *B* factories. *Eur. Phys. J.*, C41, 2005. `arXiv:hep-ph/0406184`, `doi:10.1140/epjc/s2005-02169-1`.

[15] [online]2014. URL: `http://ckmfitter.in2p3.fr/www/results/plots_moriond14/ckm_res_moriond14.html`.

[16] R. Aaij et al. Observation of the resonant character of the $Z(4430)^-$ state. *Phys. Rev. Lett.*, 112, 2014. `arXiv:1404.1903`, `doi:10.1103/PhysRevLett.112.222002`.

[17] S. Chatrchyan et al. Measurement of the X(3872) production cross section via decays to J/psi pi pi in pp collisions at sqrt(s) = 7 TeV. *JHEP*, 1304, 2013. `arXiv:1302.3968`, `doi:10.1007/JHEP04(2013)154`.

[18] Particle Data Group. Review of particle physics. *Chin. Phys. C*, 38.

[19] K. G. Wilson. Nonlagrangian models of current algebra. *Phys. Rev.*, 179, 1969. `doi:10.1103/PhysRev.179.1499`.

[20] M. Neubert. Heavy quark symmetry. *Phys. Rept.*, 245, 1994. `arXiv:hep-ph/9306320`, `doi:10.1016/0370-1573(94)90091-4`.

[21] W.E. Caswell and G.P. Lepage. Effective Lagrangians for Bound State Problems in QED, QCD, and Other Field Theories. *Phys. Lett.*, B167, 1986. `doi:10.1016/0370-2693(86)91297-9`.

[22] G. T. Bodwin, E. Braaten, and G. P. Lepage. Rigorous QCD analysis of inclusive annihilation and production of heavy quarkonium. *Phys. Rev.*, D51, 1995. `arXiv:hep-ph/9407339`, `doi:10.1103/PhysRevD.51.112510.1103/PhysRevD.55.5853`.

[23] S.S. Gershtein, V.V. Kiselev, A.K. Likhoded, and A.V. and Tkabladze. Physics of B(c) mesons. *Phys. Usp.*, 38, 1995. `arXiv:hep-ph/9504319`, `doi:10.1070/PU1995v038n01ABEH000063`.

[24] E. J. Eichten and C. Quigg. Mesons with beauty and charm: Spectroscopy. *Phys. Rev.*, D49, 1994. `arXiv:hep-ph/9402210, doi: 10.1103/PhysRevD.49.5845`.

[25] S. N. Gupta and J. M. Johnson. B(c) spectroscopy in a quantum chromodynamic potential model. *Phys. Rev.*, D53, 1996. `arXiv:hep-ph/9511267, doi:10.1103/PhysRevD.53.312`.

[26] E. Bagan, H. G. Dosch, P. Gosdzinsky, S. Narison, and J.M. Richard. Hadrons with charm and beauty. *Z. Phys.*, C64, 1994. `arXiv:hep-ph/9403208, doi:10.1007/BF01557235`.

[27] E. B. Gregory et al. Precise B, B_s, and B_c meson spectroscopy from full lattice QCD. *Phys. Rev. D*, 83, 2011. `doi:10.1103/PhysRevD.83.014506`.

[28] R. J. Dowdall, C. T. H. Davies, T. C. Hammant, and R. R. Horgan. Precise heavy-light meson masses and hyperfine splittings from lattice QCD including charm quarks in the sea. *Phys. Rev. D*, 86, 2012. `doi:10.1103/PhysRevD.86.094510`.

[29] I. F. Allison, C. T. H. Davies, A. Gray, A. S. Kronfeld, P. B. Mackenzie, and J. N. Simone. Mass of the B_c Meson in Three-Flavor Lattice QCD. *Phys. Rev. Lett.*, 94, 2005. `doi:10.1103/PhysRevLett.94.172001`.

[30] I.P. Gouz, V.V. Kiselev, A.K. Likhoded, V.I. Romanovsky, and O.P. Yushchenko. Prospects for the B_c studies at LHCb. *Phys. Atom. Nucl.*, 67, 2004. `arXiv:hep-ph/0211432, doi:10.1134/1.1788046`.

[31] C. Chang and X. Wu. Uncertainties in estimating hadronic production of the meson B_c and comparisons between TEVATRON and LHC. *Eur. Phys. J.*, C38, 2004. `arXiv:hep-ph/0309121, doi:10.1140/epjc/s2004-02015-0`.

[32] S. P. Baranov. Pair production of $B_c^{(*)}$ mesons in pp and $\gamma\gamma$ collisions. *Phys. Rev. D*, 55, 1997. `doi:10.1103/PhysRevD.55.2756`.

[33] K. Kolodziej, A. Leike, and R. Ruckl. Production of B(c) mesons in hadronic collisions. *Phys. Lett.*, B355, 1995. `arXiv:hep-ph/9505298, doi:10.1016/0370-2693(95)00710-3`.

[34] C. Chang, Y. Chen, G. Han, and H. Jiang. On hadronic production of the B(c) meson. *Phys. Lett.*, B364, 1995. `arXiv:hep-ph/9408242, doi:10.1016/0370-2693(95)01235-4`.

[35] C. Chang, Y. Chen, and R.J. Oakes. Comparative study of the hadronic production of B(c) mesons. *Phys. Rev.*, D54, 1996. `arXiv:hep-ph/9602411, doi:10.1103/PhysRevD.54.4344`.

[36] A.V. Berezhnoy, A.K. Likhoded, and M.V. Shevlyagin. Hadronic production of B(c) mesons. *Phys. Atom. Nucl.*, 58, 1995. `arXiv:hep-ph/9408284`.

[37] V.V. Kiselev, A.K. Likhoded, and A.V. Tkabladze. B(c) spectroscopy. *Phys. Rev.*, D51, 1995. `arXiv:hep-ph/9406339, doi:10.1103/PhysRevD.51.3613`.

[38] A. Abd El-Hady, J.H. Munoz, and J.P. Vary. Semileptonic and nonleptonic B(c) decays. *Phys. Rev.*, D62, 2000. `arXiv:hep-ph/9909406, doi:10.1103/PhysRevD.62.014019`.

[39] C.T.H. Davies, K. Hornbostel, G.P. Lepage, A.J. Lidsey, J. Shigemitsu, et al. B(c) spectroscopy from lattice QCD. *Phys. Lett.*, B382, 1996. `arXiv:hep-lat/9602020, doi:10.1016/0370-2693(96)00650-8`.

[40] V.V. Kiselev. Exclusive decays and lifetime of B_c meson in QCD sum rules. 2002. `arXiv:hep-ph/0211021`.

[41] M. Beneke and G. Buchalla. The B_c Meson Lifetime. *Phys. Rev.*, D53, 1996. `arXiv:hep-ph/9601249, doi:10.1103/PhysRevD.53.4991`.

[42] A. I. Onishchenko. Doubly heavy systems: Decays and OPE. 1999. `arXiv:hep-ph/9912424`.

[43] M. A. Shifman. Quark hadron duality. 2000. `arXiv:hep-ph/0009131`.

[44] C. Chang, S. Chen, T. Feng, and X. Li. The Lifetime of B_c meson and some relevant problems. *Phys. Rev.*, D64, 2001. `arXiv:hep-ph/0007162, doi:10.1103/PhysRevD.64.014003`.

[45] V.V. Kiselev, A.K. Likhoded, and A.I. Onishchenko. Semileptonic B_c meson decays in sum rules of QCD and NRQCD. *Nucl. Phys.*, B569, 2000. `arXiv:hep-ph/9905359, doi:10.1016/S0550-3213(99)00505-2`.

[46] V.V. Kiselev, A.E. Kovalsky, and A.K. Likhoded. Decays and lifetime of B_c in QCD sum rules. 2000. `arXiv:hep-ph/0006104`.

[47] N. Brambilla et al. Heavy quarkonium physics. 2004. `arXiv:hep-ph/0412158`.

[48] P. Colangelo and F. De Fazio. Radiative leptonic B_c decays. *Mod. Phys. Lett.*, A14, 1999. `arXiv:hep-ph/9904363, doi:10.1142/ S0217732399002388`.

[49] C.i Chang, J. Cheng, and C. Lu. Radiative leptonic decays of B(c) meson. *Phys. Lett.*, B425, 1998. `arXiv:hep-ph/9712325, doi:10.1016/ S0370-2693(98)00177-4`.

[50] H. Choi and C. Ji. Non-leptonic two-body decays of the B(c) meson in light-front quark model and QCD factorization approach. *Phys. Rev.*, D80, 2009. `arXiv:0909.5028, doi:10.1103/PhysRevD.80.114003`.

[51] A.K. Likhoded and A.V. Luchinsky. Light hadron production in $B_c \rightarrow J/\psi + X$ decays. *Phys. Rev.*, D81, 2010. `arXiv:0910.3089, doi:10. 1103/PhysRevD.81.014015`.

[52] Z. Wang. The B_c-decays $B_c^+ \rightarrow J/\psi \pi^+ \pi^- \pi^+$, $\eta_c \pi^+ \pi^- \pi^+$. *Phys. Rev.*, D86, 2012. `arXiv:1205.5317, doi:10.1103/PhysRevD.86. 054010`.

[53] C. Chang, C. Driouichi, P. Eerola, and X. Wu. BCVEGPY: An Event generator for hadronic production of the B_c meson. *Comput.Phys.Commun.*, 159, 2004. `arXiv:hep-ph/0309120, doi:10.1016/j.cpc.2004. 02.005`.

[54] C. Chang, J. Wang, and X. Wu. BCVEGPY2.0: A Upgrade version of the generator BCVEGPY with an addendum about hadroproduction of the P-wave B_c states. *Comput.Phys.Commun.*, 174, 2006. `arXiv:hep-ph/ 0504017, doi:10.1016/j.cpc.2005.09.008`.

[55] T. Sjostrand, S. Mrenna, and P. Z. Skands. PYTHIA 6.4 Physics and Manual. *JHEP*, 0605, 2006. `arXiv:hep-ph/0603175, doi:10.1088/ 1126-6708/2006/05/026`.

[56] R. Field. Early LHC Underlying Event Data - Findings and Surprises. 2010. `arXiv:1010.3558`.

[57] D.J. Lange. The EvtGen particle decay simulation package. *Nucl.Instrum.Meth.*, A462, 2001. `doi:10.1016/S0168-9002(01) 00089-4`.

[58] S. Agostinelli et al. GEANT4: A Simulation toolkit. *Nucl.Instrum.Meth.*, A506, 2003. `doi:10.1016/S0168-9002(03)01368-8`.

[59] F. Abe et al. Observation of the B_c meson in $p\bar{p}$ collisions at $\sqrt{s} = 1.8$ TeV. *Phys. Rev. Lett.*, 81, 1998. `arXiv:hep-ex/9805034, doi:10.1103/PhysRevLett.81.2432`.

[60] F. Abe et al. Observation of B_c mesons in $p\bar{p}$ collisions at $\sqrt{s} = 1.8$ TeV. *Phys. Rev.*, D58, 1998. `arXiv:hep-ex/9804014, doi:10.1103/PhysRevD.58.112004`.

[61] T. Aaltonen et al. Observation of the Decay $B_c^\pm \to J/\psi\pi^\pm$ and Measurement of the $B_c^\pm$ Mass. *Phys. Rev. Lett.*, 100, 2008. `arXiv:0712.1506, doi:10.1103/PhysRevLett.100.182002`.

[62] V. M. Abazov et al. Observation of the B_c Meson in the Exclusive Decay $B_c \to J/\psi\pi$. *Phys. Rev. Lett.*, 101, 2008. `arXiv:0802.4258, doi:10.1103/PhysRevLett.101.012001`.

[63] A. Abulencia et al. Measurement of the B_c^+ meson lifetime using $B_c^+ \to J/\psi e^+ \nu_e$. *Phys. Rev. Lett.*, 97, 2006. `arXiv:hep-ex/0603027, doi:10.1103/PhysRevLett.97.012002`.

[64] V. M. Abazov et al. Measurement of the lifetime of the $B_c^\pm$ meson in the semileptonic decay channel. *Phys. Rev. Lett.*, 102, 2009. `arXiv:0805.2614, doi:10.1103/PhysRevLett.102.092001`.

[65] T. Aaltonen et al. Measurement of the B_c^- meson lifetime in the decay $B_c^- \to J/\psi\ \pi^-$. *Phys. Rev.*, D87, 2013. `arXiv:1210.2366, doi:10.1103/PhysRevD.87.011101`.

[66] R. Aaij et al. First observation of the decay $B_c^+ \to J/\psi\pi^+\pi^-\pi^+$. *Phys. Rev. Lett.*, 108, 2012. `arXiv:1204.0079, doi:10.1103/PhysRevLett.108.251802`.

[67] R. Aaij et al. First observation of the decay $B_c^+ \to J/\psi K^+$. *JHEP*, 1309, 2013. `arXiv:1306.6723, doi:10.1007/JHEP09(2013)075`.

[68] R. Aaij et al. Evidence for the decay $B_c^+ \to J/\psi 3\pi^+2\pi^-$. *JHEP*, 1405, 2014. `arXiv:1404.0287, doi:10.1007/JHEP05(2014)148`.

[69] R. Aaij et al. Observation of the decay $B_c \to J/\psi K^+K^-\pi^+$. *JHEP*, 1311, 2013. `arXiv:1309.0587, doi:10.1007/JHEP11(2013)094`.

[70] R. Aaij et al. Observation of $B_c^+ \to J/\psi D_s^+$ and $B_c^+ \to J/\psi D_s^{*+}$ decays. *Phys. Rev.*, D87(11), 2013. `arXiv:1304.4530, doi:10.1103/PhysRevD.87.112012`.

[71] R. Aaij et al. Observation of the decay $B_c^+ \to \psi(2S)\pi^+$. *Phys. Rev.*, D87, 2013. `arXiv:1303.1737, doi:10.1103/PhysRevD.87.071103`.

[72] R. Aaij et al. First observation of a baryonic B_c^+ decay. *Phys. Rev. Lett.*, 113, 2014. `arXiv:1408.0971, doi:10.1103/PhysRevLett.113.152003`.

[73] R. Aaij et al. Measurement of the ratio of B_c^+ branching fractions to $J/\psi\pi^+$ and $J/\psi\mu^+\nu_\mu$. *Phys. Rev.*, D90, 2014. `arXiv:1407.2126, doi:10.1103/PhysRevD.90.032009`.

[74] R. Aaij et al. Observation of the Decay $B_c^+ \to B_s^0\pi^+$. *Phys. Rev. Lett.*, 111(18), 2013. `arXiv:1308.4544, doi:10.1103/PhysRevLett.111.181801`.

[75] R. Aaij et al. Measurement of the B_c^+ meson lifetime using $B_c^+ \to J/\psi\mu^+\nu_\mu X$ decays. *Eur. Phys. J.*, C74, 2014. `arXiv:1401.6932, doi:10.1140/epjc/s10052-014-2839-x`.

[76] R Aaij et al. Measurements of B_c^+ production and mass with the $B_c^+ \to J/\psi\pi^+$ decay. *Phys. Rev. Lett.*, 109, 2012. `arXiv:1209.5634, doi:10.1103/PhysRevLett.109.232001`.

[77] G. Aad et al. Observation of an Excited $B_c^\pm$ Meson State with the ATLAS Detector. 2014. `arXiv:1407.1032`.

[78] L. Evans and P. Bryant. LHC Machine. *JINST*, 3, 2008. `doi:10.1088/1748-0221/3/08/S08001`.

[79] S. Myers and E. Picasso. The Design, construction and commissioning of the CERN Large Electron Positron collider. *Contemp. Phys.*, 31, 1990. `doi:10.1080/00107519008213789`.

[80] G. Aad et al. The ATLAS Experiment at the CERN Large Hadron Collider. *JINST*, 3, 2008. `doi:10.1088/1748-0221/3/08/S08003`.

[81] S. Chatrchyan et al. The CMS experiment at the CERN LHC. *JINST*, 3, 2008. `doi:10.1088/1748-0221/3/08/S08004`.

[82] Jr. Alves, A. Augusto et al. The LHCb Detector at the LHC. *JINST*, 3, 2008. `doi:10.1088/1748-0221/3/08/S08005`.

[83] K. Aamodt et al. The ALICE experiment at the CERN LHC. *JINST*, 3, 2008. `doi:10.1088/1748-0221/3/08/S08002`.

[84] G. Anelli et al. The TOTEM experiment at the CERN Large Hadron Collider. *JINST*, 3, 2008. `doi:10.1088/1748-0221/3/08/S08007`.

[85] O. S. Bruning, P. Collier, P. Lebrun, S. Myers, R. Ostojic, J. Poole, and P. Proudlock. *LHC Design Report*. CERN, Geneva, 2004.

[86] S. Chatrchyan et al. The performance of the CMS muon detector in proton-proton collisions at sqrt(s) = 7 TeV at the LHC. *JINST*, 8, 2013. `arXiv:1306.6905`, `doi:10.1088/1748-0221/8/11/P11002`.

[87] *The CMS tracker system project: Technical Design Report*. Technical Design Report CMS. CERN, Geneva, 1997.

[88] *The CMS electromagnetic calorimeter project: Technical Design Report*. Technical Design Report CMS. CERN, Geneva, 1997.

[89] *The CMS hadron calorimeter project: Technical Design Report*. Technical Design Report CMS. CERN, Geneva, 1997.

[90] *The CMS muon project: Technical Design Report*. Technical Design Report CMS. CERN, Geneva, 1997.

[91] P. Billoir. Progressive track recognition with a Kalman-like fitting procedure. *Comput.Phys.Commun.*, 57(1-3), 1989. `doi:10.1016/0010-4655(89)90249-X`.

[92] P. Billoir and S. Qian. Simultaneous pattern recognition and track fitting by the Kalman filtering method. *Nucl. Instrum. Meth. A*, 294(1-2), 1990. `doi:10.1016/0168-9002(90)91835-Y`.

[93] S. Chatrchyan et al. Description and performance of track and primary-vertex reconstruction with the CMS tracker. *JINST*, 9(10), 2014. `arXiv:1405.6569`, `doi:10.1088/1748-0221/9/10/P10009`.

[94] K. Rose. Deterministic Annealing for Clustering, Compression, Classification, Regression and related Optimisation Problems. *Proc. IEEE 86*, 86, 1998.

[95] W. Waltenberger, R. Fruhwirth, and P. Vanlaer. Adaptive vertex fitting. *J. Phys. G*, 34(12), 2007. URL: `http://stacks.iop.org/0954-3899/34/i=12/a=N01`.

[96] T. Miao, N. Leioatts, H. Wenzel, and F. Yumiceva. Beam Position Determination using Tracks. Technical Report CMS-NOTE-2007-021, CERN, Geneva, 2007.

[97] K. Prokofiev and T. Speer. A kinematic and a decay chain reconstruction library. 2005.

[98] S. Chatrchyan et al. Performance of CMS muon reconstruction in cosmic-ray events. *JINST*, 5, 2010. `arXiv:0911.4994`, `doi:10.1088/1748-0221/5/03/T03022`.

[99] S. Chatrchyan et al. Performance of CMS muon reconstruction in pp collision events at $\sqrt{s} = 7$ TeV. *JINST*, 7, 2012. `arXiv:1206.4071`, `doi:10.1088/1748-0221/7/10/P10002`.

[100] *CMS TriDAS project: Technical Design Report, Volume 1: The Trigger Systems*. Technical Design Report CMS.

[101] Particle Data Group. Review of particle physics. *Phys. Rev. D*, 86, (2012) 010001 and the 2013 partial update for the 2014 edition (URL: http://pdg.lbl.gov. `doi:10.1103/PhysRevD.86.010001`.

[102] Search for hadronic $b \rightarrow u$ decays. *Phys. Lett. B*, 241(2), 1990. `doi:http://dx.doi.org/10.1016/0370-2693(90)91293-K`.

[103] T. Skwarnicki. A study of the radiative CASCADE transitions between the Upsilon-Prime and Upsilon resonances. 1986.

[104] I. M. Chakravarti, R. G. Laha, and J. Roy. *Handbook of Methods of Applied Statistics*, volume I. Wiley, 1967.

[105] CMS Collaboration. Measurement of tracking efficiency. CMS Physics Analysis Summary CMS-PAS-TRK-10-002, 2010. URL: `http://cdsweb.cern.ch/record/1279139`.

[106] A.V. Berezhnoy, A.K. Likhoded, and A.V. Luchinsky. BC_NPI module for the analysis of $B_c \rightarrow J/\psi + n\pi$ and $B_c \rightarrow B_s + n\pi$ decays within the EvtGen package. 2011. `arXiv:1104.0808`.

[107] C. Peterson, D. Schlatter, I. Schmitt, and P. M. Zerwas. Scaling Violations in Inclusive e+ e- Annihilation Spectra. *Phys. Rev.*, D27, 1983. `doi:10.1103/PhysRevD.27.105`.

[108] V. Khachatryan et al. Measurement of the B^+ Production Cross Section in pp Collisions at $\sqrt{s} = 7$ TeV. *Phys. Rev. Lett.*, 106, 2011. `arXiv:1101.0131`, `doi:10.1103/PhysRevLett.106.112001`.